STRUCTURE-PROPERTY RELATIONSHIP OF Ba2+ and Ti4+ DOPED MULTIFERROIC BISMUTH FERRITE

BY

Rubayyat Mahbub Turjo
STUDENT NUMBER 0412112007

THIS THESIS PAPER IS SUBMITTED TO THE DEPARTMENT OF MATERIALS AND METALLURGICAL ENGINEERING IN PARTIAL FULFILLMENT OF THE REQUIREMENTS FOR THE DEGREE OF MASTER OF SCIENCE IN MATERIALS AND METALLURGICAL ENGINEERING

DEPARTMENT OF MATERIALS AND METALLURGICAL ENGINEERING
BANGLADESH UNIVERSITY OF ENGINEERING AND TECHNOLOGY

CANDIDATES' DECLARATION

IT IS HEREBY DECLARED THAT THIS THESIS PAPER OR ANY PART OF IT HAS NOT BEEN SUBMITTED ANYWHERE ELSE FOR THE AWARD OF ANY DEGREE

.....

Rubayyat Mahbub Turjo
M.Sc. Engg., MME, BUET

The thesis titled "Structure-property Relationship of Ba^{2+} and Ti^{4+} Doped Multiferroic Bismuth Ferrite" submitted by Rubayyat Mahbub Turjo, student no 0412112007 P, session April 2012 has been accepted as satisfactory in partial fulfillment of the requirements for the degree of Master of Science in Materials and Metallurgical Engineering on September, 2014.

Board of Examiners

.....

Chairman
Dr. Md. Fakhrul Islam
Professor & Head, GCE, BUET, Dhaka.

.....

Member (Ex-Officio)
Dr. Ahmed Sharif
Professor & Head, MME, BUET, Dhaka.

.....

Member
Dr. A K M Abdul Hakim
Individual Consultant, GCE, BUET, Dhaka.

.....

Member
Dr. A. K. M. Bazlur Rashid
Professor, MME, BUET, Dhaka.

.....

Member (External)
Dr. Sheikh Manjura Hoque
Principal Scientific Officer, Material Science Division, Atomic Energy Centre, BAEC, Kazi Nazrul Islam Avenue, Ramna, P.O. Box-162,Dhaka-1000.

DEDICATION

TO MY BELOVED PARENTS

ACKNOWLEDGEMENTS

I would like to start by thanking the Almighty for blessing me with everything that I could have asked for.

Foremost, I would like to express my sincere gratitude to my supervisor, Prof. Dr. Md. Fakhrul Islam. Without his enthusiasm, his inspiration and his great efforts this work would have remained a dream. I thank him from the bottom of my heart for his sincere cooperation, precious advice and consistent encouragement. His dedication and the drive for excellence in any task undertaken has been one of the primary motivating factors in this thesis. I am indebted to him for providing me all necessary facilities and opinions whenever required.

I would also like to pay my exhaustive gratefulness to all the faculties and staffs of the Department of Materials and Metallurgical Engineering, BUET for their support and motivation throughout this research project, specially Head of the Department Prof. Dr. Ahmed Sharif for his constant encouragement. I specially thank the Department of Glass and Ceramic Engineering (GCE), BUET and all of its members. Without their constant assistance this work would not have been possible. Without the lab facilities and raw materials provided by GCE my research project would have remained undone.

It is difficult to overstate my gratitude to Dr. A K M Abdul Hakim and Dr. M.A. Matin for guiding me with their valuable advices and expertise that has helped me immensely. I truly appreciate and value the esteemed guidance of Dr. AKM Abdul Hakim from the beginning to the end of this thesis.

I am eternally grateful to Mehedi Hasan Rizvi, Lecturer, GCE; Arman Hussain, Lecturer, GCE and Takian Fakhrul, Lecturer, MME. All the ideas we shared and discussed have proven very useful. This project would not have gone so well without their contribution at the forefront of this research.

I convey my heartiest regards to Dr. Sheikh Monjura Hoque, Principle Scientific Officer, Materials Science Division, AEC, Dhaka. I am extremely grateful to her for sharing her wisdom and for generously letting me use his VSM lab on such short notice.

I also express my sincere gratitude to Dr. Gafur, Senior Scientific Officer, BCSIR and Mr. Rakib, Engineer, BCSIR for their support with the XRD and DTA analysis. I specially thank Dr. Gagur for his invaluable advice and support which helped me greatly while working on this research project.

Above all, I would like to thank all my family members and friends whose direct and indirect support helped me completing my project in time. This thesis would have been impossible without their perpetual moral support.

Last but not the least, I would like to thank my parents for their undying support, encouragement, and endless love throughout my life.

ABSTRACT

The main focus of this research was to correlate the microstructure with multiferroic properties of $Bi_{1-x}Ba_xFe_{1-y}Ti_yO_3$ *(x = 0.1, y = 0.0; x = 0.2, y = 0.0; x = 0.3, y = 0.0; and x = 0.3, y = 0.1) samples. The role of doping Ba at Bi-site and Ti at Fe-site on the microstructure and multiferroic properties of* $BiFeO_3$ *ceramic has been investigated in this research. Single phase* $Bi_{1-x}Ba_xFe_{1-y}Ti_yO_3$ *were synthesized by the conventional solid-state reaction method. The* $Bi_{1-x}Ba_xFe_{1-y}Ti_yO_3$ *dried pellets were calcined at 800°C for 2 hours followed by sintering in the temperature range of 850-900°C. Phase analysis by X–ray diffraction (XRD) confirmed the formation of single phase distorted R3c structure. Increase in unit cell volume with increasing doping concentration has also been reported by XRD analysis. Percentage theoretical density above 95% was achieved for all compositions in this research. Microstructural investigation using the field emission scanning electron microscope (FESEM) showed that, increased doping concentration dramatically reduced the average grain size of* $Bi_{1-x}Ba_xFe_{1-y}Ti_yO_3$ *due to the strong pinning effect of dopants. Ba and Ti doped BFO showed superior values of dielectric constant and ferromagnetic properties. The best values of room temperature dielectric constant (~2885) at 1 kHz frequency was attained by* $Bi_{0.7}Ba_{0.3}Fe_{0.9}Ti_{0.1}O_3$ samples *having average grain size in the range of 1.0-1.05 µm. The lack of oxygen vacancies in this sample provided high resistivity and thereby resulted in high dielectric constant. At higher temperatures a considerable increase in the dielectric constant of* $Bi_{0.9}Ba_{0.1}FeO_3$ *and* $Bi_{0.7}Ba_{0.3}FeO_3$ *samples occurred due to space charge polarization. However, in* $Bi_{0.8}Ba_{0.2}FeO_3$ *and* $Bi_{0.7}Ba_{0.3}Fe_{0.9}Ti_{0.1}O_3$ *the stability of dielectric constant with temperature was considerably improved due to lack of oxygen vacancy in these samples. Moreover, DTA analysis revealed the shift of peak for ferroelectric transition* (T_C) *towards higher temperatures with increased doping concentration, which reached 866°C for* $Bi_{0.7}Ba_{0.3}Fe_{0.9}Ti_{0.1}O_3$*. As expected from the XRD results the remnant magnetization also increased with doping concentration and reached 0.9 emu/gram for* $Bi_{0.7}Ba_{0.3}Fe_{0.9}Ti_{0.1}O_3$*. This increase in remnant magnetization can be attributed to the increased distortion with increasing doping concentration. Maximum coercivity (~2.5kOe) was attained by single Ba doped* $Bi_{1-x}Ba_xFe_{1-y}Ti_yO_3$ *(x = 0.1, y = 0.0; x = 0.2, y = 0.0; x = 0.3, y = 0.0) samples. However the decrease in coercivity to 1.8kOe in* $Bi_{0.7}Ba_{0.3}Fe_{0.9}Ti_{0.1}O_3$ *sample can be attributed to the easiness of spin flipping in this sample due to substitution of Fe-site with Ti having different valance.*

Table of Contents

ACKNOWLEDGEMENTS v

ABSTRACT vi

List of Figures x

List of Tables xiv

CHAPTER 1 INTRODUCTION 1

1.1 Background of the research 2

1.2 Motivation of the research 3

1.3 Aims of the research 8

1.4 Current research trends 8

1.5 Recent works on A-site and B-site doping of BFO 9

1.6 Targets and challenges of this thesis 13

CHAPTER 2 LITERATURE REVIEW 16

2.1 Introduction 17

2.2 Primary ferroics 17

2.2.1 Ferroelectric materials 19

2.2.2 Ferro-, antiferro-, and ferri-magnetic materials 22

2.2.3 Ferroelastic material 25

2.3 Order parameter couplings 27

2.4 Multiferroics and magnetoelectric effect 28

2.4.1 Classification of multiferroics 29

2.4.1.1 Single phase multiferroics 29

- Type-I multiferroics 30
- Type-II multiferroics: Magnetic multiferroics 33

2.4.1.2 Multiphase multiferroics 34

2.4.2 Why is it difficult to find materials that are both ferroelectric and magnetic in a single phase? 35

2.5 $BiFeO_3$ multiferroics 36

2.5.1 History of $BiFeO_3$ 36

2.5.2 Science of $BiFeO_3$ 37

2.5.2.1 Structure of $BiFeO_3$ 38

2.5.2.2 Phase diagram of $BiFeO_3$ 39
2.5.3 Electrical properties of $BiFeO_3$ 40
2.5.3.1 Dielectric constant of $BiFeO_3$ 42
2.5.4 Magnetic properties of $BiFeO_3$ 43
2.4.5 Processing of bismuth ferrite based ceramics 44
2.4.5.1 Ball Milling 45
2.4.5.2 Shaping and drying 46
2.4.5.3 Sintering 47
CHAPTER 3 EXPERIMENTAL 49
3.1 Introduction 50
3.2 Raw materials and their characterization 50
3.3 Sample Preparation 51
3.3.1 Weight measurement 52
3.3.2 Milling 52
3.3.4 Compaction 53
3.3.5 Sintering 54
3.3.6 Post sintering operations 55
3.4 Property measurement 56
3.4.1 Percent theoretical density measurement 56
3.4.2 Microstructure study 56
3.4.3 Phase study 57
3.4.4 Dielectric property measurement 58
3.4.5 Thermal Analysis 60
3.4.6 Magnetic property measurement 61
CHAPTER 4 RESULTS AND DISCUSSION 62
4.1 Introduction 63
4.2 Dependence of percent theoretical density and <grain size> on sintering temperature and doping concentration 69
4.3 Microstructure development 74
4.4 XRD analysis 89
4.5 Dielectric property measurement 90

4.6 Differential thermal analysis (DTA) for determining transition point 96
4.7 Magnetic property measurement 98
CHAPTER 5 CONCLUSION 102
CHAPTER 6 SUGGESTION FOR FUTURE WORK 104

List of Figures

Figure 1.1	Schematic view of the R3c structure built up from two cubic perovskite $BiFeO_3$ unit cells.	3
Figure 1.2	The four degrees of multiferroic order. a–d, Electric polarization P and magnetization M can assume four non-collinear states in a multiferroic crystal.	4
Figure 1.3	Schematic of a tunnel junction. Electrons tunnel from the bottom electrode through the barrier into the top electrode.	5
Figure 1.4	Sketch of a possible MERAM element.	6
Figure 1.5	Magnetic hysteresis loops of $Bi_{1-x}Ba_xFeO_3$ (x=0.15, 0.25).	10
Figure 1.6	M-H loops of $Bi_{1-x}Ba_xFeO_3$ (x=0.1, 0.2 and 0.3) samples.	12
Figure 1.7	P-E loops of $Bi_{1-x}Ba_xFeO_3$ (x=0.1, 0.15, 0.2 and 0.25) samples.	12
Figure 2.1	Hysteresis loops of (a) ferromagnetic, (b) ferroelectric and (c) ferroelastic materials.	18
Figure 2.2	Schematic representation of ferroelectric and ferromagnetic characteristics.	19
Figure 2.3	Perovskite crystal structure, showing a dipole moment generated by a displaced B-site atom.	21
Figure 2.4	Common examples of magnetic dipole ordering.	23
Figure 2.5	M-H curves for (a) diamagnetic, paramagnetic, antiferromagnetic (b) ferromagnetic and ferromagnetic materials	24
Figure 2.6	M-H curves for ferromagnetic and ferrimagnetic materials.	25
Figure 2.7	Experimentally observed microstructures of lead phosphate.	26
Figure 2.8	Ferroic orders and possible couplings between them.	27
Figure 2.9	Magnetoelectric Multiferroics.	28

Figure 2.10	Different microscopic mechanisms found in type-I multiferroics.	31
Figure 2.11	Schematic illustration of a structural transition process.	38
Figure 2.12	Phase Diagram of Fe_2O_3 and Bi_2O_3.	39
Figure 2.13	Schematic of crystal structure of BFO and ferroelectric polarization (arrow).	41
Figure 2.14	(Colour on-line) Schematic of tetragonal-like $BiFeO_3$ (BFO) with G-type antiferromagnetic ordering.	43
Figure 2.15	Schematics of the 64 nm antiferromagnetic circular cycloid.	44
Figure 2.16	Schematic representation of ball milling.	46
Figure 3.1	Disk shape sample.	51
Figure 3.2	Schematic representation of compaction process.	53
Figure 3.3	Furnaces used for sintering ceramics sample.	54
Figure 3.4	Sintering Cycles.	54
Figure 3.5	Field Emission Scanning Electron Microscope (FESEM).	57
Figure 3.6	XRD Machine.	57
Figure 3.7	Impedance Analyzer.	59
Figure 3.8	Differential Thermal Analyzer.	60
Figure 3.9	Vibrating Sample Magnetometer.	61
Figure 4.1	Sintering cycle-1.	64
Figure 4.2	Sintering cycle-1.	67
Figure 4.3	Variation of percent theoretical density with sintering temperature of $Bi_{1-x}Ba_xFe_{1-y}Ti_yO_3$ (x = 0.1, y = 0.0; x = 0.2, y = 0.0; x = 0.3, y = 0.0; and x = 0.3, y = 0.1) ceramics for **1 hour holding time at the sintering temperature**.	70
Figure 4.4	Variation of percent theoretical density with sintering temperature of $Bi_{1-x}Ba_xFe_{1-y}Ti_yO_3$ (x = 0.1, y = 0.0; x = 0.2, y = 0.0; x = 0.3, y = 0.0; and x = 0.3, y = 0.1) ceramics for **2 hours holding time at the sintering temperature**.	70
Figure 4.5	Variation of percent theoretical density with doping concentration of $Bi_{1-x}Ba_xFe_{1-y}Ti_yO_3$ (x = 0.1, y = 0.0; x = 0.2, y = 0.0; x = 0.3, y = 0.0; and x = 0.3, y = 0.1) ceramics for **1 hour holding time at the sintering temperature**.	71

Figure 4.6 Variation of percent theoretical density with doping concentration of $Bi_{1-x}Ba_xFe_{1-y}Ti_yO_3$ (x = 0.1, y = 0.0; x = 0.2, y = 0.0; x = 0.3, y = 0.0; and x = 0.3, y = 0.1) ceramics for **2 hours holding time at the sintering temperature**. 71

Figure 4.7 Variation of <grain size> with sintering temperature of $Bi_{1-x}Ba_xFe_{1-y}Ti_yO_3$ (x = 0.1, y = 0.0; x = 0.2, y = 0.0; x = 0.3, y = 0.0; and x = 0.3, y = 0.1) ceramics for **1 hour holding time at the sintering temperature**. 72

Figure 4.8 Variation of < grain size> with sintering temperature of $Bi_{1-x}Ba_xFe_{1-y}Ti_yO_3$ (x = 0.1, y = 0.0; x = 0.2, y = 0.0; x = 0.3, y = 0.0; and x = 0.3, y = 0.1) ceramics for **2 hours holding time at the sintering temperature**. 78

Figure 4.9 Variation of <grain size> with doping concentration of $Bi_{1-x}Ba_xFe_{1-y}Ti_yO_3$ (x = 0.1, y = 0.0; x = 0.2, y = 0.0; x = 0.3, y = 0.0; and x = 0.3, y = 0.1) ceramics for **1 hour holding time at the sintering temperature**. 73

Figure 4.10 Variation of <grain size> with doping concentration of $Bi_{1-x}Ba_xFe_{1-y}Ti_yO_3$ (x = 0.1, y = 0.0; x = 0.2, y = 0.0; x = 0.3, y = 0.0; and x = 0.3, y = 0.1) ceramics for **2 hours holding time at the sintering temperature**. 74

Figure 4.11 Microstructure development from as pressed to sintered condition of $Bi_{0.9}Ba_{0.1}FeO_3$ samples sintered using cycle-1. 76

Figure 4.12 Microstructure development from as pressed to sintered condition of $Bi_{0.8}Ba_{0.2}FeO_3$ samples sintered using cycle-1. 78

Figure 4.13 Microstructure development from as pressed to sintered condition of $Bi_{0.7}Ba_{0.3}FeO_3$ samples sintered using cycle-1. 79

Figure 4.14 Microstructure development from as pressed to sintered condition of $Bi_{0.7}Ba_{0.3}Fe_{0.9}Ti_{0.1}O_3$ samples sintered using cycle-1. 80

Figure 4.15 FESEM micrograph of $Bi_{1-x}Ba_xFe_{1-y}Ti_yO_3$ samples sintered at 850°C for 2 hours showing variation of <grain size> and %TD with doping concentration. 83

Figure 4.16 FESEM micrograph of $Bi_{1-x}Ba_xFe_{1-y}Ti_yO_3$ samples sintered at 850°C for 4 hours showing variation of <grain size> and %TD with doping concentration. 84

Figure 4.17 FESEM micrograph of $Bi_{1-x}Ba_xFe_{1-y}Ti_yO_3$ samples sintered at 875°C for 2 hours showing variation of <grain size> and %TD with doping concentration.. 86

Figure 4.18 FESEM micrograph of $Bi_{1-x}Ba_xFe_{1-y}Ti_yO_3$ samples sintered at 875°C for 4 hours showing variation of <grain size> and %TD with doping concentration. 87

Figure 4.19 FESEM micrograph of $Bi_{1-x}Ba_xFe_{1-y}Ti_yO_3$ samples sintered at 875°C for 6 hours showing variation of <grain size> and %TD with doping concentration. 88

Figure 4.20 XRD patterns at room temperature of $Bi_{1-x}Ba_xFe_{1-y}Ti_yO_3$ (x = 0.1, y = 0.0; x = 0.2, y = 0.0; x = 0.3, y = 0.0; and x = 0.3, y = 0.1) samples having optimum microstructure. 89

Figure 4.21 Variation of dielectric constant with doping concentration of $Bi_{1-x}Ba_xFe_{1-y}Ti_yO_3$ (x = 0.1, y = 0.0; x = 0.2, y = 0.0; x = 0.3, y = 0.0; and x = 0.3, y = 0.1) samples having optimum microstructure. 92

Figure 4.22 Variation of dielectric constant with temperature at different frequencies of $Bi_{1-x}Ba_xFe_{1-y}Ti_yO_3$ (x = 0.1, y = 0.0; x = 0.2, y = 0.0; x = 0.3, y = 0.0; and x = 0.3, y = 0.1) samples having optimum microstructure. 94

Figure 4.23 Variation of dielectric constant with frequency $Bi_{1-x}Ba_xFe_{1-y}Ti_yO_3$ (x = 0.1, y = 0.0; x = 0.2, y = 0.0; x = 0.3, y = 0.0; and x = 0.3, y = 0.1) samples having optimum microstructure. 95

Figure 4.24 Variation of dielectric loss with frequency $Bi_{1-x}Ba_xFe_{1-y}Ti_yO_3$ (x = 0.1, y = 0.0; x = 0.2, y = 0.0; x = 0.3, y = 0.0; and x = 0.3, y = 0.1) samples having optimum microstructure. 96

Figure 4.25 DTA analysis for $Bi_{1-x}Ba_xFe_{1-y}Ti_yO_3$ (x = 0.1, y = 0.0; x = 0.2, y = 0.0; x = 0.3, y = 0.0; and x = 0.3, y = 0.1) having optimum microstructure 97

Figure 4.26 The M-H loop of $Bi_{1-x}Ba_xFe_{1-y}Ti_yO_3$ (x = 0.1, y = 0.0; x = 0.2, y = 0.0; x = 0.3, y = 0.0; and x = 0.3, y = 0.1) samples having optimum microstructure. 99

Figure 4.27 Comparison of the M-H loops of $Bi_{1-x}Ba_xFe_{1-y}Ti_yO_3$ (x = 0.1, y = 0.0; x = 0.2, y = 0.0; x = 0.3, y = 0.0; and x = 0.3, y = 0.1) samples with that of pure BFO. 100

List of Tables

Table 3.1	Information of raw materials.	51
Table 3.2	Raw powder requirements for formulation of samples.	52
Table 3.3	Table showing experimental parameters applied.	55
Table 3.4	Theoretical densities of different composition.	56
Table 4.1	Percent theoretical density (%TD) and average grain size of $Bi_{1-x}Ba_xFe_{1-y}Ti_yO_3$ ceramics sintered at temperatures from 850 to 900°C.	65
Table 4.2	Key experimental results showing optimum sintering condition for all four compositions.	68
Table 4.3	Dielectric constant of $Bi_{1-x}Ba_xFe_{1-y}Ti_yO_3$ samples having optimum microstructure.	91
Table 4.3	Remnant magnetization and coercivity of $Bi_{1-x}Ba_xFe_{1-y}Ti_yO_3$ samples having optimum microstructure.	100

CHAPTER 1
INTRODUCTION

1.1 Background of the research

Multiferroics are multifunctional materials that exhibit more than one ferroic orders i.e. ferroelectricity, ferromagnetism, ferroelasticity and ferrotoroidicity in the same phase. Multiferroics particularly magnetoelectrics, in which spontaneous magnetic and dielectric ordering occur have fascinated scientists for centuries. They have a spontaneous magnetization that can be switched by an applied magnetic field, a spontaneous polarization that can be switched by an applied electric field, and often some coupling between the two [1]. Such materials have all the potential applications of both their parent ferroelectric and ferromagnetic materials which include spintronics, memory devices, sensors etc.

Among the very few multiferroic materials, bismuth ferrite ($BiFeO_3$) has been considered to be the most promising single phase candidate for practical applications, due to its high ferroelectric (FE) and anti-ferromagnetic (AFM)/ ferromagnetic (FM) transition temperatures, respectively $T_C \sim 1103$ K (Curie Temperature) and $T_N \sim 643$ K (Neel Temperature) [2-3]. These high transition temperatures allow the usage of $BiFeO_3$ (BFO) for devices in a wide range of temperature.

This Pure $BiFeO_3$ has a rhombohedrally distorted perovskite structure (ABO_3 type structure which belongs to the R3c space group) resulting in A-site polarization and a cycloid spin structure (at room temperature) [3-5]. The primitive unit cell contains two formula units (10 atoms) as shown in Figure 1.1. However, the high leakage current in pure BFO due to oxygen vacancy related defects reduces it‘s ferroelectric properties and the cycloidal spin structure results in zero net magnetization. So, pure BFO possesses weak ferroelectric and ferromagnetic order parameters. In this context, doping with ions having different ionic radius than Bi^{3+} (e.g. Ba^{2+}, Ca^{2+}) at A-site may distort the original structure of pure BFO, change the cycloidal spin structure to a canted spin structure, control grain growth and enhance both dielectric and ferromagnetic properties [5-13]. It has also been reported that, above an optimum A-site doping dielectric properties may deteriorate due to oxygen vacancy related defects. However, transition metal ions having higher charge than Fe^{3+} (e.g. Ti^{4+}) can be codoped at B-site to reduce oxygen vacancy related defects formed after A-site doping [7, 9 and 13].

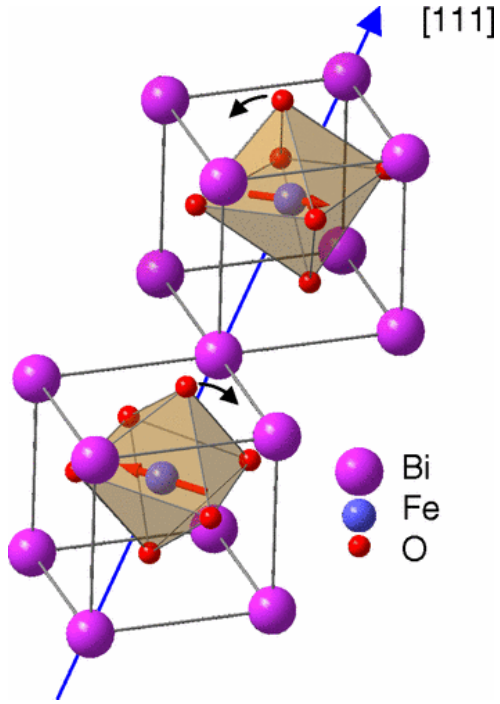

Figure 1.1: Schematic view of the R3c structure built up from two cubic perovskite $BiFeO_3$ unit cells. [The cations are displaced along the [111] direction relative to the anions, and the oxygen octahedral rotate with alternating sense around the [111] axis. In the ideal cubic perovskite structure the oxygen ions would occupy the face-centered sites.]

The current research thus will focus on studying structural characteristics, magnetic polarization, permittivity and also establishing the structure-property relationship of Ba^{2+} and Ti^{4+} doped $BiFeO_3$.

1.2 Motivation of the research

The most appealing matter about $BiFeO_3$ is the occurrence of both ferromagnetic and ferroelectric order simultaneously in a single phase. So, the motivation of research regarding $BiFeO_3$ multiferroics is that it could lead to a new generation of memory devices that can be electrically written and magnetically read, which means the advantages of FeRAMs (ferroelectric random access memories) and MRAMs (magnetic random access memories) could be combined in a single device [14, 15] . Moreover, as ferroelectric polarization and magnetization are used to encode binary information in FeRAMs and MRAMs respectively, the coexistence of magnetization and polarization in a $BiFeO_3$ multiferroic material allow the realization of four-

state logic in a single device. More complex schemes have even been proposed in order to store up to eight logic states.

Multiferroic magnetoelectric materials were studied extensively by Hans Schmid in Geneva from 1970 to 1990 with nickel iodine boracites as the paradigm material. A primary aim was to provide a memory element that had more than the two states used by Boolean algebra. A four-state logic (Figure 1.2), or even better, octal logic, would permit an exponentially increased computing capacity. Unfortunately the boracites function only at very low temperatures and generally grow in needle-form. Their study was never extended to thin films and was never commercialized.

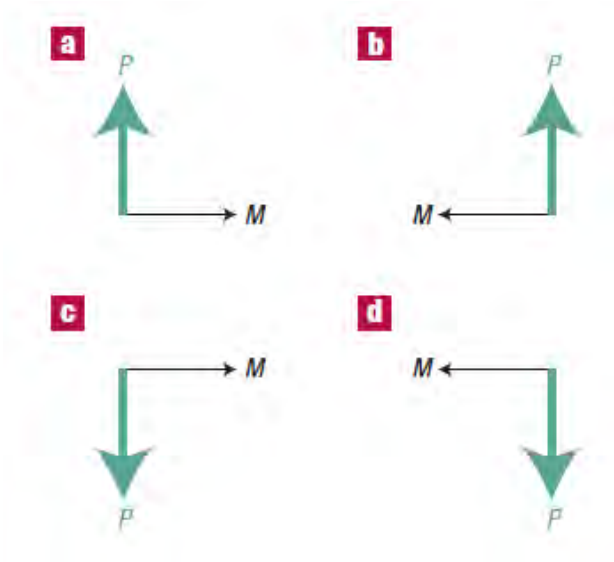

Figure 1.2: The four degrees of multiferroic order. a–d, Electric polarization P and magnetization M can assume four non-collinear states in a multiferroic crystal.

Recently, Gajek et al. exploit the large tunnel magnetoresistance in junctions (Figure 1.3) that have a ferromagnetic electrode. Notably, there is also an electroresistance effect influenced by the electric polarization P in the multiferroic barrier (blue). The combination of these two effects — magnetoresistance plus electroresistance — yields a four-state resistive memory element.

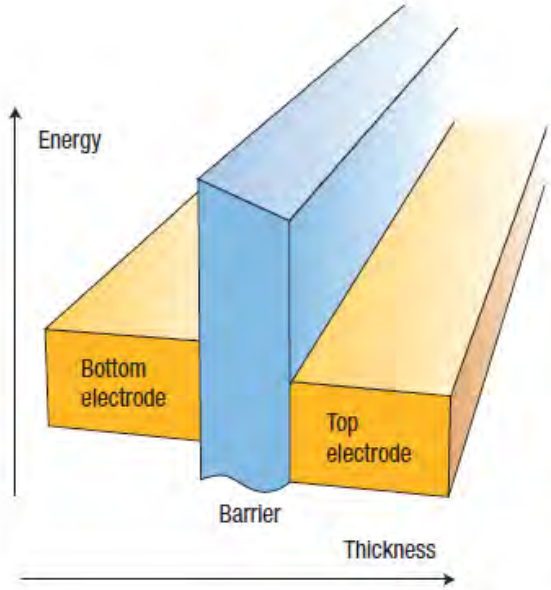

Figure 1.3: Schematic of a tunnel junction. Electrons tunnel from the bottom electrode through the barrier into the top electrode.

In order to make a multiple-state magnetoelectric memory, one must be able to access the four states formed by electric polarization P and magnetization M (Figure 1.2): (+P,+M), (+P,–M), (-P,+M), and (–P,–M). However, this is not just a matter of symmetry, but also of multiferroic coupling. If we wish to switch from (+P,+M) to (+P,–M) by applying an electric field, a significant P–M coupling is required. Unfortunately this implies that the four states are not truly independent. In the extreme limit in which the polarization and magnetization are fully coupled, only the states (+P,+M) and (–P,–M) — or only (+P,–M) and (–P,+M) — are accessible and this is, of course, not a four-state memory. Therefore, the kind of polarization–magnetization correlation studied by Gajek and co-workers is an important new topic and if applicable in real life devices would certainly permit an exponentially increased computing capacity.

Beyond the combination of ferroic properties in a single device, the electrical control of magnetization via the magnetoelectric coupling offers the opportunity of combining the respective advantages of FeRAMs and MRAMs in the form of non-volatile magnetic storage bits that are switched by an electrical field. Indeed, although the characteristics of MRAMs equal or surpass those of alternative non-volatile memory technologies in terms of access time and endurance, they have a large handicap in their high writing energy. A possible solution for

reducing the writing energy uses a spin-polarized current to reverse the magnetization of the storage layer by spin-transfer rather than magnetic fields. Spin-transfer MRAMs are currently being developed by several companies and a 2 Mb memory was recently demonstrated.

An alternative solution that could drastically reduce the writing energy of MRAMs is the use of a write scheme based on the application of a voltage rather than large currents. The magnetoelectric coupling in multiferroics provides such an opportunity. The basic operation of such magnetoelectric random access memories (MERAMs) combines the magnetoelectric coupling with the interfacial exchange coupling between a multiferroic and a ferromagnet to switch the magnetization of the ferromagnetic layer by using a voltage (Figure 1.4).

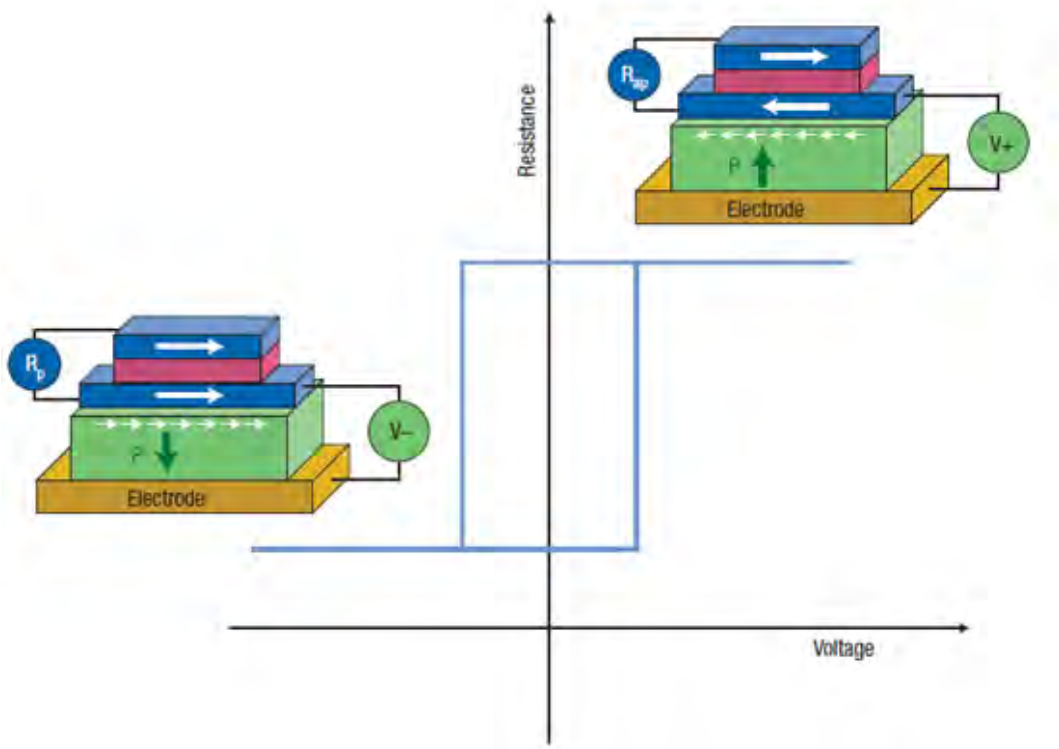

Figure 1.4: Sketch of a possible MERAM element [15]. [The binary information is stored by the magnetization direction of the bottom ferromagnetic layer (blue), read by the resistance of the magnetic trilayer (Rp when the magnetizations of the two ferromagnetic layers are parallel), and written by applying a voltage across the multiferroic layer (green). If the magnetization of the bottom ferromagnetic layer is coupled to the spins in the multiferroic (small white arrows) and if the magnetoelectric coupling is strong enough, reversing the ferroelectric polarization P in the multiferroic changes the magnetic configuration in the trilayer from parallel to antiparallel, and the resistance from Rp to antiparallel (Rap). A hysteretic dependence of the device resistance with voltage is achieved (blue curve).]

In MERAMs, the magnetoelectric coupling enables an electric field to control the exchange coupling at the interface of the multiferroic with the ferromagnet. The exchange coupling across the interface then controls the magnetization of the ferromagnetic layer, so that ultimately this magnetization can be switched by the electric polarization of the multiferroic. Driven by the directional coupling occurring at the interface between a ferromagnet and a multiferroic, Binek and Doudin suggested focusing on exchange bias, This proposal triggered much activity in the search for exchange bias using multiferroics, its connection to ferroelectric properties and ultimately its electrical control.

The number of multiferroics that could be used for MERAMs is quite limited, and so far only $BiFeO_3$ has emerged as a potential candidate. In BFO, the ferroelectric polarization and the ferromagnetic vector are coupled, so that reversing the polarization by an electric field also rotates the magnetic spins. In line with the above MERAM scheme, Chu et al. show that the ferromagnetic domain structure of CoFe micrometre-size elements deposited on top of a BFO film also exhibits a systematic coupling with the magnetic spins in BFO. Therefore, when an in-plane electric field is applied, the magnetic domain structure of the CoFe dots is modified. The original magnetic state is recovered when a voltage with opposite polarity is applied. This result is an essential step towards the fabrication of prototype MERAM elements that are reproducibly switched by an electric field.

Now, the next step is to realize a full MERAM element where the electrical resistance of a spintronics device is controlled with a multiferroic. Nevertheless, the control of magnetism by a multiferroic achieved by Chu and colleagues is certainly a testament to the rude health of this field, and extends the potential of multifunctional oxides for novel devices.

Several issues should however be solved before realization in devices. The problems are high leakage current density and cycloidal magnetic spin structure. Many attempts have been made to enhance the ferroelectric and ferromagnetic properties of BFO via ion substitution. The current research deals with finding the effect of Ba^{2+} and Ti^{4+} doping on the multiferroic properties of $BiFeO_3$.

1.3 Aims of the research

The main aims of this research include:

(i) To improve the room temperature magnetic property by modifying the rhombohedrally distorted perovskite structure of $BiFeO_3$ using Ba^{2+} and Ti^{4+} as dopants.

(ii) To stabilize the dielectric property of $BiFeO_3$ by controlling grain growth and reducing oxygen vacancy related defects (leakage current) using the dopants.

(iii) To determine optimum sintering condition for each doped compositions that will result in less porous and dense microstructure.

(iv) To correlate the structural characteristics with the multiferroic properties of $BiFeO_3$.

1.4 Current research trends

Pure BFO has some inherent problems: (a) Large number of oxygen vacancies produced due to highly volatile nature of Bi and the multiple oxidation states of Fe (Fe^{2+} and Fe^{3+}) cause a high leakage current in the material that degrades its ferroelectric properties [10-12]. (b) On the other hand, the localized ferromagnetism produced by the canting of spins in $BiFeO_3$ vanishes at macroscopic level due to the cycloidal spin structure [8-13].

In order to overcome the problems associated with BFO, many attempts have been made recently, which include:

(i) Doping with divalent ions (example: Ba^{2+}, Ca^{2+} etc) or rare earth ions (La^{3+}, Nd^{3+}or Sm^{3+}) at A-sites for substituting part of Bi^{3+} and transition metal ions (example: Ti^{4+}, Mn^{4+} etc) at B-sites for substituting part of Fe^{3+}; [16-18].

(ii) Fabricating a composite of BFO with other ABO_3 perovskite materials, such as $BaTiO_3$ [19].

(iii) Fabricating high quality single crystal of $BiFeO_3$ to solve non-stoichiometric problems [20].

(iv) Synthesizing $BiFeO_3$ nano particles with grain size below 62 nm to achieve ferromagnetism by destroying spiral spin structure [21].

(v) Depositing ultra-thin $BiFeO_3$ single layer or multilayer films to enhance ferroelectric property; [22].

Among these approaches, it has been proved that A-site and B-site substitution is an efficient way to improve both the ferromagnetic and ferrelectrictic properties of BFO.

1.5 Recent works on A-site and B-site doping of BFO

Long known to be both antiferromagnetic—its magnetic moments align in opposing directions, so that the net magnetization is zero—and ferroelectric, bismuth ferrite is multiferroic in the popular use of the term. Since it is readily synthesized in bulk and thin-film forms and both its anti - ferromagnetic Néel temperature and ferroelectric Curie temperature are well above room temperature (approximately 643 K and 1103 K, respectively) it is undoubtedly the most studied multiferroic today.

When the scientists first became interested in $BiFeO_3$ in the late 1990s, the only published ferroelectric measurement—performed on a bulk polycrystalline sample—reported a rather small value for the ferroelectric polarization, around 6 $\mu C/cm^2$. That value struck all as somewhat curious, since the lone pair of electrons on the Bi^{3+} ions should lead to large local dipole moments [23].

The current interest in bismuth ferrite was stimulated primarily by a 2003 paper from Ramesh‘s group,[24] which showed that it had unexpectedly large remnant polarization, P_r, 15 times larger than previously seen in bulk, together with very large ferromagnetism of ca. 1.0 Bohr magneton (μ_B) per unit cell. Single crystals grown more recently in France in 2006–7 have confirmed the large value of the polarization first observed in the films, showing also that it is intrinsic;[23] At any rate, the 2003 Science paper has proved enormously stimulating, and has inspired both new fundamental physics and exciting device applications.

Several attempts have been made to reduce the leakage current and to improve the ferromagnetic property of pure BFO by adding proper dopants. In 2005 Xiaoding et al. [25] investigated the transport properties of aliovalent-ion-doped $BiFeO_3$ thin films in order to identify the cause of high leakage currents. Doping of 2 atomic weight % Ti^{4+} ions increased the dc resistivity by more than three orders of magnitude. In contrast, doping of 2+ charged ions such as Ni^{2+} reduced the dc resistivity by two orders of magnitude. Current–voltage (I–V) characteristics indicated that the main conduction mechanism for pure and Ni^{2+} doped BFO was space charge limited, which was associated with the free-carriers trapped by the oxygen vacancies, whereas in the Ti^{4+} doped BFO, field-assisted ionic conduction was dominant.

In 2006 Wang et. al. [12] investigated the effect of Ba doping on magnetic, ferroelectric, and magnetoelectric properties on $BiFeO_3$ at room temperature. Ba doped $BiFeO_3$ compounds were prepared by a solid-state reaction. X-ray diffraction showed that $Bi_{1-x}Ba_xFeO_3$ was single phase up to x = 0.25. These samples exhibited magnetism and ferroelectricity simultaneously at room temperature. The magnetic hysteresis loops of $Bi_{1-x}Ba_xFeO_3$ (x=0.15, 0.25) at room temperature are shown in Figure 1.5. The magnetoelectric coupling was also evidenced by the increase of the dielectric constant with the increase of the applied magnetic field.

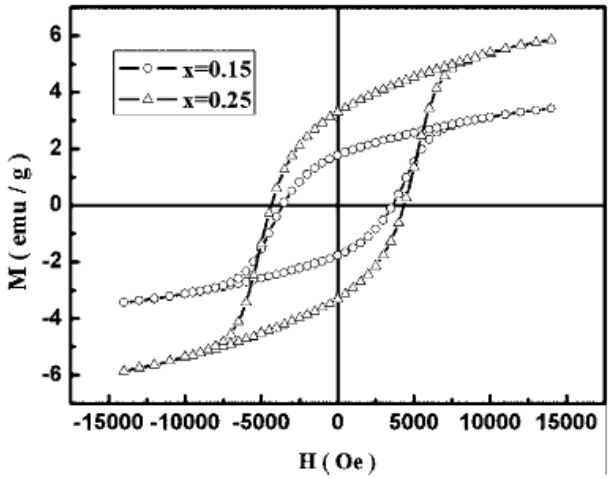

Figure 1.5: Magnetic hysteresis loops of $Bi_{1-x}Ba_xFeO_3$ (x=0.15, 0.25).

In 2007 Yuan-Hua et al. [11] studied the enhancement of ferromagnetic properties in $BiFeO_3$ polycrystalline ceramic by La doping. The authors present the structure transformation and magnetic properties of $Bi_{1-x}La_xFeO_3$(x=0.0–0.15) ceramics prepared by a conventional solid-

state reaction processing. Magnetic measurements reveal that remnant magnetization of 15% La-doped $BiFeO_3$ has enhanced about 20 times as compared to pure $BiFeO_3$. It is the structural phase transition from rhombohedral R3c to orthorhombic C222 near x=0.15 that destructs the spin cycloid, and thus enhances the ferromagnetic properties significantly. In these $Bi_{1-x}La_xFeO_3$ ceramic samples, besides the known antiferromagnetic Néel temperature $T_{N1} \sim 615$ K, another Néel temperature $T_{N2} \sim 260$ K can be observed due to the trace impurity phase of $Bi_2Fe_4O_9$ in these ceramic samples.

However, in 2008 Khomchenko et.al. [26] compared the mechanism of defects formation and their influence on the crystal structure and magnetic properties of diamagnetically substituted $Bi_{1-x}A_xFeO_3$ (A = Ca, Sr, Pb, Ba; x = 0.2, 0.3) multiferroics. For both antiferromagnetic and weak ferromagnetic compounds, A^{2+} substitution was realized through the formation of oxygen vacancies, suggesting that the observed effect of the suppression of spiral spin modulation is of intrinsic nature. Magnetization measurements showed that the magnetic state of the solid solutions depends strongly on the ionic radius of the substituting elements. A-site substitution with the biggest ionic radius ions was found to effectively suppress the spiral spin structure of $BiFeO_3$ giving rise to the appearance of weak ferromagnetism. This indicated a possible way of improving multiferroic properties of $BiFeO_3$-based magnetic ferroelectrics. Ba^{2+} having much higher ionic radius than Bi^{3+} attracted the researchers as a potential dopant to improve the multiferroic property of BFO since then.

In 2010, Gautam et al. [27] reported the dielectric, magnetic and ferroelectric properties of $Bi_{1-x}Ba_xFeO_3$ (x= 0.1, 0.2 and 0.3) synthesized by solid state reaction method. Ba substitution led to a decrease in grain size and hence an increase in the electrical resistivity. The substitution of Bi with Ba led to increase in polarization upto x=0.2. Further increase in Ba concentration decreased the polarization value due to the formation of oxygen related defects. Room-temperature measurements of the magnetization of $Bi_{1-x}Ba_xFeO_3$ (x = 0.1-0.3) compounds as a function of the applied magnetic field showed spontaneous magnetization appears in all Ba doped compounds and increase in magnetization value was observed with increase in Ba doping (Figure1.6).

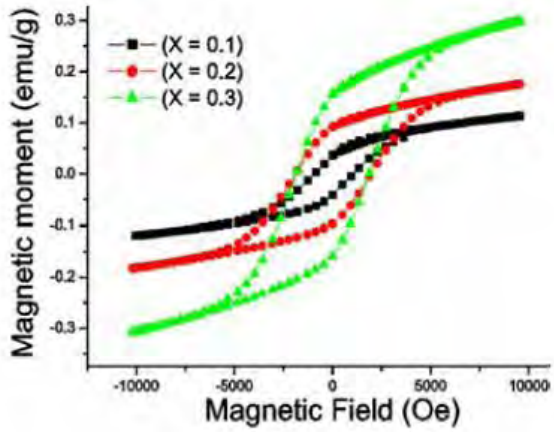

Figure 1.6: M-H loops of $Bi_{1-x}Ba_xFeO_3$ (x=0.1, 0.2 and 0.3) samples.

In 2012 Rajasree Das et. al. [6] also reported the magnetic, ferroelectric and magnetoelectric properties of Ba-doped $BiFeO_3$. Room temperature P vs. E loops of $Bi_{1-x}Ba_xFeO_3$ (x = 0.1, 0.15, 0.2 and 0.25) samples (Figure 1.7) showed that leakage current decreases up to x=0.2 samples resulting in good polarization value. Although $Ba_{0.25}$BFO showed higher polarization compared to that of others, the observed roundish hysteresis loop was due to a large leakage current which can overshadow the real contribution from reorientation of electrical dipoles.

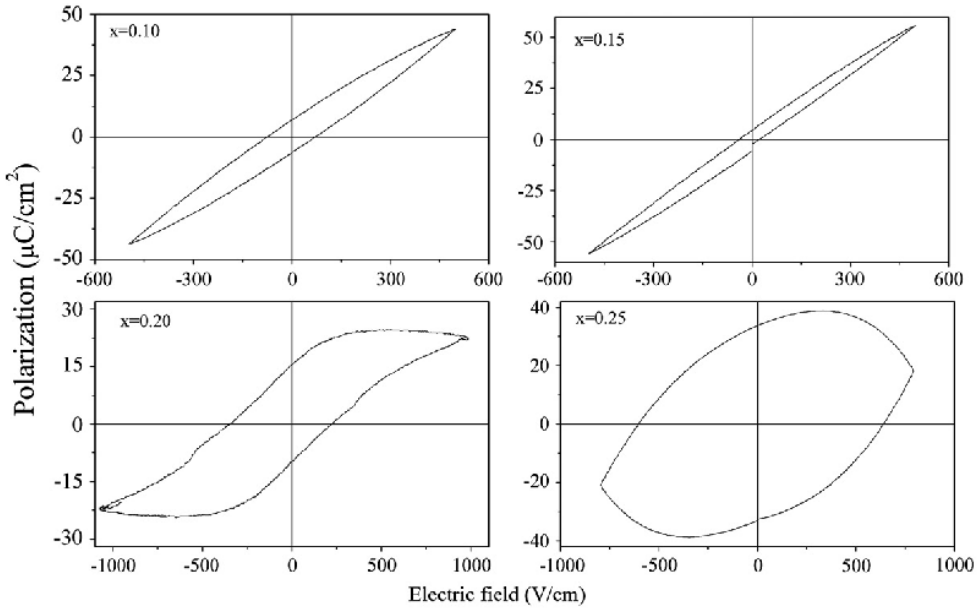

Figure 1.7: P-E loops of $Bi_{1-x}Ba_xFeO_3$ (x=0.1, 0.15, 0.2 and 0.25) samples.

In these works although the magnetization of $Bi_{1-x}Ba_xFeO_3$ was found to increase with increasing Ba doping but the dielectric value decreased above optimum doping of Ba (x=0.2) due to formation of oxygen vacancy related defects.

However, previous works report that B-site doping with a higher charged ion than Fe^{3+} can be applied to improve the dielectric value of $Bi_{1-x}Ba_xFeO_3$ by reducing oxygen ion related defects. In 2010, S.J. Kim et. al. [7] reported the effect of Ti doping at B-site of $BiFeO_3$. The results showed reduced dielectric loss and enhanced ferroelectric saturation and magnetic behavior in Ti doped samples relative to pure BFO. The partial substitution of Ti with a higher valence at Fe sites led to reduction in oxygen vacancies and to a change in the antiferromagnetic structure, resulting in enhanced electric properties and net magnetization, respectively.

From the work of previous researchers it is evident that A-site and B-site doping is a good way to improve the multiferroic properties of BFO, both in films and bulk ceramics [26-28]. The current work mainly aims to find the effect of Ba doping on the multiferroic properties of BFO. Furthermore, the research attempts to reduce the oxygen vacancy related defects and thereby stabilize the ferroelectric properties of $Bi_{1-x}Ba_xFeO_3$ samples above the optimum A-site doping concentration by adding Ti at B-site. Although Haoliang Deng et. al. [29] recently investigated the dielectric and ferroelectric property of Ba and Ti codoped BFO (2014), but the work was not focused on reducing leakage current of $Bi_{1-x}Ba_xFeO_3$ above the optimum doping concentration. Also, no investigations on Ba^{2+} or Ti^{4+} doped bulk BFO materials has been reported to optimize the microstructure of doped samples by using proper sintering conditions. So, optimizing the microstructure of each doped compositions by preparing fine grained (~1μm) and dense (> 95percent theoretical density) samples was also a prime focus of this research.

1.6 Targets and challenges of this thesis

The main focus of this research is to improve the room temperature ferromagnetic properties by modifying the rhombohedrally distorted perovskite structure of $BiFeO_3$ using Ba^{2+} as dopants and thereby changing the cycloid spin structure to a canted spin structure. Furthermore, dielectric property is also aimed to be stabilized by controlling grain growth and reducing oxygen vacancy

related defects. Oxygen related vacancies formed after optimum A-site doping can also be controlled by adding Ti at B-site. Moreover, the research focus on determining the optimum sintering condition of doped BFO samples that will result in fine grained dense samples for all compositions**.**

The A-site substitution by barium ion (Ba^{2+}) has been attempted by many authors in recent years to enhance the multiferroic properties of $BiFeO_3$. Ba^{2+} having a large ionic radius of Bi^{3+} distorts the original structure of $BiFeO_3$ and changes it‘s cycloidal spin structure to a canted spin structure resulting in net magnetization at room temperature. Moreover, addition of Ba^{2+} also significantly reduces the oxygen vacancy related defects (leakage current) by occupying evaporated Bi sites and increases the electrical resistivity of BFO by controlling grain size, thus allowing high dielectric constant to be determined at room temperature [30].

So, we may expect an increase in ferromagnetic properties of BFO with increasing Ba concentration due to structural distortion. However, the substitution of Ba^{2+} for Bi^{3+} may cause two parallel phenomena with respect to concentration of oxygen vacancies [30], one is decrease in concentration of oxygen vacancies by filling the probable vacant volatized Bi^{3+} sites and the second is the creation of oxygen vacancies to neutralize the charge produced by substituting Ba^{2+} for Bi^{3+}. When all the vacant Bi^{3+} sites are filled up at a certain doping level of Ba^{2+}, addition of excessive Ba^{2+} creates oxygen vacancies by substituting Bi^{3+} ions due to its lower charge (+2) than the bismuth ion (+3). Hence, we may consider a decrease in leakage current up to an optimum Ba doping and then an increase in leakage current on further doping. To reduce the oxygen vacancy related defects formed after optimum Ba doping at A-site, a higher charged ion than Fe^{3+} (i.e. Ti^{4+}) can be doped at B-site.

So, it is interesting to investigate the effect of -doping of Ba and Ti on the microstructure and multiferroic properties of $BiFeO_3$. Moreover, no work based on Ba or Ti doped BFO has been conducted previously in our department. On this point of view, this work imposes an entirely a new challenge. In addition the limitation of technical facilities further confines the scope of working. However the work, if carried out successfully, has the potential to yield materials with superior ferroelectric and ferromagnetic properties, thereby offering the potential to revolutionize

the application of electromagnetic materials. From this aspect the research is definitely exciting and commendable of being followed.

As the preparation of the compacts is simple, the biggest challenge is to achieve very fine grain structure with minimum porosity. On this occasion the toughest task is to find the optimum sintering temperature which will bring the desired microstructure. Control of the geometry of samples is another challenge to take over. Since this is attributed entirely on the rate of heating and cooling during sintering, the heating/cooling rate needs to be optimized as well.

One important thing here is the use of powder which has a size in nanometer range. Such powders possess very high surface energy and consequentially, are more reactive than coarser powders. Hence the sintering temperature needs to be modified accordingly.

CHAPTER 2
LITERATURE REVIEW

2.1 Introduction

An introduction to primary ferroics is mentioned in Section 2.2 while possible couplings between ferroic orders are discussed in Section 2.3. Multiferroics and their types are mentioned in Section 2.4 and the most important single phase multiferroic $BiFeO_3$ (BFO) is presented systematically in Section 2.5.

2.2 Primary ferroics

Ferro- is a prefix which means iron in Latin, it is primitively used to describe materials exhibiting strong magnetic properties as iron does. Apart from iron, other elements like cobalt, nickel and rare earth elements also exhibit magnetic behavior called ferromagnetism, which enables materials made from the above-mentioned elements to form permanent magnets. Ferromagnetic materials were reported to have a long-range ordering phenomenon at the atomic level. Many small domains can be found in a magnetic material with plenty of unpaired electrons inside. Microscopically, those unpaired electrons are not randomly alligned, they interact with others to make the alignment in the same direction within the same domain. However, these domains are randomly aligned so that on the whole, they cancel out to make zero magnetism. When an external magnetic field is applied, those domains with the magnetic field grow at the expense of their neighbouring domains, causing materials to be magnetized. This phenomenon is characterized by a hysteresis loop of magnetization M as a function of external magnetic field H, as illustrated in Figure 2.1 (a). It is obvious that the magnetization is saturated at high magnetic field and a remnant magnetization can still exist in the absence of the field. In addition, the direction of magnetization could be reversed provided that the external magnetic field is switched oppositely with quite strong field intensity.

However, the ferromagnetic material can lose its ferromagnetic properties under thermal agitation, the temperature that characterizes this phenomenon is known as the ―Curie temperature (Tc)", above which spontaneous ferromagnetism becomes paramagnetism which owns a small, positive susceptibility to magnetic fields and can‘t keep this magnetic properties after removal of

the external field. When such a material is cooled down and crosses the Curie temperature, it undergoes a phase transition from a non-ferroic to ferroic state. These transitions are generally accompanied with a lowering of the crystal symmetry. For example bulk $BaTiO_3$ an archetypal ferroelectric presents a transition from a cubic paraelectric structure to a tetragonal ferroelectric structure around 120°C.

Ferroelectricity and ferroelasticity are other ferroic orders which are analogous to ferromagnetism. Polarization and strain are induced by externally applied electric field and mechanical stress respectively. They both show hysteresis loops with spontaneous electric polarization and strain, as depicted in Figure 2.1 (b) and (c**).** Figure 2.2 shows how ferroelectrics and ferromagnetics permit the orientations of electrical polarization and magnetization to be reversed by applying an electric field and magnetic field, respectively.

Actually, the discovery of ferroelectricity can date back to the early 20th century when ferromagnetism had already been discovered. Since the appearance of hysteresis loops from ferroelectricity and ferromagnetism look quite similar, the prefix ferro- was continuously carried forward to describe ferroelectricity, though many ferroelectric materials have nothing to do with iron either.

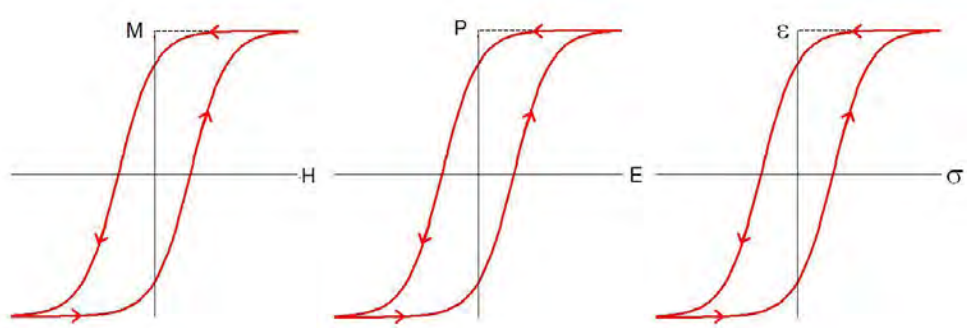

Figure 2.1: Hysteresis loops of (a) ferromagnetic, (b) ferroelectric and (c) ferroelastic materials.

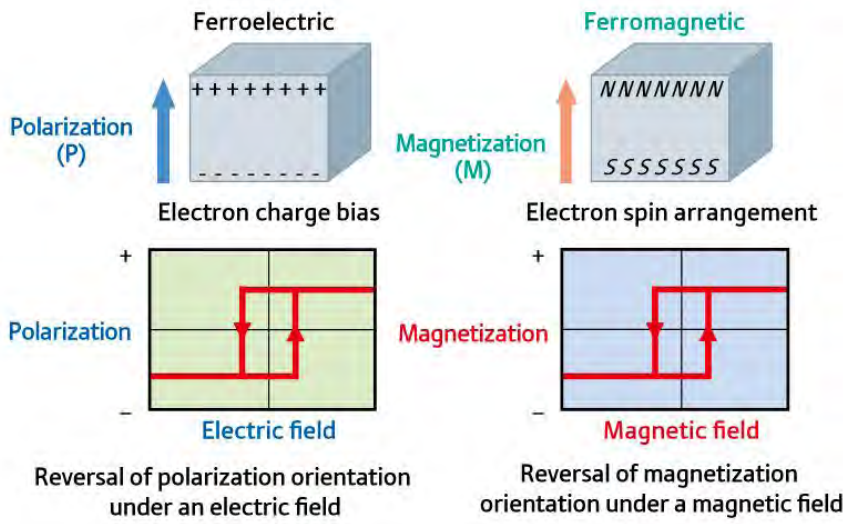

Figure 2.2: Schematic representation of ferroelectric and ferromagnetic characteristics. [Ferroelectrics and ferromagnetics permit the orientations of electrical polarization and magnetization to be reversed by applying an electric field and magnetic field, respectively.]

However, there exists another ferroic order named ferrotoroidicity which include materials that possess a stable and spontaneous order parameter that is taken to be the curl of a magnetization or polarization. On the basis of above discussion, we can conclude that there are four primary ferroic order parameters. They are:

- **Ferroelectricity**
- **Ferromagnetism**
- **Ferroelasticity**
- **Ferrotoroidicity**

In the following discussion, concepts of the ferroelectrics and ferro (ferri) magnetic materials will be discussed in detail.

2.2.1 Ferroelectric materials

Ferroelectricity (FE) was first discovered in Rochelle salt in 1921. At that time, it was called Seignette-electricity, honoring its discoverer. For the past few decades, ferroelectric materials have received a great amount of interests because of their various uses in many applications such

as nonvolatile ferroelectric random access memories (NVFRAM), dynamic random access memories, sensors and microactuators [31].

A crystal is said to be ferroelectric when it possesses at least two equilibrium orientations of the spontaneous polarization vector in the absence of an external electric field, and the spontaneous polarization can be switched between those orientations by an electric field. The polar character of the orientation states should represent an absolutely stable configuration in a null field [32].

It is well known that crystals can be classified into thirty-two crystal classes (point groups) according to the symmetry elements they possess. Among these thirty-two crystal classes, eleven of them are characterized by the existence of a center of symmetry: they are thus centrosymmetric. A centrosymmetric crystal cannot posses any polar properties. The remaining twenty-one crystal classes do not have a center of symmetry; thus, it is possible for them to (i) have one or more polar axes, (ii) possess odd-rank tensor properties. With one exception, all non-centrosymmetric point groups exhibit piezoelectric effect that is defined by a change in electric polarity under applied stress, and vice versa, that is the converse piezoelectric effect.

Out of the twenty piezoelectric classes, ten possess a unique polar axis. Crystals in these classes are called polar because they are spontaneously polarized. The value of the spontaneous polarization depends on temperature. When temperature changes, a change in the polarization occurs and electric charges can be observed on those crystal faces perpendicular to the polar axis. This is called the pyroelectric effect. The ten crystal classes with a unique polar axis are also called pyroelectric classes. Ferroelectric crystals belong to the pyroelectric family, but they only constitute the part that the direction of the spontaneous polarization can be reversed by external electric field.

So, a (proper) ferroelectric possesses a spontaneous polarisation of the electric dipole due to a lack of inversion symmetry within the crystal structure. For example, consider the most extensively studied and widely used classic perovskite of the form ABO_3, in which a central positive B-ion (a transition metal element) is surrounded by an octahedron of negatively charged oxygen ions (Figure 2.3). A shift in the position of the B-site ion would break the inversion

symmetry and cause the induction of a dipole moment, giving rise to ferroelectric order. Such shifts can occur during structural phase transitions, in which the system moves from a high to low symmetry state (e.g. cubic to tetragonal). In the majority of ferroelectric perovskites, the B-site atom has an empty d electron shell, which allows covalent bonding with the full p orbitals of the oxygen atoms. One of the best known examples of a proper ferroelectric is $BaTiO_3$. As shown in Figure 2.3, the Ba^{2+} cations are located at the corners of the unit cell. A dipole moment occurs due to relative displacements of the Ti^{4+} from their symmetrical positions.

Ferroelectricity can also occur due to the existence of lone pairs of electrons on the outer shell of the A-site atom, which are highly susceptible to polarisation. This is the cause of ferroelectricity in $BiFeO_3$. Whether A-site or B site polarization would occur depends on Goldschmid Tolerance Factor, $t=(r_{A\text{-site}}+r_O)/\sqrt{2}(r_{B\text{-site}}+r_O)$; where $t>1$ results in A-site polarization.

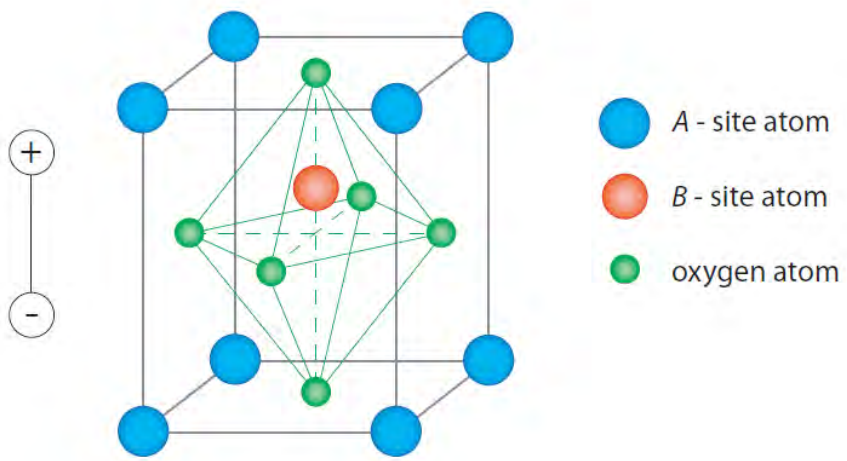

Figure 2.3: Perovskite crystal structure, showing a dipole moment generated by a displaced B-site atom.

In an improper ferroelectric, the spontaneous polarisation is not due to a polar displacement of the ions, but occurs as a result of some other effect within the material. In a geometric ferroelectric, the dipole moment occurs due to non-polar lattice distortions, due to e.g. electrostatic forces rather than changes in chemical bonding. An example of this is in $YMnO_3$, where a ferroelectric state is due to a buckling of the rigid MnO_5 bipyramids. In charge ordered ferroelectrics, the spontaneous polarisation is dependent on electron correlations in the material.

Such charge ordered ferroelectricity is observed in $LuFe_2O_4$. Improper ferroelectricity can also occur due to magnetic order.

2.2.2 Ferro-, antiferro-, and ferri-magnetic materials

The phenomenon of magnetism has been known to mankind for many thousands of years. Lodestone (Fe_3O_4) was the first permanent magnetic material to be identified and studied. The magnetic moment of an atom/ion has three principal sources: (1) the spin of electrons; (2) electron orbital angular momentum about the nucleus; and (3) a change in the orbital moment induced by an applied magnetic field. The first two effects give paramagnetic contributions to the magnetization, and the third gives a diamagnetic contribution [33].

In a crystal, the overall magnetic property depends on two factors: (i) the magnetic moment associated with each atom/ion, and (ii) the interactions between these magnetic moments. In the case that there are no unpaired electrons around each atom/ion, there will be no net magnetic moments associated with them (bearing in mind that both orbital moments and electron spins cancel to zero in a fully filled orbital), the material will show diamagnetic behavior. When there are unpaired electrons, every atom/ion has a net magnetic moment and depending on the interactions between the magnetic dipoles, the material may show (i) paramagnetism (PM); (ii) ferromagnetism (FM); (iii) antiferromagnetism (AFM) and (iv) ferrimagnetism (FIM). In a paramagnetic material, alignment of adjacent moments is observed only under applied magnetic field. Ferromagnetism consists of parallel aligned adjacent moments. Antiferromagnetic order consists of antiparallel aligned equal moments. And, ferrimagnetic order consists of antiparallel unequal moments, resulting in a non-zero net magnetization.

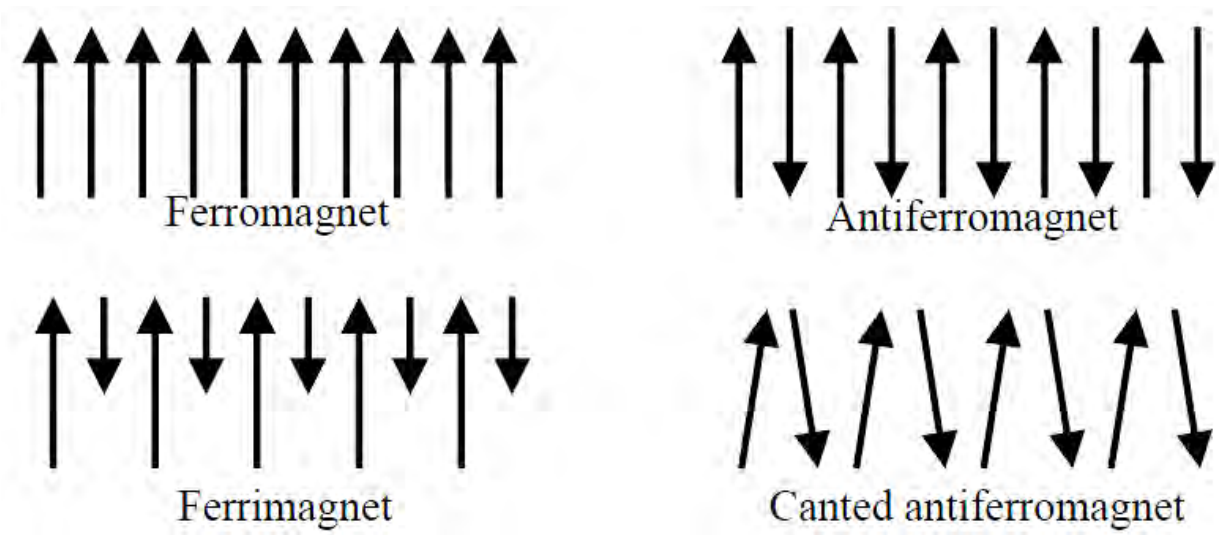

Figure 2.4: Common examples of magnetic dipole ordering.

Ferromagnetism is a very strong magnetic response compared with paramagnetic and diamagnetic behaviors. It is characterized by a transition temperature (Neel temperature, T_N).Above this temperature, the material is paramagnetic. Below this temperature, it is ferromagnetic.

A material‘s magnetic property can be understood from the M or B versus H curves, called the magnetization curves.

The magnetic induction (B) is the response of a material to the applied magnetic field (H). The relationship between B and H depends on the material; The magnetization (M) is defined as the magnetic moment per unit volume such that,

$$M = \chi.\ H \text{ and } B = \mu.\ H;\ \chi = \text{susceptibility and } \mu = \text{permeability}$$

From Figure 2.7a, we observe that the net magnetization of diamagnetic, paramagnetic and antiferromagnetic materials is very low even at a very high applied magnetic field and the relationship between M and H is linear. But, in ferromagnetic and ferrimagnetic materials, even at a low applied magnetic field, the value of magnetization is very high. Moreover, the M − H

curve is non-linear, and the magnetization saturates at higher values of H as shown in Figure 2.7b.

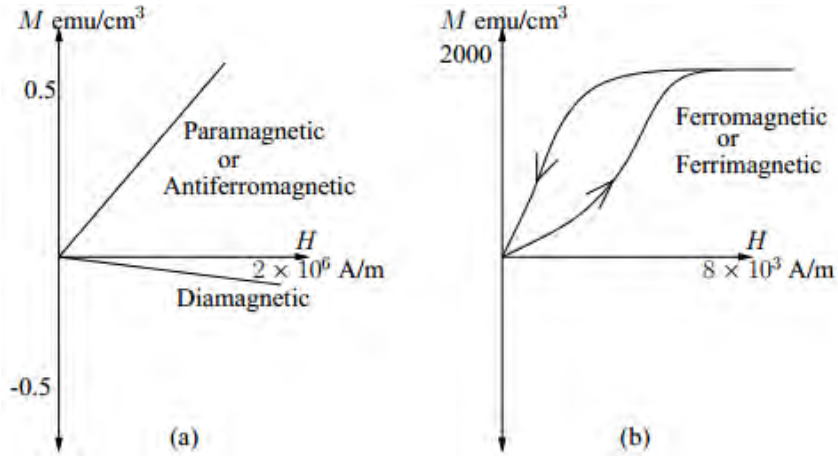

Figure 2.5: M-H curves for (a) diamagnetic, paramagnetic, antiferromagnetic (b) ferromagnetic and ferromagnetic materials. (N.A. Spaldin 2003)

All ferromagnetic and ferrimagnetic materials exhibit the phenomenon of hysteresis as shown in the four quadrant hysteresis loop in Figure 2.6. The performance of any magnetic material can be defined with the help of this hysteresis loop. M_s is the saturation magnetization and is a measure of how strongly the material can be magnetized. M_r is the remanent magnetization which is the residual, permanent magnetization left after the removal of the applied field. In order to demagnetize the specimen from its remanent state, a reverse field H_c, the coercive field is required to reduce the residual magnetization to zero. Higher the value of H_c, larger is the retaining capacity of the material. This is the reason that, the PL in an MTJ is with a larger coercivity, so that it requires a larger field to change its magnetization than the FL. Even ferromagnetic materials become paramagnetic, with random orientation of moments, above Neel temperature, T_N.

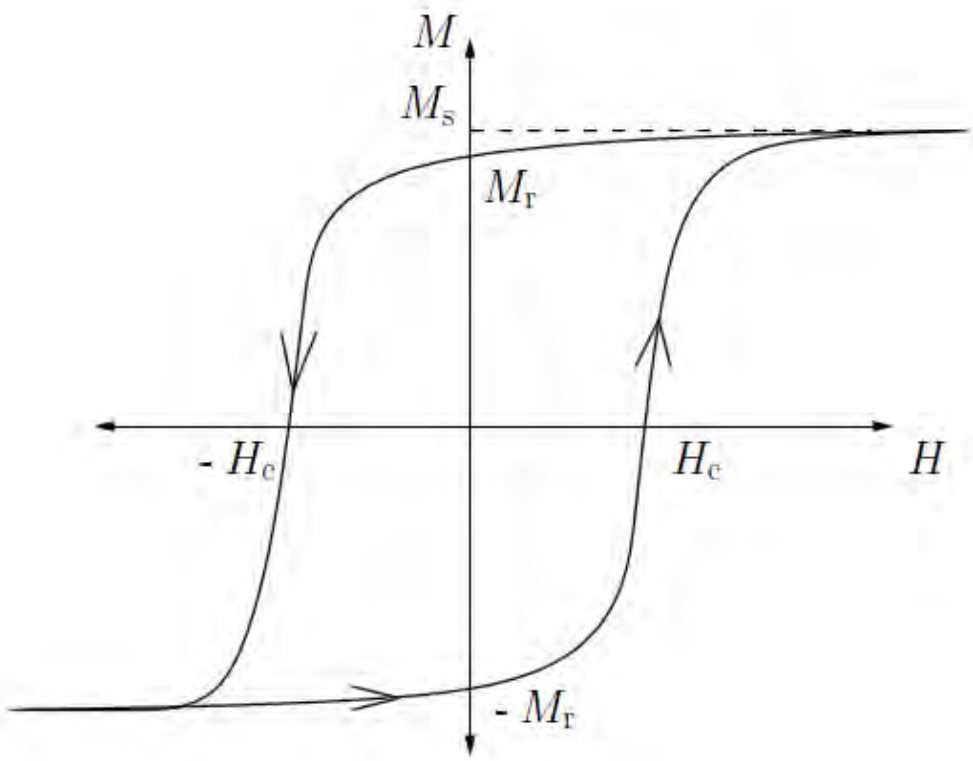

Figure 2.6: M-H curves for ferromagnetic and ferrimagnetic materials.

2.2.3 Ferroelastic material

Ferroelastic materials develop a spontaneous strain below a phase transition temperature. From the symmetry point of view, the material undergo a structural phase transition from a high symmetry phase to a low symmetry phase, which is characterized by a _broken symmetry‘ of the high symmetry phase [34].

The phase transition mechanism results in a spontaneous strain. The spontaneous strain can be quite large. For example, the spontaneous strain of a typical ferroelastic material is >2%. The correlated changes in the enthalpy of the crystal related to this formation of spontaneous strain often reach some 6 KJ/mole, an energy which would reactive equivalent changes in thermochemical phase diagrams of some hundreds of degrees in temperature. In order to release

the energy created by the phase transition, a twin domain structure is often created within a ferroelastic crystal, where the dominant twin planes are oriented approximately perpendicular to each other.

A wall between two adjacent domains can be envisaged as an internal surface of the crystal. The orientation of an individual twin wall is then determined by the condition that the crystal in the low-symmetry phase tends to maintain the total symmetry of the high-symmetry phase as an average. The domains are related equivalent to each other via the symmetry element lost at the phase transition that give rise to the long-range ordered state. It is commonly accepted that stress induced domain wall motion in ferroelastic materials yield hysteretic macroscopic behavior. Mueller et al. [35] showed that nonlinear effects in ferroelastic crystals are related to the properties of ferroelastic domain walls pinned on defects, which became de-pined above a critical stress level. Additionally, Jian and Wayman [36] observed domain wall motion in single-crystal and polycrystalline $LaNbO_4$ ferroelastics under stress, and argued that the nonlinear elastic behavior is a direct result of domain wall motion, rather than the intrinsic properties of the crystal. In addition, Newnham [37] concluded that stress-induced movement of domain walls is the principle source of hysteresis in ferroelastics. A complete analysis of twin structure and domain wall can be seen in reference [35].

Figure 2.7 illustrates the stress-induced twin movement of a ferroelasteic $Pb_3(Pb_4)_2$ crystal [35].

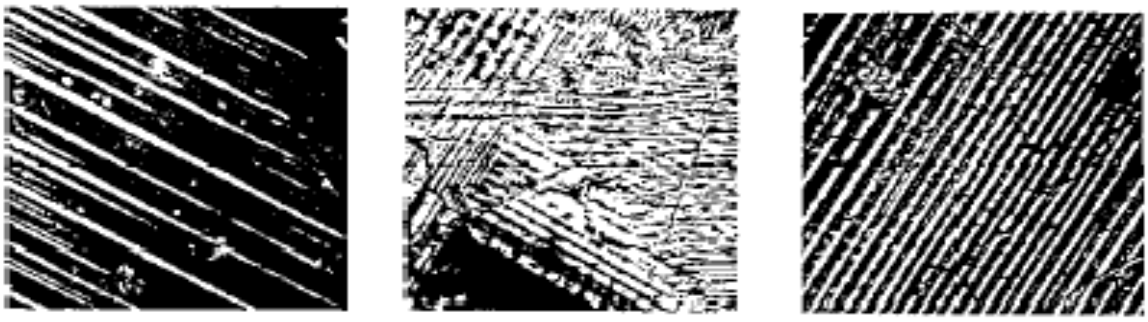

Figure 2.7: Experimentally observed microstructures of lead phosphate. [The two fully ‗switched‘ crystals (a) and (c) display striped twin patterns whereas the crystal in the intermediate state (b) shows superposition of various twin orientations.]

2.3 Order parameter couplings

There are four order parameters. The order parameter couplings are given below:

- **Piezoelectricity:** describes a change in strain as a linear function of applied electric field, or a change in polarization as a linear function of applied stress.

- **Piezomagnetism:** describes a change in strain as a linear function of applied magnetic field, or a change in magnetization as a linear function of applied stress.

- **Magnetoelectricity:** describes the influence of a magnetic (electric) field on the polarization (magnetization) of a material.

- **Electrostriction:** describes a change in strain as a quadratic function of applied electric field.

The effects of cross-coupling between ferroic orders is, represented in figure 2.8. Changes in strain as a function of an electric or magnetic field are shown by the black arrows, and the magnetoelectric coupling between the ferroelectric and ferromagnetic orders is shown by the green arrows.

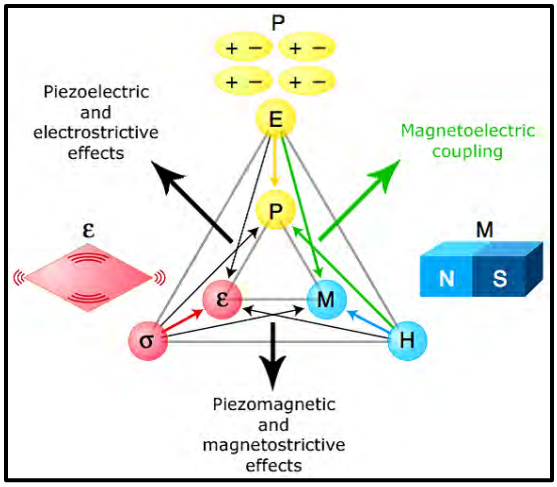

Figure 2.8: Ferroic orders and possible couplings between them.

2.4 Multiferroics and magnetoelectric effect

Multiferroic materials are single-component materials or composites exhibiting two or more ferroic properties such as ferromagnetism, ferroelectricity, or ferroelasticity, as shown in Figure 2.9. In a broader definition, it also covers materials with ferro- and antiferro- orders. There are significant scientific and technological interests in these materials due to their unusual responses, including very large magneto-electric susceptibility, giant magnetostriction, and energy coupling coefficients. In addition, the ability to couple between the spontaneous order parameters offers extra degrees of freedom in the design of conventional devices. Examples of single component multiferroics are $BiFeO_3$ (a ferromagnetic/ferroelectric perovskite), and Fe-Ga (a ferromagnetic/ferroelastic alloy). However, magnetoelectic multiferroics are materials that combine ferromagnetic and ferroelectric order parameters. **Due to the scope of this thesis and their huge application field, current discussion will mainly focus on magnetoelectric multiferroics.**

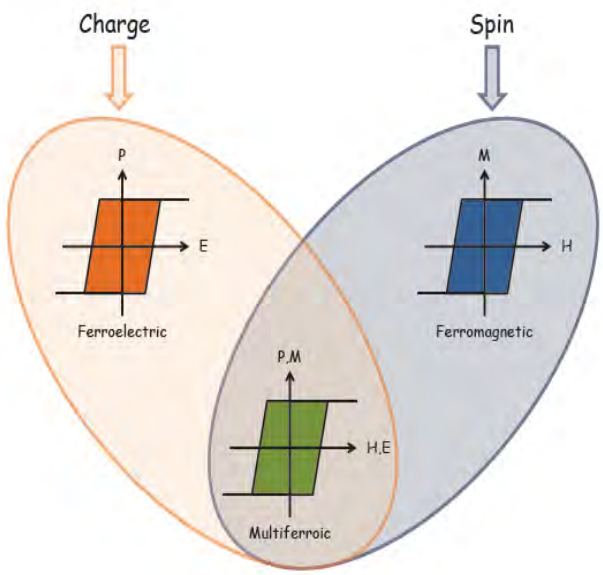

Figure 2.9: Magnetoelectric Multiferroics. [Multiferroics materials are those that present more than one ferroic order. Multiferroics combining ferroelectric (left-orange) and ferromagnetic (right- blue) properties are very appealing materials because the possible presence of magnetoelectric coupling (magnetic control of polarization or electric control of magnetization, bottom-green) can give rise to new technological functionalities.]

The ability to combine magnetic and ferroelectic properties within one material and the potential functionality that can be achieved has resulted in much of the early work on multiferroics being concentrated within magnetoelectric multiferroics [38]. Combining these two properties has, however, proven to be difficult. Normally, these two order parameters are mutually exclusive; yet a number of materials have simultaneously presented magnetic and ferroelectric properties. Coupling of the parameters within the multiferroic system tends to be weak. The microscopic mechanisms of magnetism and ferroelectricity are very different from each other therefore do not strongly interfere.

2.4.1 Classification of multiferroics

The microscopic origin of magnetism is basically the same in all magnets: it is the presence of localized electrons, mostly in the partially filled d or f shells of transition-metal or rare-earth ions, which have a corresponding localized spin, or magnetic moment. Exchange interactions between the localized moments lead to magnetic order. The situation with ferroelectrics is quite different. There are several different microscopic sources of ferroelectricity, and accordingly one can have different types of multiferroics. Broadly, multiferroics can be classified as single-phase or composite multiferroics.

2.4.1.1 Single phase multiferroics

Single-phase multiferroics are those materials that show both ferroelectric and ferromagnetic order [38-44] in a single phase .Thus multiferroicity is intrinsic of the material. In opposition to single-phase multiferroics, multiferroic order is not intrinsic in multiphase mulriferroics but results from the combination of two materials that are ferroelectric and ferromagnetic, separately. Therefore, the availability of ferromagnetic and ferroelectric materials at room temperature makes easy to obtain multiferroic composite materials at room temperature.

Single-phase multiferroics can be further classified into two groups. The first group, called type-I multiferroics, contains those materials in which ferroelectricity and magnetism have different sources and appear largely independent of one another, though there is some coupling between

them. In these materials, ferroelectricity typically appears at higher temperatures than magnetism, and the spontaneous polarization P is often rather large (of order 10 -100 μC/cm²). Examples are $BiFeO_3$ (T_{FE} ~ 1100K, T_N = 643 K, P ~90μC/cm²) and $YMnO_3$ (T_{FE} ~914K, T_N= 76 K, P ~ 6μC/cm²). The second group, which we can call type-II multiferroics, is the relatively recently discovered materials [45, 46], in which magnetism causes ferroelectricity, implying a strong coupling between the two. However, the polarization in these materials is usually much smaller (10^{-2}μC/cm^2).

- **Type-I multiferroics**

Type-I multiferroics are ―older" and more numerous. These are often good ferroelectrics, and the critical temperatures of the magnetic and ferroelectric transitions can be well above room temperature. Unfortunately, the coupling between magnetism and ferroelectricity in these materials is usually weak compare to type-II multiferroics. The materials challenge for this group of multiferroics is to keep all their positive features, but enhance this coupling. The source of magnetism in these materials is the presence of localized electrons, mostly in the partially filled d or f shells of transition-metal or rare-earth ions, which have a corresponding localized spin, or magnetic moment. However, one can single out several different subclasses of type-I multiferroics, depending on the mechanism of ferroelectricity in them. We will focus on four of the major mechanism of ferroelectricity in these materials.

Ferroelectricity due to lone pairs

In $BiFeO_3$, and probably in $BiMnO_3$ and $PbVO_3$, Bi^{3+} and Pb^{2+} play the major role in the origin of ferroelectricity. In these ions, there are two outer 6s electrons that do not participate in chemical bonds. They are called lone pairs, or sometimes dangling bonds. They have a high polarizability—the condition required for ferroelectricity in the classical description. These electrons generate an electric dipole, which is the origin of ferroelectric order. Other cations (i.e. Fe^{3+}, Mn^{3+}, Ni^{2+}) are responsible for magnetic properties. More microscopically one can explain the origin of ferroelectricity in these compounds by ordering of these lone pairs (with certain admixture of p orbitals) in one direction (Figure 2.10). Apparently this is what happens in many

Bi- and Pb-containing ferroelectrics and multiferroics such as $BiFeO_3$, but it also helps to improve the ferroelectric properties of $Pb[Zr_xTi_{(1-x)}]O_3$.

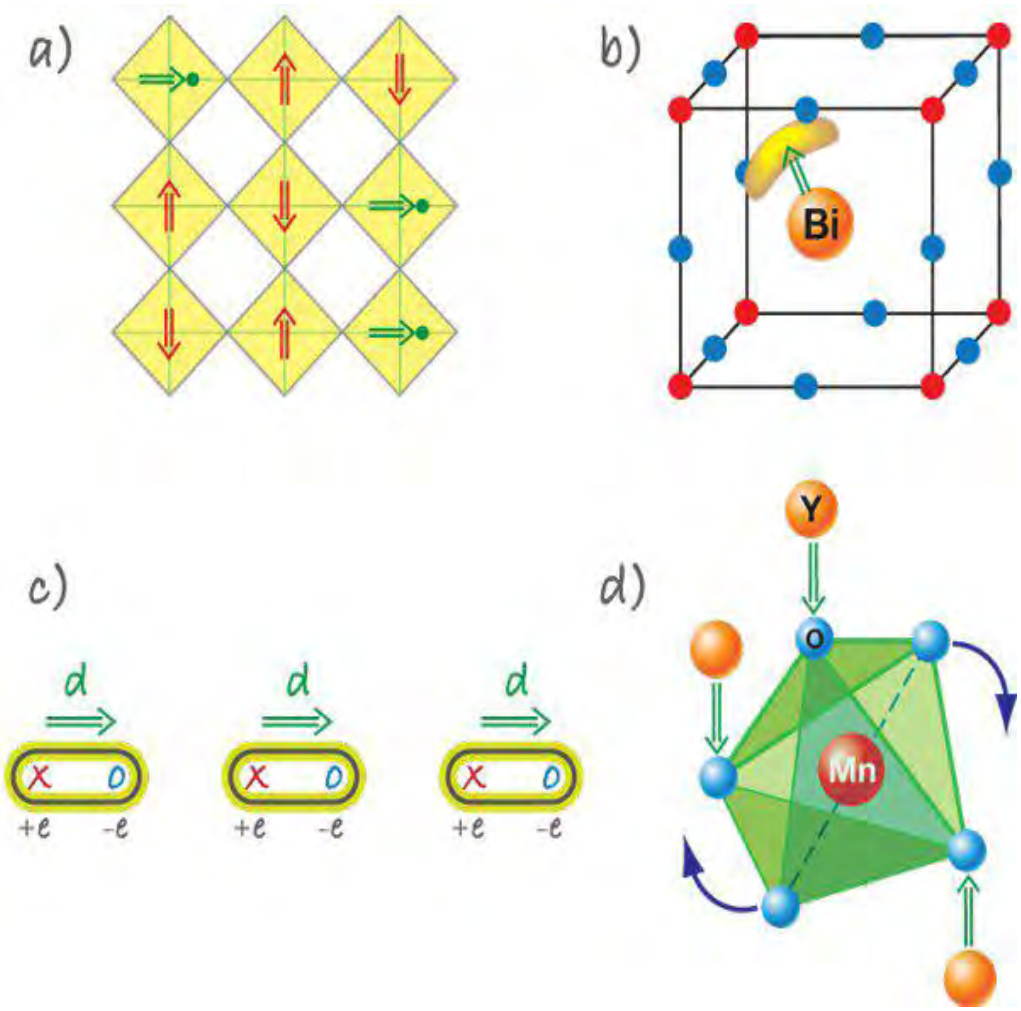

Figure 2.10: Different microscopic mechanisms found in type-I multiferroics. [(a) In ―mixed" perovskites with ferroelectrically active d0 ions (green circles) and magnetic d^6 ions (red), shifts of d0 ions from the centers of O_6 octahedra (yellow plaquettes) lead to polarization (green arrows), coexisting with magnetic order (red arrows). (b) In materials like $BiFeO_3$ and $PbVO_3$, the ordering of lone pairs (yellow "lobes") of Bi^{3+} and Pb^{2+} ions (orange), contributes to the polarization (green arrow). (c) In charge ordered systems, the coexistence of inequivalent sites with different charges, and inequivalent (long and short) bonds, leads to ferroelectricity. (d) The ―geometric" mechanism of generation of polarization in $YMnO_3$ describes the tilting of a rigid MnO_5 block with a magnetic Mn remaining at the center. Because of the tilting, the Y-O bonds form dipoles (green arrows), and there appears two"up" dipoles per one ―down" dipole so that the system becomes ferroelectric (and multiferroic when Mn spins order at lower temperatures).]

Ferroelectricity due to charge ordering

One more mechanism that can lead to ferroelectricity and to type-I multiferroicity can be charge ordering, often observed in transition metal compounds, especially those formally containing transition metal ions with different valence. If, after charge ordering, both sites and bonds turn out to be inequivalent, this can lead to ferroelectricity [Figure 2.10]. A corresponding mechanism can work in systems like $Pr_{1/2}Ca_{1/22}MnO_3$ or in nickelates $RNiO_3$ with charge ordering. But more often we meet the situation in which there exist ions with different charge (often because they are different elements), but on top of that there occurs dimerization.

$TbMn_2O_5$ belongs to this class, as does the newly discovered multiferroic Ca_3CoMnO_6. Another similar possibility is when the bonds are in equivalent because of the structure of the material, the site-centered charge order appearing on top of that. This is the case in an organic ferroelectric $(TMTTF)_2X$, and also in the multiferroic $LuFe_2O_4$

Ferroelectricity in Perovskite Structure

Probably the best-known ferroelectrics are the perovskites like $BaTiO_3$ or $Pb(ZrTi)O_3$ (PZT). There are many magnetic materials among perovskites, and also many ferroelectrics [47]. But comparing these extensive compilations, each containing more than 100 pages of tables, demonstrates that there seems to be mutual exclusion of magnetism and ferroelectricity in perovskites: there is practically no overlap of these tables. Whereas for magnetism one needs partially filled d shells of a transition metal, practically all ferroelectric perovskites contain transition metal ions with an empty d shell, such as Ti^{4+}, Ta^{5+}, W^{6+}. Ferroelectricity in these systems is caused by the off-center shifts of the transition metal ion, which forms strong covalent bonds with one (or three) oxygens, using their empty d states. And somehow, the presence of real d electrons in d^n configurations of magnetic transition metals suppresses this process, preventing ferroelectricity in magnetic Perovskites. This so called ―d^0 vs d^n problem" was one of the first to be studied theoretically at the beginning of the recent revival of multiferroics [48], and although there has been some progress, still there is no full solution of this problem [45]. The answer may well lie in the fact that this mutual exclusion is not a ―theorem" but rather a

matter of numbers: in most cases a magnetic d^n ion is stable in the center of its O_6 octahedra, but there may still be the cases where it is not. One possible way around this problem may be making ―mixed" perovskites with d^0 and d^n ions (Figure 2.10). However, the coupling of magnetic and ferroelectric subsystems in mixed perovskites is weak.

"Geometric" ferroelectricity

Lastly, we consider a case realized in, for example, $YMnO_3$ [49]. Ferroelectricity in $YMnO_3$ has nothing to do with the magnetic Mn^{3+}, but is caused by the tilting of the practically rigid MnO_5 block. This tilting occurs just to provide closer packing, and as a result the oxygen ions move closer to the rather small Y ions (Figure 2.10).

- **Type-II multiferroics: Magnetic multiferroics**

The biggest excitement nowadays is caused by the discovery of a novel class of multiferroics in which ferroelectricity exists only in a magnetically ordered state and is caused by a particular type of magnetism. For example, in $TbMnO_3$ magnetic ordering appears at T_{N1} = 41 K, and at a lower temperature, T_{N2} = 28 K, the magnetic structure changes. It is only in the low temperature phase that a nonzero electric polarization appears. Similar behavior occurs in $TbMn_2O_5$. The first paper to study $TbMnO_3$ showed that a magnetic field can strongly influence the electric polarization: e.g. in $TbMnO_3$ the polarization rotates (or ―flops") by 90 degrees when a critical magnetic field is applied along a certain direction [50]. In $TbMn_2O_5$ the influence of an external field is even stronger: the polarization changes sign with field, and a field alternating between +1.5 and -1.5 Tesla leads to corresponding oscillations in the polarization [51]. Since the discovery of these materials, a number of other type-II multiferroics with strong magnetoelectric coupling have been discovered. However, these materials have been recently discovered and are under vigorous study.

From the point of view of the mechanism of multiferroic behavior, one can divide type-II multiferroics into two groups: those in which ferroelectricity is caused by a particular type of magnetic spiral and those in which ferroelectricity appears even for collinear magnetic structures.

Spiral magnets

Spiral magnets are those where atomic spin rotate across the lattice in a defined plane, this breaks the symmetry and allows ferroelectricity. However, ferroelectricity only takes place in spiral magnets when the so-called cycloidal spin arrangement set, that is spins rotate in the plane of the propagation of the spiral. In this case, ferroelectricity arises in the plane of the cycloid and perpendicular to the propagation vector of the cycloid due to the so-called inverse Dzyaloshinsky-Moriya interaction ($P = A \sum rij \times (S_i \times S_j)$, being r_{ij} the vector connecting the S_i and S_j spins). Here, sizable spin-orbit interaction is needed (A), if A is large the magnetoelectric coupling is strong. The cycloid is sensible to the application of a magnetic field, which can produce rotation of cycloid plane by 90 (so-called flopping), inducing a change in the direction of o the ferroelectric polarization. $TbMnO_3$ is the archetype of this class of 3 multiferroic materials [52].

Collinear magnets

In these materials one-dimensional chains of up-up- down-down spins are formed due to the exchange striction. The distortion induced by up-up (down-down) or up-down (down-up) bonds is different, which provokes the formation of ordered electric dipoles. An example is Ca_3CoMnO_6 [53], or E-type rare earth manganites, e.i. $HoMnO_3$ [49, 54].

2.4.1.2 Multiphase multiferroics

The choice of single-phase materials exhibiting the coexistence of at least two ferroic orders at room temperature is quite limited. The scarcity of single phase multiferroic materials makes composite/ multiphase multiferroics an interesting alternative. Magnetoelectric multiferroic composites consist of a ferroelectric phase and ferromagnetic phase, and the coupling between the two orderings is through stress mediation. The magnetoelectric effect is extrinsic in this case since magnetoelectric effect is not exhibited by any of the constituent phases on their own. Various constituent materials have been studied as multiferroic composite materials, such as

$BaTiO_3$-$CoFe_2O_4$, $BaTiO_3$-$NiFe_2O_4$, PZT-$NiFe_2O_4$, PZT-$CoFe_2O_4$, $BiFeO_3$-$CoFe_2O_4$, and $BiFeO_3$-$NiFe_2O_4$.

2.4.2 Why is it difficult to find materials that are both ferroelectric and magnetic in a single phase?

Multiferroics that possess two ferroic (ferroelectric and magnetic) orderings in single phase are very rare in nature due to their requirement of coexistence of transition metal ions with odd number of d electrons for magnetism and lone pair active ions for ferroelectric property in the same compound [6,48].

Most ferroelectrics are transition metal oxides, in which transition ions have empty d shells. These positively charged ions like to form _molecules‘ with one (or several) of the neighbouring negative oxygen ions. This shift of the cation inside a periodic crystal induces bulk electric polarization. The mechanism of the covalent bonding (electronic pairing) in such molecules is the virtual hopping of electrons from the filled oxygen shell to the empty *d* shell of a transition metal ion. Magnetism, on the contrary, requires transition metal ions with partially filled d shells, as the spins of electrons occupying completely filled shells add to zero and do not participate in magnetic ordering. The exchange interaction between uncompensated spins of different ions, giving rise to long range magnetic ordering, also results from the virtual hopping of electrons between the ions. In this respect the two mechanisms are not so dissimilar, but the difference in filling of the *d* shells required for ferroelectricity and magnetism makes these two ordered states mutually exclusive.

Still, some compounds, such as $BiMnO_3$ or $BiFeO_3$ with magnetic Mn^{3+} and Fe^{3+} ions having partially filled d shell, are ferroelectric. Here, however, it is the Bi ion with two electrons on the 6*s* orbital (lone pair) that moves away from the centrosymmetric position in its oxygen surrounding. These materials are rare in nature. Because the ferroelectric and magnetic orders in these materials are associated with different ions, the coupling between them is weak. For example, $BiMnO_3$ shows a ferroelectric transition at $T_{FE} \approx 800$ K and a ferromagnetic transition at $T_{FM} \approx 110$ K, below which the two orders coexist. $BiMnO_3$ is a unique material, in which both

magnetization and electric polarization are reasonably large. This, however, does not make it a useful multiferroic. Its dielectric constant ε shows only a minute anomaly at T_{FM} and is fairly insensitive to magnetic fields: even very close to T_{FM}, the change in ε produced by a 9-Tesla field does not exceed 0.6%.

Nevertheless, multiferroism involves a number of subtle competing factors for it‘s ferroelectricc property, with d-electron occupancy on the transition metal being a critical issue for the ferromagnetic property.

2.5 $BiFeO_3$ multiferroics

Bismuth ferrite (BFO) is one of the most interesting members of multiferroic family which shows both ferroelectric and ferromagnetic properties in a single phase at room temperature. It is one of the few multiferroics that has Curie and Neel temperatures far above room temperature. It shows magnetoelectric coupling at room temperature and such coupling is strongly enhanced by proper dopings.

2.5.1 History of $BiFeO_3$

The basic idea that crystals could be simultaneously ferromagnetic and ferroelectric probably originated with Pierre Curie in the 19th century. After switching was discovered in ferroelectric Rochelle Salt by Valasek in 1920 [23] there was a rash of supposed discoveries of magnetoelectric properties by Perrier, but unfortunately in materials such as Ni in which they are now understood to be impossible. A history of this period of solid-state physics is given in O‘ Dell‘s text [55].

True magnetoelectricity –defined as a linear term in the free energy was first understood theoretically by Dzyaloshinskii with special predictions being made for Cr_2O_3 and discovered experimentally in that material by Astrov. However this material is paraelectric and antiferromagnetic, making microelectronics applications impractical.

The more interesting case of ferromagnetic ferroelectrics waited for some years until the work of Schmid on boracites [56]. The boracites are also impractical materials for device applications: they have low symmetry with large unit cells and grow in needle shapes; more importantly, they exhibit magnetoelectricity only at extremely low temperatures. Meanwhile Smolenskii‘s group in Leningrad pioneered the study of bismuth ferrite, $BiFeO_3$, but they found that they could not grow single crystals and that ceramic specimens were too highly conducting (probably caused by oxygen vacancies and mixed Fe valences) to be used in applications. They tried to address the conductivity problem by doping other ions into both the A and B sites of the lattice.

Reviews of the general study of magnetoelectricity appeared by Schmid in 1994 [57] and more recently by Fiebig [57] and by Eerenstein et al. [59]. The current interest in bismuth ferrite was stimulated primarily by works of Ramesh‘s group in 2003 [24]. Increasing efforts have now been devoted to the research focusing on the preparation and characterization of $BiFeO_3$ in forms of film, bulk and nanostructure.

2.5.2 Science of $BiFeO_3$

In parallel with the specific investigation of bismuth ferrite and related compounds has been a more general approach to the idea of multiferroics. NicolaHill (now Spaldin) has asked [1] why there are so few materials that are magnetic and ferroelectric; implicitly limiting her discussion to transition-metal oxides, especially perovskites, she observed that the ferroelectrics (e.g., titanates) have B-site ions with d^0 electrons [60], whereas the magnets require d^j electrons with j different from zero.

However, oxide perovskites do not all have the same mechanism of ferroelectricity: the center Ti ion plays the key role in $BaTiO_3$ [61] but the lone-pair Pb ion is dominant in $PbTiO_3$ [62]. Indeed, this seems to be the case in $BiFeO_3$, where the polarization is mostly caused by the lone pair (s2 orbital) of Bi^{3+}, so that the polarization comes mostly from the A site while the magnetization comes from the B site (Fe^{3+}) having d^j configuration; this same idea has led Spaldin and co-workers to propose a host of other perovskites with possible A-site ferroelectricity and B-site magnetism, such as $Bi(Cr,Fe)O_3$ and $BiMnO_3$.

2.5.2.1 Structure of $BiFeO_3$

The room-temperature phase of $BiFeO_3$ is classed as rhombohedral perovskite (point group R3c) [23]. The primitive unit cell contains two formula units of perovskite. In the perovskite structure each A-site atom is surrounded by 12 nearest neighbour oxygen ions and each B-site atom has six oxygen ion neighbours. Together the A-site atom and O_2- ions forms FCC arrangement with B-site atom fitting into the octahedral interstices. The perovskite-type unit cell has a lattice parameter, a_{rh}, of 3.965A° and a rhombohedral angle, α_{rh}, of 89.3–89° at room temperature [23, 62] with ferroelectric polarization along $[111]_{pseudocubic}$ [23]. The unit cell can also be described in a hexagonal frame of reference, with the hexagonal c-axis parallel to the diagonals of the perovskite cube. The hexagonal lattice parameters are a_{hex} = 5.58A ° and c_{hex} = 13.90A °.

A very important structural parameter is the rotation angle of the oxygen octahedra. This angle would be 0° for a cubic perovskite with perfectly matched ionic sizes. A measure of how well the ions fit into a perovskite unit cell is the ratio $(r_{Bi} + r_O)/l$, where r is the ionic radius of the respective ion and l is the length of the octahedral edge. This is completely analogous to the commonly used Goldschmid tolerance factor, [23, 62] which is defined as $t = (r_{Bi} + r_O)/(r_{Fe} + r_O)$. For $BiFeO_3$ we obtain t=0.88 using the ionic radii of Shannon, [63] with Bi^{+3} in eightfold coordination (the value for 12-fold coordination is not reported) and Fe^{+3} in sixfold coordination and high spin. When this ratio is smaller than one, the oxygen octahedra must buckle in order to fit into a cell that is too small. For $BiFeO_3$, ω is ca. 11–14° around the polar [111] axis [62, 63].

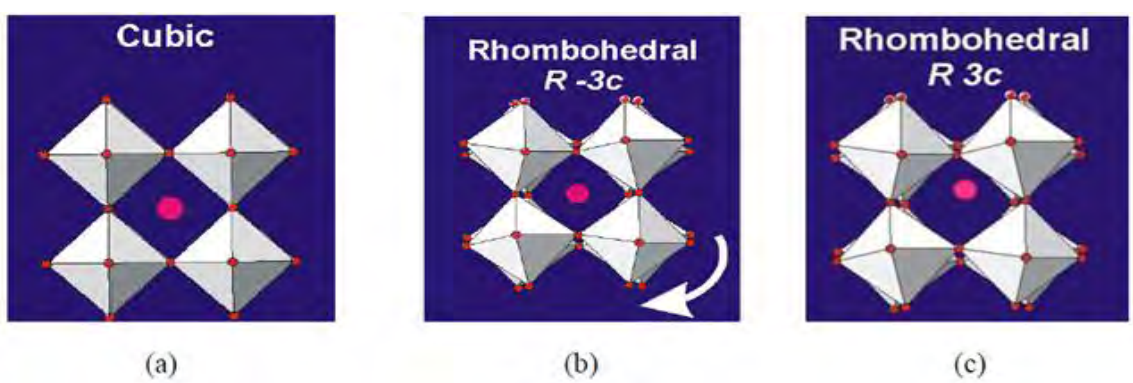

Figure 2.11: Schematic illustration of a structural transition process.[(a) ideal cubic structure Pm-3m without tilting; (b) R-3c structure tilted along three axes with the same angle; (c) Displacement of Bi ion towards [111] direction based on R-3c.]

The lattice parameter and crystal structure of $BiFeO_3$ are dependent on the temperature. It was well documented that, except for the long Bi-Fe bond distance, the lattice parameter a, c, the volume of unit cell, the short bond distance of Bi-Fe as well as the bond angles gradually increase with increase in temperature. As a consequence of these variations, magnetism and polarization are reported to be gradually reduced, and structural phase transitions are also induced from the rhombohedrally distorted R3c perovskite structure to an orthorhombic Pnma structure and eventually to a cubic structure.

2.5.2.2 Phase diagram of $BiFeO_3$

The phase diagram of Fe_2O_3 and Bi_2O_3 is presented below in Figure 2.12, unequal amount of Fe_2O_3 and Bi_2O_3 is seen to bring about impurity phases $Bi_{25}FeO_{39}$ (bismuth-rich) and Bi_2FeO_9 (bismuth-deficient). $BiFeO_3$ is usually prepared from equal parts of Bi_2O_3 and Fe_2O_3, and under high temperatures it can decompose back into these starting materials, as shown in Equation 2.1.

$$2BiFeO_3 \longrightarrow Fe_2O_3 + Bi_2O_3 \quad (2.1)$$

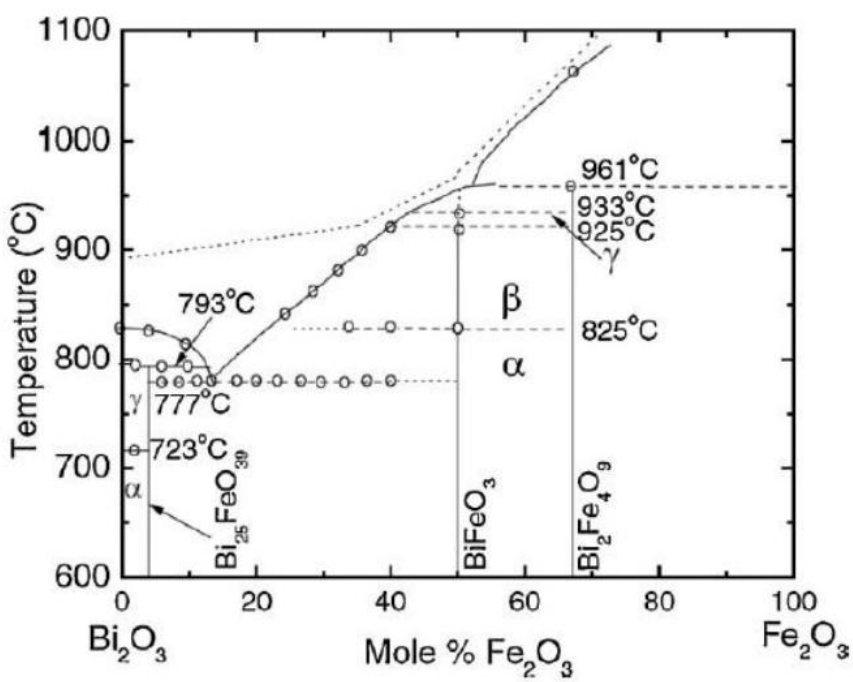

Figure 2.12: Phase Diagram of Fe_2O_3 and Bi_2O_3.

At approximately 825°C there is a first-order transition to a high-temperature β phase that is accompanied by a sudden volume contraction [23, 64, 65]. The transition is also accompanied by a peak in the dielectric constant [65]; this has been taken as an indication of a ferroelectric–paraelectric transition, although dielectric peaks can also occur in ferroelectric–ferroelectric transitions, such as the orthorhombic–rhombohedral transition in the archetypal perovskite ferroelectric $BaTiO_3$ (which is also first order). Nevertheless, although there is disagreement about the exact symmetry of the β phase above 825°C, most reports agree that it is centrosymmetric [67–69], so it is probably a safe bet that the α–β transition at T_C = 825°C is indeed the ferroelectric–paraelectric transition.

Palai et al. [64] propose that the symmetry of the β phase is orthorhombic, although their data does not allow establishing the exact space group with certainty. Some authors have argued that the β phase may be tetragonal or pseudotetragonal [64, 66, 67], but that is impossible, since the domain structure rules out a tetragonal symmetry and the perovskite a,b,c lattice constants are each quite different [64, 68]. It was also proposed that this phase may instead be monoclinic [67, 68]; the measured monoclinic angle was nevertheless initially quoted as 90° within experimental error, so that the β phase was in effect __metrically orthorhombic‘‘ (i.e., the angles may be 90°, but internal ion positions in each unit cell do not satisfy orthorhombic constraints). More recently, however, Haumont et al. have quoted a monoclinic angle of 90.01^{o} [68].

2.5.3 Electrical properties of $BiFeO_3$

The ferroelectric state arises from a large displacement of the Bi ions (A-site polarization) relative to the FeO_6 octahedra in $BiFeO_3$ as shown in Figure 2.13. The ferroelectric polarization lies along the pseudocubic <111> leading to the formation of eight possible polarization variantsts.

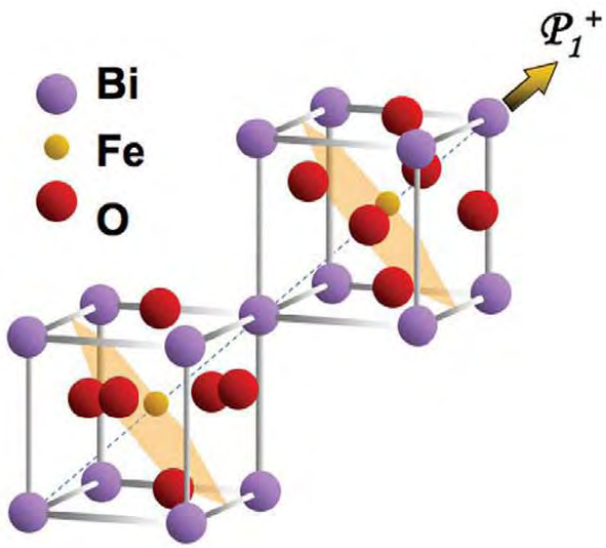

Figure 2.13: Schematic of crystal structure of BFO and ferroelectric polarization (arrow).

Whether A-site and B-site polarization occurs depends on Goldschmid Tolerance Factor,

$$t = (r_{A\text{-site}}+r_O)/\sqrt{2}(r_{B\text{-site}}+r_O); \qquad (2.2)$$

If t<1 the oxygen octahedra must buckle in order to fit into a cell that is too small.

For, $BaTiO_3$, t=(1.5+1.28)/√2(0.75+1.28)=.98~1; **Slight or no buckle** (B-site polarization)
For, $BiFeO_3$, t=(1.17+1.28)/√2(0.69+1.28)=.88 ; **Buckling Occurs** (A-site polarization)

This buckling of FeO_6 octahedra in $BiFeO_3$ is the main cause behind A-site polarization. The displacement of the A-site bismuth cation (shown in Figure 2.11) along the [111] axis due to octahedra buckling brings about a non-centrosymmetric polarization resulting in the ferroelectric property.

Electrical characterization on bulk $BiFeO_3$ has been very difficult due to the low resistivity of samples. The controversy about whether it is ferroelectric or antiferroelectric was finally settled based on the hysteresis loop measured by Teague et al. [70]. They performed the experiment in liquid nitrogen, which lowered the charge carrier density and mobility, and in turn lowered the leakage current. The measured spontaneous polarization was 3.5μC/cm^2 along the <100> direction, which represents 6.1μC/cm^2 in the <111>direction. This value is much smaller than

what would be expected for a ferroelectric material with such high Curie temperature and large distortion. The leakage problem, likely due to defects and non-stoichiometry, has been hampering more comprehensive studies about the bulk $BiFeO_3$ and has limited applications of this material. To overcome this problem, several works has been reported to reduce leakage current of $BiFeO_3$ using proper dopants.

2.5.3.1 Dielectric constant of $BiFeO_3$

The radio frequency dielectric constant of $BiFeO_3$ at room temperature is $\varepsilon_r = 30$. [23]. It peaks at the rhombohedral–orthorhombic transition (825–840°C), possibly – though not necessarily – due to a ferroelectric–paraelectric transition. This dielectric constant is small compared with those of typical perovskite ferroelectrics such as $BaTiO_3$, (Ba, Sr)TiO_3 and Pb(Zr,Ti)O_3 (PZT). The mean refractive index, n, of $BiFeO_3$ is [23] approximately 2.62, so the optical frequency dielectric constant can be estimated as $\varepsilon_r = 6.86$. This is only an average value, however; dielectric constant at optical frequencies is very anisotropic.

Although 30 can be regarded as the intrinsic dielectric constant of this compound at radiofrequencies, the impedance measurements in parallel-plate capacitors often yield higher values: between 50 and 300 depending on sample morphology, orientation, and frequency range. This is because at the frequencies typically accessible by impedance analyzers (100 Hz to 1 MHz), domain-wall motion and space-charge contributions can be important and add to the measured permittivity. While the intrinsic value $\varepsilon_r = 30$ may seem small for a ferroelectric, this value is not unreasonable. For one thing, the ferroelectric Curie temperature of $BiFeO_3$ is very high, meaning that at room temperature the ferroelectric polarization is already saturated and, thus, small electric fields will barely affect it (the dielectric constant is essentially a measure of polarizability).

Finally, and this is just a hypothesis, it may be that perovskite ferroelectrics in which the polarization comes from the A site (e.g., $PbTiO_3$ and $BiFeO_3$) have intrinsically lower dielectric constants than those where polarization comes from the B site (e.g., $BaTiO_3$). Experimentally

this certainly seems to be the case, but at present we know of no satisfactory explanation for this fact, if indeed it is more than just a coincidence.

2.5.4 Magnetic properties of $BiFeO_3$

The local short range magnetic ordering of BFO is G-type antiferromanget: each Fe^{3+} spin is surround by six nearly antiparallel spins on the nearest Fe neighbours (Figure 2.14). The antiferromagnetic spin ordering is not homogeneous but is manifested as an incommensurated cycloid structure with a wavelength of ~ 64 nm along <110>, as can be seen in Figure 2.15 [23]. In this cycloid structure the net magnetic moment of the spins cancel out each other and results in zero net magnetization. The spin rotation plane can also be determined because the magnetic scattering amplitude depends on the component of magnetic moments perpendicular to the scattering vector . The magnetic Néel temperature is about 643 K and the cycloid could be distorted at low temperatures [71].

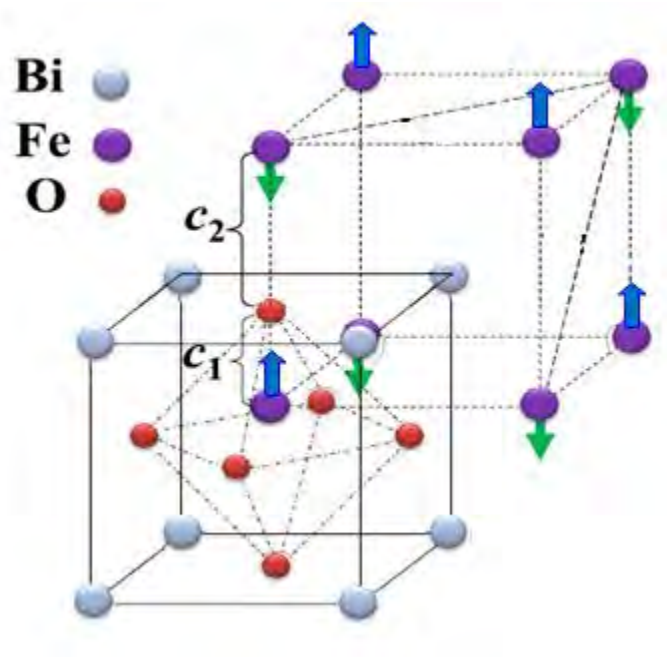

Figure 2.14: (Colour on-line) Schematic of tetragonal-like $BiFeO_3$ (BFO) with G-type antiferromagnetic ordering.

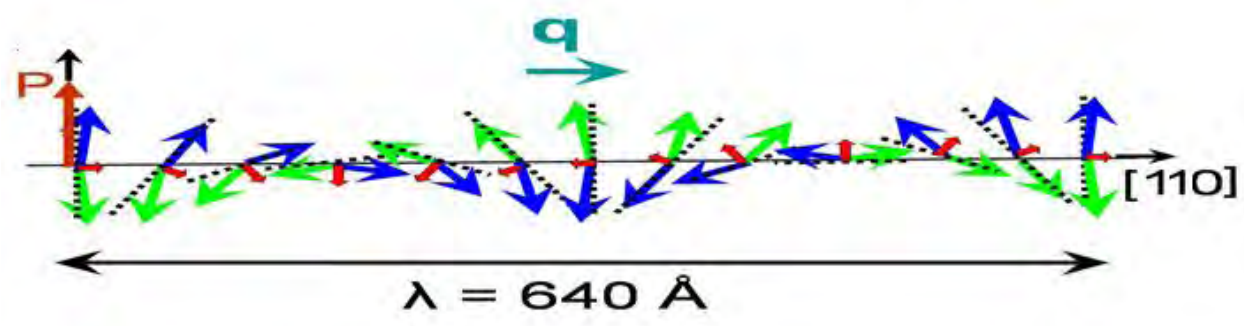

Figure 2.15: Schematics of the 64 nm antiferromagnetic circular cycloid. [The canted antiferromagnetic spins (blue and green arrows) give rise to a net magnetic moment (purple arrows) that is specially averaged out to zero due to the cycloidal rotation. The spins are contained within the plane defined by the polarization vector [23].]

Sc, Mn, Nb, Zr, Co and Ti ions substitute of Fe ions would increase the magnetization by changing the Fe valence state due to charge compensation and varying the Fe-O-Fe bond angle to increase the spin [13, 17, 73, 74]. For Bi-site substitution, Yb, La, Gd, Nd, Pb, Ca, Sr ions may also impact the magnetization of the BFO stem from the spatial homogenization of spin arrangement. A-site substitution with ions having different ionic radius than Bi^{3+} changes cycloidal spin structure of pure $BiFeO_3$ to a canted spin structure which would also result in enhancement in ferromagnetic properties in doped materials. The disturbed spin cycloid structure when Ba ions positions in Bi-site, the formation of partial Fe^{2+} due to the Bi ions volatilization or oxygen vacancies, varied canting angle of Fe-O-Fe bond due the distortion of FeO_6 octahedron are caused by introducing Ba ions. The increased tensile strain changes the balance between the antiferromagnetic and ferromagnetic interactions [6, 12, 29, 74, 75]. As for the impact for dopants on the magnetic phase transition, there are very few report studies.

2.4.5 Processing of bismuth ferrite based ceramics

In case of ceramic bodies, properties of the final parts largely depend on the processing route. In the present days bismuth ferrite powders are being processed through many routes. Of them, most modern sol-gel precipitation route, chemical precipitation, hydrothermal and combustion reaction are prominent to obtain ultra-pure powders. Choices of route depend on the applications. But till now the conventional route is the most popular method from the industrial point of view. The conventional solid state synthesis route, also known as the ceramic method,

refers to a procedure of heating two or more non-volatile solid state materials that can react with one another forming a new compound.

Typically, the high temperature treatment (500°C-2000°C) is required during the process, which provides the energy condition that enables the ions to leave their original sites and diffuse to different sites. The solid state reaction is quite slow but the reaction can speed up considerably if the temperature is increased. However, due to the decomposition or melting of materials, extremely high temperature is not favored. In principal, the optimal temperature is defined by a rule of thumb that two-thirds of the melting temperature of the compound always gives best reaction time

2.4.5.1 Ball Milling

Before ball milling the raw materials like Bi_2O_3 and Fe_2O_3 powders are weighed according to the stoichiometry. The weighed powders are thoroughly mixed in a ball mill or in an attrition mill. Milling is carried out to fulfil twofold purposes. One is to reduce the particle size and another is to mix the raw materials homogenously. Both finer particle and homogeneity of raw powders eases the diffusion controlled solid state reactions.

The schematic representation of a ball mill is illustrated in Figure 2.16. In the present days, powders are only mixed properly in a laboratory type pot mill. Size reduction of the powders are not now the primary objective of ball milling as the nano sized powders are now available for laboratory type research, rather the objective of ball milling is to homogenize the mixture. The balls should be of the same material as powders so that wear of balls does not contaminate the powder mix. For example, in the past days hardened steel balls were used in a porcelain pot. Bt iron has a very detrimental effect on the dielectric properties of barium titanate based materials. In the present days high density polyethylene (HDPE) pots are used as the container and Y_2O_3 stabilized ZrO_2 balls are used to mill the powders.

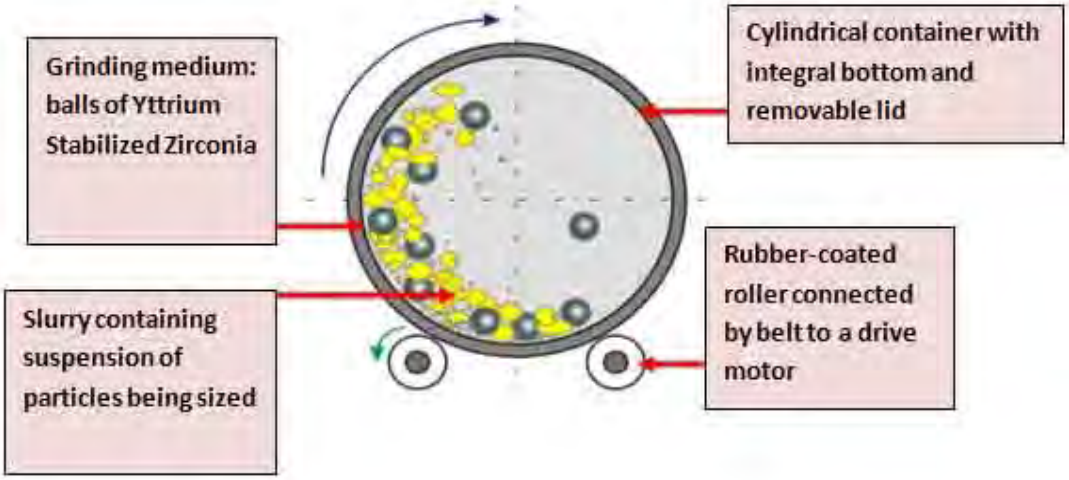

Figure 2.16: Schematic representation of ball milling.

In the wet milling process, milling medium is another important consideration for two reasons. It must not react with the balls, the container or the powder. Secondly, it must avoid decrease of colloidal stability.. After milling the suspension is dried to evaporate the milling medium.

2.4.5.2 Shaping and drying

The milled powder ready for further processing is commonly referred as _green‘ body. The green bodies should have a certain minimum density before they can be sintered. Common practice is to achieve 60% of the theoretical density during shaping and pre-sintered state.

The desired shape and a minimum green density can be provided by various techniques including powder compaction, slip-casting, extrusion, doctor blading, dipping, etc. We should go for hot pressing although it is expensive method. But the process is becoming popular for better quality ceramic material used in high end application. The choice of the method depends on the type of powder used, particle size distribution, state of agglomeration, desired shape, and thickness of the part. Hydraulic or mechanical presses are used to press powder into desired

shape at the pressure of ~100 to 300 MPa. Owing to the nature of this process, only simple and symmetric shape can be prepared. No sintering aid or liquid is added to the powder for solid phase sintering route. Hence, strength of the green powder compact is achieved through addition of a suitable binder such as PVA, glycol phthalate, etc.

After shaping, the green bodies are heated very slowly to between 400-800°C in order to remove any binder present. Initial heating rate is slow to allow the gases to come out slowly without forming cracks and blisters in the ceramic part. After the binder burnout is over, the samples are taken to a higher temperature for sintering.

2.4.5.3 Sintering

The densification of a particulate ceramic compact is technically referred to as sintering. Sintering is essentially the removal of the pores between the starting particles (accompanied by shrinkage of the component), combined with growth together and strong bonding between adjacent particles.

The following criteria must be met before sintering can occur:

1. A mechanism for material transport must be present.
2. A source of energy to activate and sustain this material transport must be present.

The primary mechanisms for transport are diffusion and viscous flow. Heat is the primary source of energy, in conjunction with energy gradients due to particle-particle contact and surface tension.

All properties of ceramic depends on the sintered body which is the direct result of the sintering parameter such as sintering temperature, hold time, atmosphere, thermal profile, etc. There are many sintering methods used but this discussion would be limited to solid phase method. Heat causes the powder particles to develop intergranular bonds by surface diffusion and other physical driving force. The typical green density of ceramic body at the

start is about 60% of theoretical density. Strength starts to develop gradually as more and more particles bond.

At about ~ 80% to 85% density the pores are still open and the ceramic has a typical –chalky" appearance. The dielectric constant is usually low and the T_c is not pronounced strongly. The pores of a ceramic are generally closed above ~90% of theoretical density. Additional heat work causes greater densification as trapped gasses diffuse out along grain boundaries. At densities below 90% of theorectical density the presence of open pores would cause the dielectric loss and undoubtedly inferior dielectric properties.

Setting of sintering temperature is not that straight forward. Low temperature sintering results in ceramic of poor density. On the other hand, too high temperature and long hold time may cause open structure with low density. Also, at high temperatures grain growth is accelerated resulting in low dielectric properties. The sintering temperature and time should be optimum for proper densification to occur without abnormal grain growth. This is usually done by trial and error method depending on various process parameters

CHAPTER 3
EXPERIMENTAL

3.1 Introduction

$Bi_{1-x}Ba_xFe_{1-y}Ti_yO$ samples were prepared by solid state reaction method in this research and their properties were measured. For advanced research, it is very important to use high purity raw materials. At the same time, it is vital to ensure that during sample preparation no impurity gets incorporated into the ceramic powders. Moreover, accurate weight calculation and measurement are also important to guarantee single phase formation. After sample preparation, sample characterization and property measurement was carried out and finally a relationship between structure and property was established. During all experiments starting from sample preparation to property measurement, all parameters should be maintained for getting good consistent results.

3.2 Raw materials and their characterization

Key materials:

a) Bismuth Oxide (Bi_2O_3) powder
Size: 300 nm
Manufacturer: INFRAMAT (USA)
Purity: 99.99%

b) Iron oxide (Fe_2O_3) powder
Size: 20-50 nm
Manufacturer: INFRAMAT (USA)
Purity: 99.99%

c) Barium Carbonate ($BaCO_3$) powder
Size: 800 nm
Manufacturer: INFRAMAT (USA)
Purity: 99.99%

d) Titanium oxide (TiO_2) powder
Size: 40 nm
Manufacturer: INFRAMAT (USA)
Purity: 99.99%

e) Binder: Polymeric (81.0% C, 13.5% H, 2.9% O, 2.6% N)

Table 3.1: Information of raw materials.

Elements/Oxides	Atomic Number	Atomic Weight	Molecular weight	Density g/cm^3
Bismuth (Bi)	81	208.98	-	9.78
Iron (Fe)	26	55.85		7.86
Barium (Ba)	56	137.34		3.51
Titanium (Ti)	22	47.87		4.51
Bismuth Oxide (Bi_2O_3)	-	-	465.96	8.90
Iron oxide (Fe_2O_3)			159.70	5.24
Barium Carbonate ($BaCO_3$)			197.34	4.29
Titanium Oxide (TiO_2)			79.88	3.78

3.3 Sample Preparation

At first, constituent powders were mixed at proper amount depending on the doping level. Next, the mixture was ball milled at 120 rpm in acetone**.** After that, binder was added into the dried powder mixture. Finally, the mixture was pressed into pellets using a pressing unit.

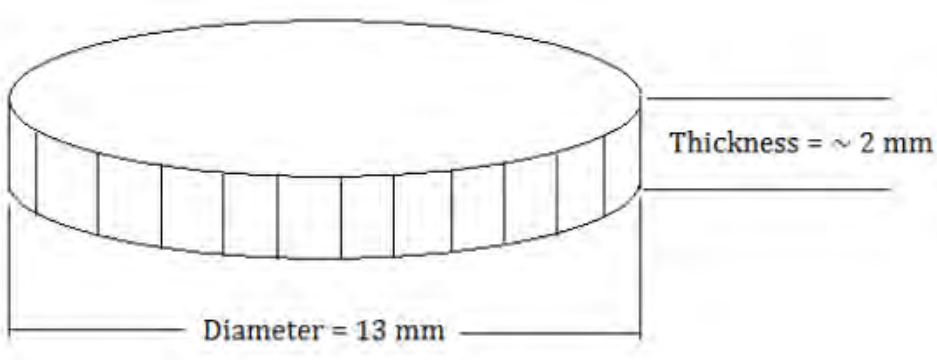

Figure 3.1: Disk shape sample.

3.3.1 Weight measurement

The basic raw materials used in this thesis are Bi_2O_3, Fe_2O_3, $BaCO_3$ and TiO_2 powders. These powders were taken at proper amount depending on the percentage of the doped element. Four compositions were prepared: a) $Bi_{0.9}Ba_{0.1}FeO_3$ b) $Bi_{0.8}Ba_{0.2}FeO_3$ c) $Bi_{0.7}Ba_{0.3}FeO_3$ and d) $Bi_{0.7}Ba_{0.3}Fe_{0.9}Ti_{0.1}O_3$. Depending upon the percentage of the doped element the amount of raw materials for mixing was varied.

Table 3.2: Raw powder requirements for formulation of samples.

Samples	Powder	Weight of powder in batch (g)	Total weight of batch (g)
$Bi_{0.9}Ba_{0.1}FeO_3$	Bi_2O_3	13.72	20
	Fe_2O_3	5.22	
	$BaCO_3$	1.29	
$Bi_{0.8}Ba_{0.2}FeO_3$	Bi_2O_3	12.49	20
	Fe_2O_3	5.35	
	$BaCO_3$	2.64	
$Bi_{0.7}Ba_{0.3}FeO_3$	Bi_2O_3	11.2	20
	Fe_2O_3	5.48	
	$BaCO_3$	4.06	
$Bi_{0.7}Ba_{0.3}Fe_{0.9}Ti_{0.1}O_3$	Bi_2O_3	11.21	20
	Fe_2O_3	5.22	
	$BaCO_3$	4.06	
	TiO_2	0.27	

3.3.2 Milling

The main purpose of milling was mixing and homogenization. At first, the powder mixtures were milled manually using a mortar and pestle. Next the hand milled powders were ball milled using laboratory type grinding bowl made of Silicon Nitride (Si_3N_2). Balls made of Si_3N_2 having dia of 10 mm were used together with acetone (purity>99%) as milling media. The grinding balls and the materials in the grinding bowl are acted upon by the centrifugal forces due to the rotation of the grinding bowl about its own axis and due to the rotating supporting disk. The grinding bowl

and the supporting disc rotate in opposite directions, so that the centrifugal forces alternately act in the same and opposite directions.

Before adding the powder in the milling pot, the balls and the pot were cleaned ultrasonically to remove slightest of dust which may show up as impurity in the final structure with resultant harmful properties. The balls usually stay at the bottom of the pot having the added powders on top of them. Then, after adding sufficient amount of acetone the mouth of pot was closed tightly and shaken to mix the ingredients. Finally the powders were milled at 120 rpm to get a homogenize mixture**.**

After milling the extracted powders were dried; for quick drying powders were kept at 100°C for at least 2 to 3 hours. It is very important to dry the powders completely otherwise they cannot be pressed properly to get the desired shape.

3.3.4 Compaction

Around 1 gm of powder was pressed into pellets using pressure of 40 KN and the pellets were held under the pressure for 1 minute using a pressing unit (Herzog, Model No. HTP 40, Japan). After ejecting the pellets from the dies the pellets were dried in an oven and then lightly ground with grit #800 SiC paper to a smooth surface, removing surface irregularities. Green densities of the samples were measured before the pellets were sintered. Green samples were not made thick to avoid density variation. The compaction process is shown in figure 3.2.

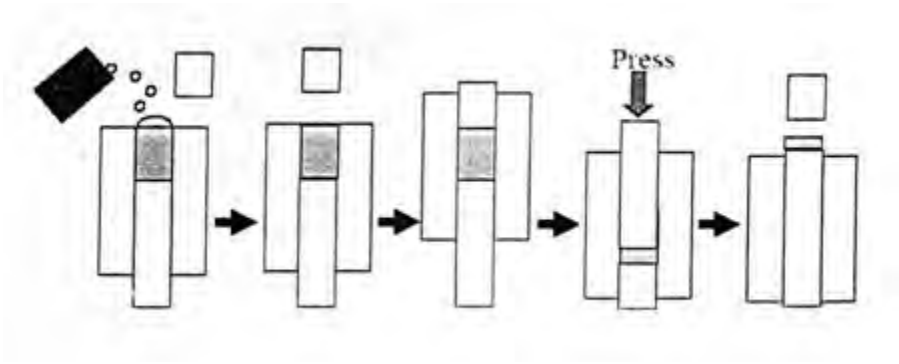

Figure 3.2: Schematic representation of compaction process.

3.3.5 Sintering

Muffle Furnace (Nabertherm Gmblt Bahnhofstr, 20, Lilienthal / Bremen Germany) was used to sinter the disk shaped samples in air atmosphere.

Figure 3.3: Furnace used for sintering ceramics sample.

The basic sintering cycles used in the experiments is shown in Figure 3.4. The maximum sintering temperature, sintering rate and cooling rate were varied to find the optimum between percent theoretical density and grain size so that the density of the sample increases significantly.

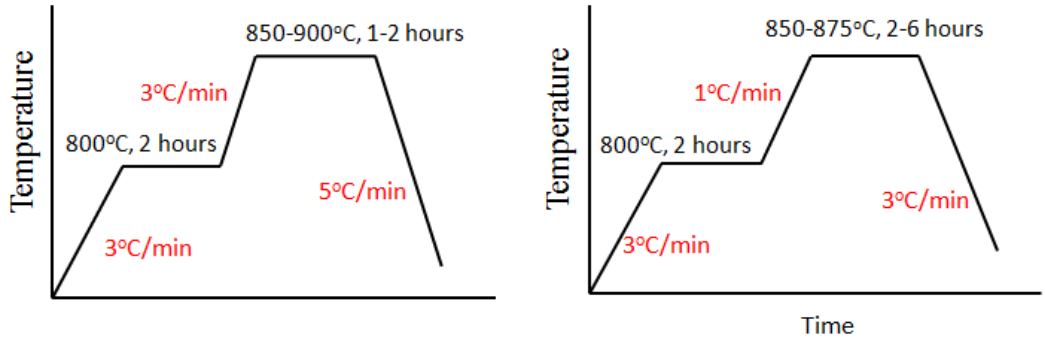

Figure 3.4: Sintering cycles

The sintering temperature, sintering rate, and the soaking time were modified progressively as the experiment proceeds on trial and error basis. Different parameters applied are shown in the table below:

Table 3.3: Table showing experimental parameters applied.

Experiment No.	Heating Rate °C/min	Binder Removal Temperature (°C)	Dwell Time (Hour)	Sintering Rate (°C/min)	Maximum Sintering Temperature (°C)	Holding Time (min)	Cooling Rate (°C/min)	End Temp. (°C)
1	**3**	**800**	**2**	**3**	**850**	**1**	**5**	**40**
2	**3**	**800**	**2**	**3**	**850**	**2**	**5**	**40**
3	**3**	**800**	**2**	**3**	**875**	**1**	**5**	**40**
4	**3**	**800**	**2**	**3**	**875**	**2**	**5**	**40**
5	**3**	**800**	**2**	**3**	**900**	**1**	**5**	**40**
6	**3**	**800**	**2**	**3**	**900**	**2**	**5**	**40**
7	**3**	**800**	**2**	**1**	**850**	**2**	**3**	**40**
8	**3**	**800**	**2**	**1**	**850**	**4**	**3**	**40**
9	**3**	**800**	**2**	**1**	**875**	**2**	**3**	**40**
10	**3**	**800**	**2**	**1**	**875**	**4**	**3**	**40**
11	**3**	**800**	**2**	**1**	**875**	**6**	**3**	**40**

The dwell time at the primary stages was set to remove the binder and for calcination. It is important to keep the heating rate low up to this point otherwise during binder burning samples may crack. The heating rate may be changed at each stage depending upon the composition and the sample‘s tendency to warp during sintering.

3.3.6 Post sintering operations

Post sintering operations are necessary to measure different material properties.

To measure dielectric properties, samples were grinded, polished and particular geometric shape was given such as rectangle, square or triangle to measure dielectric constant. 120 grit paper of SiC was used for rough polishing.

For field emission scanning electron microscopy (FESEM) samples were cleaned in acetone and dried in oven for 30 minutes. As the ceramic samples were non-conducting, they were coated with platinum dust by ion sputtering method in order to make them conducting which was essential for FESEM observations.

3.4 Property measurement

3.4.1 Percent theoretical density measurement

After completion of sintering dimensions of disk shape samples were measured with digital micrometer as well as slide callipers and samples were weighed by electronic balance. Percent theoretical density (%TD) achieved was calculated by comparing the actual and theoretical density. Theoretical densities are listed below for the tested compositions.

Table 3.4: Theoretical densities of different composition.

Material	Theoretical Density g/cm^3
$Bi_{0.9}Ba_{0.1}FeO_3$	8.14
$Bi_{0.8}Ba_{0.2}FeO_3$	7.95
$Bi_{0.7}Ba_{0.3}FeO_3$	7.76
$Bi_{0.7}Ba_{0.3}Fe_{0.9}Ti_{0.1}O_3$	7.72

3.4.2 Microstructure study

To observe ceramics sample in FESEM (JEOL JSM 7600F), sample was made conductive, coated with platinum by ion sputtering method. Then sample was mounted on a holder and inserted in FESEM.

Figure 3.5: Field Emission Scanning Electron Microscope (FESEM).

The micrographs obtained from FESEM analysis was used for microstructural study which include grain size measurement, porosity observation etc.

3.4.3 Phase study

X-ray diffraction analysis was conducted using the XRD (Bruker D8 Advance) facility in order to determine the phases present in the samples

Figure 3.6: XRD Machine.

X-rays are a type of electromagnetic radiation. The wavelength of x-rays is approximately 1 Å which has the same size equivalent to that of an atom. X-ray diffraction (XRD) is a non-destructive analytical technique mainly used for the phase identification and structural characterization of crystalline materials. X-ray diffraction combined with Rietveld analysis, provides detailed information regarding unit cell dimensions, bond-lengths, bond-angles and the site ordering of crystallites.

The relationship between the wavelengths of the X-rays λ, the incidence angle q, and spacing between two crystal lattice planes (hkl) d, is shown in the Bragg's Law expressed as:

$$2d_{hkl} \sin q = n\lambda \qquad (3.1)$$

After characterization by X-ray diffraction, a number of peaks are seen in the diffraction patterns. These patterns are identified by comparing their positions and relative intensities with the known structures in the database. Sometimes extra peaks might appear due to the impurity or structural transformation after thermal treatment. In fact, the intensities, widths and positions of peaks in the patterns reflect information about structure, quantity, texture etc. of crystallites.

3.4.4 Dielectric property measurement

An impedance analyzer (WAYNE KERR 6500B series) was used to measure the dielectric property of samples. All the measurements were subjected to AC current only.

First of all samples were prepared properly to measure dielectric properties correctly. Samples were kept clean and dry. They were polished with 120 grit paper in order to produce crack free solid sample. Samples were given geometrical shape commonly rectangle in order to measure the area. Sample thickness was kept quite uniform which was essential for correct measurement. Then after taking dimensions, silver paint was applied on both sides of the sample keeping the edges clean. Next the samples were kept in the holder of the impedance analyzer to measure the properties.

Figure 3.7: Impedance Analyzer.

Both room temperature and high temperature frequency dependency were measured. Dielectric constant was measured from the capacitance value obtained from the analyzer according to equation as below –

$$k = C_p\, d/(A\varepsilon_0) \qquad (3.2)$$

In equation 3.21, k' is the dielectric constant, C_p is the capacitance value measured by the impedance analyzer, d is the thickness of the sample, ε_0 is the permittivity of vacuum, A is the area of the sample in contact with the conducting layer.

A set up of tube furnace type oven accompanied with custom sample holder was used to heat the sample during high temperature property measurement

3.4.5 Thermal Analysis

Thermal analysis was conducted using Differential Thermal Analyzer (Brand: Seiko Instruments, Model: EXSTAR6000) to study the ferroelectric transition point.

Figure 3.8: Differential Thermal Analyzer.

The technique is based on the facts that as a substance is heated, it undergoes reactions and phase changes that involve absorption or emission of heat. In DTA the temperature of the test material is measured relative to that of an adjacent inert material. A thermocouple imbedded in the test piece and another in the inert material are connected so that any differential temperatures generated during the heating cycle are graphically recorded as a series of peaks on a moving chart. The amount of heat involved and temperature at which these changes take place are characteristic of individual elements or compounds.

According to literature at ferroelectric transition point $BiFeO_3$ undergoes a phase change. So, DTA was conducted in the temperature range of 200-900°C to find out this phase transition point.

3.4.6 Magnetic property measurement

The M-H (magnetisation- magnetic field) curve of the samples was measured using Vibrating sample magnetometer (VSM, Model: MicroSense).

Figure 3.9: Vibrating Sample Magnetometer.

A vibrating sample magnetometer or VSM is a scientific instrument that measures magnetic properties, invented in 1955 by Simon Foner at Lincoln Laboratory MIT. In VSM a sample is placed inside a uniform magnetic field to magnetize the sample. The sample is then physically vibrated sinusoidally, typically through the use of a piezoelectric material. The induced voltage in the pickup coil is proportional to the sample's magnetic moment, but does not depend on the strength of the applied magnetic field. In a typical setup, the induced voltage is measured through the use of a lock-in amplifier using the piezoelectric signal as its reference signal. By measuring in the field of an external electromagnet, it is possible to obtain the hysteresis curve of a material. The vibrating sample magnetometer measures the magnetization of a small sample of magnetic material placed in an external magnetizing field by converting the dipole field of the sample into an ac electrical signal.

CHAPTER 4
RESULTS AND DISCUSSION

4.1 Introduction

As mentioned earlier in section 1.3, the main target of this thesis project was to enhance both ferromagnetic and dielectric properties of pure $BiFeO_3$ by modifying its structure and develop structure-property relationship. To achieve this target $BiFeO_3$ was doped with Ba^{2+} and Ti^{4+}. For this purpose the starting materials used were Bi_2O_3, Fe_2O_3, $BaCO_3$ and TiO_2.

The A-site substitution by barium ion (Ba^{2+}) has been attempted by many authors in recent years to enhance the multiferroic properties of $BiFeO_3$. Ba^{2+} having a large ionic radius than Bi^{3+} distorts the original structure of $BiFeO_3$ and changes it‘s cycloidal spin structure to a canted spin structure resulting in net magnetization at room temperature. Moreover, addition of Ba also significantly reduces the oxygen vacancy related defects (leakage current) by occupying evaporated Bi sites and increases the electrical resistivity of BFO by controlling grain size, thus allowing high dielectric constant to be determined at room temperature [6, 29].

Nevertheless, an enhancement in ferromagnetic properties of BFO with increasing Ba concentration may be expected due to increasing structural distortion. Hence barium was doped at three mole fractions in $Bi_{1-x}Ba_xFeO_3$, viz. x = 0.1, 0.2 and 0.3 in this thesis. So, the first three Ba-doped composition chosen for this thesis were: 1) $Bi_{0.9}Ba_{0.1}FeO_3$ 2) $Bi_{0.8}Ba_{0.2}FeO_3$ and 3) $Bi_{0.7}Ba_{0.3}FeO_3$. However, the substitution of Ba^{2+} for Bi^{3+} may cause two parallel phenomena with respect to concentration of oxygen vacancies, one is decrease in concentration of oxygen vacancies by filling the probable vacant volatized Bi^{3+} sites and the second is the creation of oxygen vacancies to neutralize the charge produced by substituting Ba^{2+} for Bi^{3+}. After an optimum Ba^{2+} doping, when all the vacant Bi^{3+} sites are filled up, addition of excessive Ba^{2+} creates oxygen vacancies by substituting Bi^{3+} ions due to its lower charge (+2) than the bismuth ion (+3). Hence, leakage current of BFO decreases up to an optimum Ba doping and then again increases on further doping. It has been reported that, above 0.2 mole fraction Ba^{2+} addition (x=0.2) the leakage current effect becomes prominent again [6, 27]. To reduce this negative effect of excessive Ba, a higher charged ion than Fe^{3+} (Ti^{4+} in this thesis) can be co-doped at B-site [7]. Addition of Ti^{4+} can decrease the charge defects and increase the electrical resistivity of

BFO. So, to stabilize the dielectric constant of $Bi_{1-x}Ba_xFeO_3$ (x=0.3) samples the forth composition chosen was $Bi_{1-x}Ba_xFe_{1-y}Ti_yO_3$ (x=0.3, y=0.1).

The initial challenge of the experiment was to determine the optimum sintering zone for all the four compositions. The optimum sintering temperature should result in fine grained (~1µm) dense (above 95 percent theoretical density) samples which are prerequisite of improved dielectric and magnetic properties [76-78]. From literature, the sintering temperature was revealed to be above 850^0C for doped bismuth ferrite [6, 29, 30] but these works did not focus on developing optimum microstructure for each doped compositions, rather they applied a single sintering temperature for all compositions and compared their property. Moreover, no previous work has been conducted on Ba^{2+} and Ti^{4+} doped $BiFeO_3$ in our department. So a trial and error method was employed to determine the correct sintering temperature for each composition that would optimize their microstructure. At first, sintering was conducted in the range of 850 to 900^oC for 1-2 hours using cycle-1 (Figure 4.1) and effect of doping concentration on the sintering condition was studied.

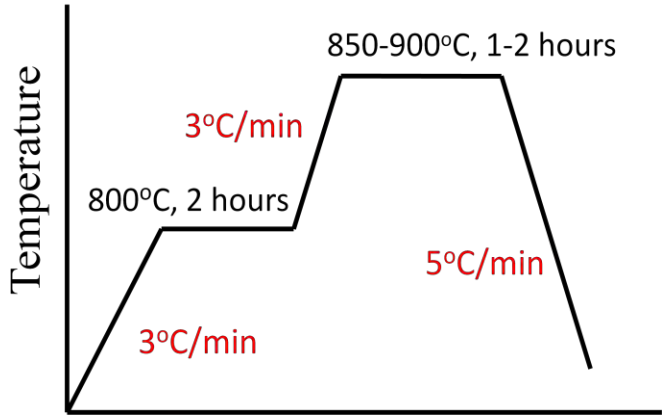

Figure 4.1: Sintering cycle-1.

The percent theoretical density and average grain size of $Bi_{1-x}Ba_xFe_{1-y}Ti_yO_3$ (x = 0.1, y = 0.0; x = 0.2, y = 0.0; x = 0.3, y = 0.0; and x = 0.1, y = 0.1) samples sintered in the range of 850-900^oC for holding times 1 and 2 hours are tabulated in Table 4.1.

Table 4.1: Percent theoretical density (%TD) and average grain size (<Grain Size>) of $Bi_{1-x}Ba_xFe_{1-y}Ti_yO_3$ ceramics sintered at temperatures from 850 to 900°C.

Sl No.	Sintering Cycle	Sintering Temperature (°C)	Holding Time (hours)	Composition	%TD	<Grain Size> µm
1	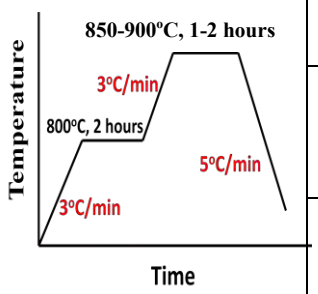 **Cycle-1**	850	1	$Bi_{0.9}Ba_{0.1}FeO_3$	92-94	0.6-0.7
				$Bi_{0.8}Ba_{0.2}FeO_3$	65-70	<0.2
				$Bi_{0.7}Ba_{0.3}FeO_3$	65-70	<0.2
				$Bi_{0.7}Ba_{0.3}Fe_{0.9}Ti_{0.1}O_3$	65-70	<0.2
2		850	2	$Bi_{0.9}Ba_{0.1}FeO_3$	>95	0.8-0.9
				$Bi_{0.8}Ba_{0.2}FeO_3$	65-70	<0.2
				$Bi_{0.7}Ba_{0.3}FeO_3$	65-70	<0.2
				$Bi_{0.7}Ba_{0.3}Fe_{0.9}Ti_{0.1}O_3$	65-70	<0.2
3		875	1	$Bi_{0.9}Ba_{0.1}FeO_3$	>95	6-7
				$Bi_{0.8}Ba_{0.2}FeO_3$	75-80	<0.4
				$Bi_{0.7}Ba_{0.3}FeO_3$	75-80	<0.4
				$Bi_{0.7}Ba_{0.3}Fe_{0.9}Ti_{0.1}O_3$	75-80	<0.4
4		875	2	$Bi_{0.9}Ba_{0.1}FeO_3$	>95	6-7
				$Bi_{0.8}Ba_{0.2}FeO_3$	80-82	<0.4
				$Bi_{0.7}Ba_{0.3}FeO_3$	80-82	<0.4
				$Bi_{0.7}Ba_{0.3}Fe_{0.9}Ti_{0.1}O_3$	80-82	<0.4
5		900	1	$Bi_{0.9}Ba_{0.1}FeO_3$	>95	8
				$Bi_{0.8}Ba_{0.2}FeO_3$	93-94	0.5-0.6
				$Bi_{0.7}Ba_{0.3}FeO_3$	92-93	0.45-0.5
				$Bi_{0.7}Ba_{0.3}Fe_{0.9}Ti_{0.1}O_3$	88-90	0.4-0.45
6		900	2	$Bi_{0.9}Ba_{0.1}FeO_3$	>95	10
				$Bi_{0.8}Ba_{0.2}FeO_3$	94.5-95.5	.65-.75
				$Bi_{0.7}Ba_{0.3}FeO_3$	94-95	0.55-0.65
				$Bi_{0.7}Ba_{0.3}Fe_{0.9}Ti_{0.1}O_3$	93-94	0.45-0.55
7	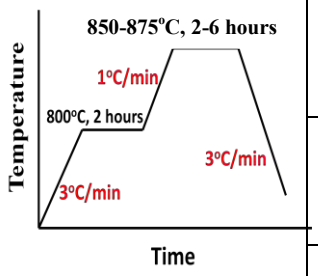 **Cycle-2**	850	2	$Bi_{0.9}Ba_{0.1}FeO_3$	>95	1.0-1.1
				$Bi_{0.8}Ba_{0.2}FeO_3$	90-93	<0.4
				$Bi_{0.7}Ba_{0.3}FeO_3$	80-82	<0.4
				$Bi_{0.7}Ba_{0.3}Fe_{0.9}Ti_{0.1}O_3$	80-82	<0.4
8		850	4	$Bi_{0.9}Ba_{0.1}FeO_3$	>95	2.0-2.3
				$Bi_{0.8}Ba_{0.2}FeO_3$	90-93	<0.5
				$Bi_{0.7}Ba_{0.3}FeO_3$	85-90	<0.4
				$Bi_{0.7}Ba_{0.3}Fe_{0.9}Ti_{0.1}O_3$	85-90	<0.4
9		875	2	$Bi_{0.9}Ba_{0.1}FeO_3$	>95	6-7
				$Bi_{0.8}Ba_{0.2}FeO_3$	>95	0.95-1.0
				$Bi_{0.7}Ba_{0.3}FeO_3$	90-93	0.65-0.75
				$Bi_{0.7}Ba_{0.3}Fe_{0.9}Ti_{0.1}O_3$	90-93	0.55-0.65
10		875	4	$Bi_{0.9}Ba_{0.1}FeO_3$	>95	6-7
				$Bi_{0.8}Ba_{0.2}FeO_3$	>95	1.5-1.7
				$Bi_{0.7}Ba_{0.3}FeO_3$	>95	0.95-1.0
				$Bi_{0.7}Ba_{0.3}Fe_{0.9}Ti_{0.1}O_3$	>95	0.7-0.8
11		875	6	$Bi_{0.9}Ba_{0.1}FeO_3$	>95	8
				$Bi_{0.8}Ba_{0.2}FeO_3$	>95	1.8-2.0
				$Bi_{0.7}Ba_{0.3}FeO_3$	>95	1.5-1.7
				$Bi_{0.7}Ba_{0.3}Fe_{0.9}Ti_{0.1}O_3$	>95	1.0-1.05

For the $Bi_{0.9}Ba_{0.1}FeO_3$ samples, sintering at 850°C for a holding time of 1-2 hours proved to be adequate resulting in percent theoretical density (%TD) above 90% and satisfactory average grain size. Although the %TD for this sample increased with increasing sintering temperature above 850°C but it was associated with liquification in the structure due to excessive sintering.

However, the %TD and average grain size deteriorated significantly, with increasing additions of Ba at each sintering temperature. For $Bi_{0.8}Ba_{0.2}FeO_3$, $Bi_{0.7}Ba_{0.3}FeO_3$ and $Bi_{0.7}Ba_{0.3}Fe_{0.9}Ti_{0.1}O_3$ samples the %TD was below 70% at 850°C. Although the % TD increased to above 90% for these compositions with increasing sintering temperature to 900°C, but the average grain size was still below satisfactory due to insufficient time provided at higher time. Also, sintering temperature of 900°C proved to be excessive for these samples causing distortion in the samples.

From the results of sintering cycle-1 we derived some conclusions:

(i) The optimum sintering temperature should be different for all compositions.
(ii) For $Bi_{0.9}Ba_{0.1}FeO_3$ samples, the optimum sintering temperature should not be above 850°C as liquification starts in the structure due to over sintering.
(iii) For $Bi_{0.8}Ba_{0.2}FeO_3$, $Bi_{0.7}Ba_{0.3}FeO_3$ and $Bi_{0.7}Ba_{0.3}Fe_{0.9}Ti_{0.1}O_3$ samples, optimum sintering temperature should be below 900°C as excessive sintering temperature caused distortion in these samples.
(iv) More time is required at high temperatures for all compositions for proper grain growth and densification.

However, to overcome the deficiencies of sintering cycle-1 and to provide enough time to all compositions for proper densification and grain growth, next sintering was conducted the range of 850 to 875°C using cycle-2 (Figure 4.2). The sintering rate above 800°C was lowered to 1°C/min from 3°C/min and the cooling rate was lowered to 3°C/min from 5°C/min to allow sufficient time at higher temperature. The %TD and average grain size of $Bi_{1-x}Ba_xFe_{1-y}Ti_yO_3$ (x = 0.1, y = 0.0; x = 0.2, y = 0.0; x = 0.3, y = 0.0; and x = 0.3, y = 0.1) samples sintered in the range of 850-875°C using cylcle-2 are tabulated in Table 4.1.

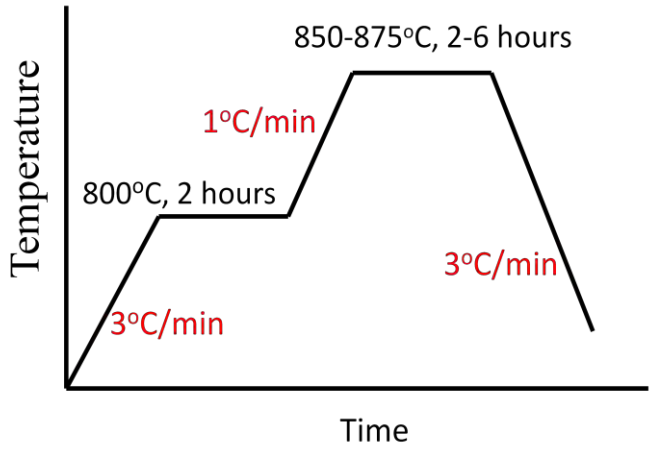

Figure 4.2: Sintering cycle-2.

Optimization of the microstructure was achieved for all compositions under this cycle. For the $Bi_{0.9}Ba_{0.1}FeO_3$ samples, sintering at 850°C for 2 hours proved to be sufficient resulting in percent theoretical density (%TD) above 95% and 1.0-1.1μm average grain size. Increasing the holding time to 4 hours at 850°C resulted in excessive grain growth for this sample which has a detrimental effect on dielectric properties. However, the %TD and average grain size deteriorated significantly at 850°C, with increasing additions of Ba. Addition of Ba severely inhibited the densification process and resulted in porous samples of reduced compactness. Sintering at 850°C for 2 and 4 hours was inadequate to offer sufficient energy for proper coalescence for these samples hence resulting in poor densification. These results clearly indicated the necessity for higher temperature of sintering in order to obtain proper densification, especially for $Bi_{1-x}Ba_xFe_{1-y}Ti_yO_3$ (x = 0.2, y = 0.0; x = 0.3, y = 0.0; and x = 0.3, y = 0.1) samples where the pinning effect of Ba inhibits the densification process.

For $Bi_{0.8}Ba_{0.2}FeO_3$ samples optimization (%TD >95% and grain size ~ 0.95-1.0 μm) was achieved when the sintering temperature was increased to 875°C and held there for 2 hours. Similarly, for $Bi_{0.7}Ba_{0.3}FeO_3$ and $Bi_{0.7}Ba_{0.3}Fe_{0.9}Ti_{0.1}O_3$ samples optimization of the structure was achieved at 875°C for 4 and 6 hours holding time respectively. The optimum sintering conditions for all the compositions have been tabulated in Table 4.2.

Table 4.1: Key experimental results showing optimum sintering condition for all four compositions

Sample ID	Composition	Sintering Temperature (^oC)	Holding Time (hours)	Percent Theoretical Density (%TD)	<Grain Size> µm
T1	$\mathbf{Bi_{0.9}Ba_{0.1}FeO_3}$	850	2	>95	1.0-1.1
T2	$\mathbf{Bi_{0.8}Ba_{0.2}FeO_3}$	875	2	>95	0.95-1.0
T3	$\mathbf{Bi_{0.7}Ba_{0.3}FeO_3}$	875	4	>95	0.95-1.0
T4	$\mathbf{Bi_{0.7}Ba_{0.3}Fe_{0.9}Ti_{0.1}O_3}$	875	6	>95	1.0-1.05

The $Bi_{0.9}Ba_{0.1}FeO_3$ sample with optimum sintering condition was given Sample ID: T1. Accordingly $Bi_{0.8}Ba_{0.2}FeO_3$, $Bi_{0.7}Ba_{0.3}FeO_3$ and $Bi_{0.7}Ba_{0.3}Fe_{0.9}Ti_{0.1}O_3$ compositions with optimum microstructure was named T2, T3 and T4 respectively. After developing the microstructure the structure and properties of the four compositions were compared.

The XRD analysis of the T1, T2, T3 and T4 samples confirmed the formation of R3c type perovskite structure with increase in structural distortion with increasing Ba concentration.

Magnetization-Magnetic field (M-H) hysteresis loop was measured for all the compositions with optimum structure. As expected from the XRD results, the magnetization of the samples was found to increase from T1 to T4 sample with increase in Ba concentration due to increasing lattice distortion. The lattice distortion changes the cycloidal spin structure of pure BFO to canted spin structure and results in net magnetization.

In contrast to pure BFO, Ba doped BFO showed superior values of dielectric constant due to decrease in leakage current. The dielectric constant value increased with Ba addition up to 0.2 mole fraction (Sample ID: T2) than decreased again for $Bi_{0.7}Ba_{0.3}FeO_3$ sample (Sample ID: T3) due to formation of oxygen vacancies by the excess Ba^{2+} addition. However, the dielectric constant for $Bi_{0.7}Ba_{0.3}FeO_3$ samples (Sample ID: T2) was stabilized by Ti^{4+} doping at B-site in $Bi_{0.7}Ba_{0.3}Fe_{0.9}Ti_{0.1}O_3$ samples (Sample ID: T4).

DTA analysis revealed that the peak for ferroelectric transition (T_C) shifted towards higher temperatures for the Ba-substituted ceramics and reached to 870°C for T4 samples. Thus doped BFO exhibited ferroelectric characteristics over a wider temperature range than pure BFO.

The best combination of dielectric properties and magnetization was obtained for $Bi_{0.7}Ba_{0.3}Fe_{0.9}Ti_{0.1}O_3$ samples (Sample ID: T4) having average grain size between of 1.0-1.05 μm and % TD above 95%.

4.2 Dependence of percent theoretical density and <grain size> on sintering temperature and doping concentration

The percent theoretical density (%TD) and average grain size of $Bi_{1-x}Ba_xFe_{1-y}Ti_yO_3$ (x = 0.1, y = 0.0; x = 0.2, y = 0.0; x = 0.3, y = 0.0; and x = 0.3, y = 0.1) samples sintered under cycle-1 and cycle-2 have been tabulated in Table 4.1.

For $Bi_{1-x}Ba_xFe_{1-y}Ti_yO_3$ samples sintered using cycle-1 in the temperature range 850-900°C,the variation of percent theoretical density with sintering temperature for 1 and 2 hours of holding time are shown in figure 4.3 and 4.4 respectively. From figure 4.3 and 4.4 it is obvious that the %TD of $Bi_{0.9}Ba_{0.1}FeO_3$ ceramics are least affected by temperature in comparison to the ceramics with higher addition of Ba. The small amount of Ba present in this sample did not hamper the densification process, so high %TD was attained even at low temperature. However, the samples that have a higher concentration of Ba exhibit a sharp increase in %TD during the transition of sintering temperature from 850 to 900°C. Similar effect is observed for the co-doped sample. This effect is more prominent when the holding time is increased from 1 to 2 hours as shown in figure 4.4. This implies that at sintering temperatures above 850°C the pinning effect of Ba and even Ti becomes less significant. Moreover, this pinning effect becomes even less significant when the holding time is increased. All samples sintered at 900°C for 2 hours have a % TD above 90%

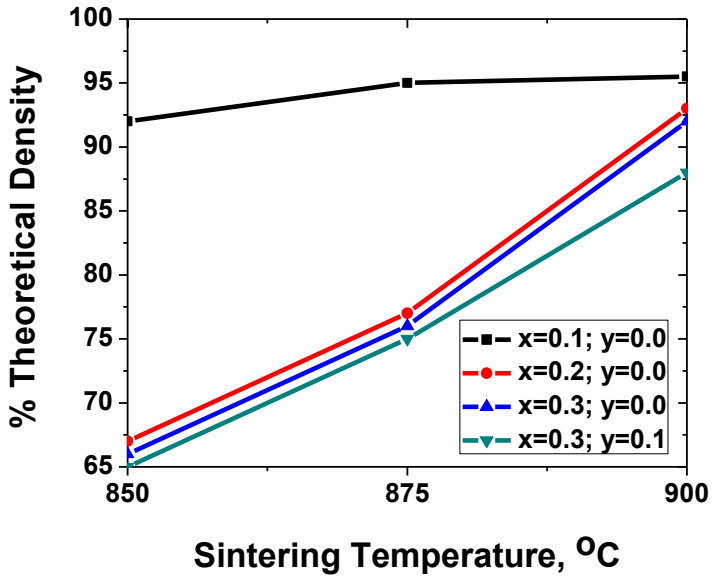

Figure 4.3: Variation of percent theoretical density with sintering temperature of $Bi_{1-x}Ba_xFe_{1-y}Ti_yO_3$ (x = 0.1, y = 0.0; x = 0.2, y = 0.0; x = 0.3, y = 0.0; and x = 0.3, y = 0.1) ceramics for **1 hour holding time at the sintering temperature**.

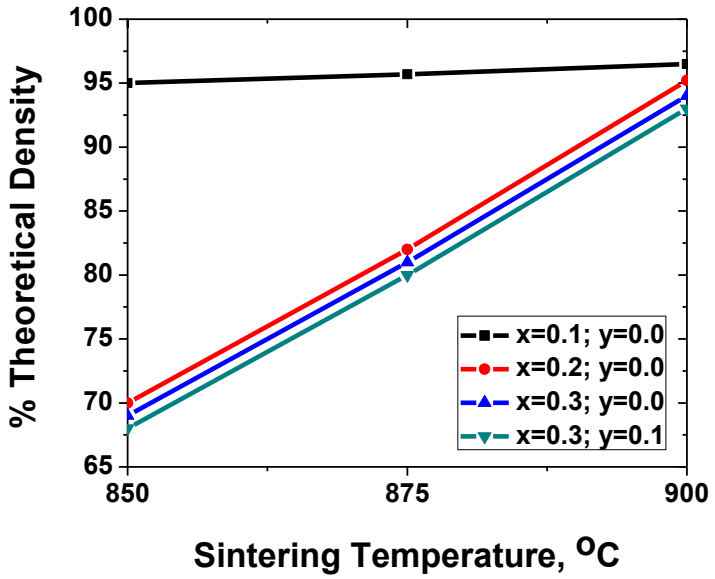

Figure 4.3: Variation of percent theoretical density with sintering temperature of $Bi_{1-x}Ba_xFe_{1-y}Ti_yO_3$ (x = 0.1, y = 0.0; x = 0.2, y = 0.0; x = 0.3, y = 0.0; and x = 0.3, y = 0.1) ceramics for **2 hours holding time at the sintering temperature**.

Figure 4.5 and 4.6 show the variation of %TD with doping concentration for $Bi_{1-x}Ba_xFe_{1-y}Ti_yO_3$ (x = 0.1, y = 0.0; x = 0.2, y = 0.0; x = 0.3, y = 0.0; and x = 0.3, y = 0.1) ceramics sintered using cycle-1 at holding times of 1 and 2 hours respectively. Both figures confirm that with increasing additions of barium (Ba) the %TD decreases at each sintering temperature. Titanium (Ti) also,

along with Ba inhibits densification in $Bi_{0.7}Ba_{0.9}Fe_{0.9}Ti_{0.1}O_3$ sample. Ba addition suppresses the grain growth during sintering by pinning of grain boundaries thus resulting in poorer densification and hence lower %TD.

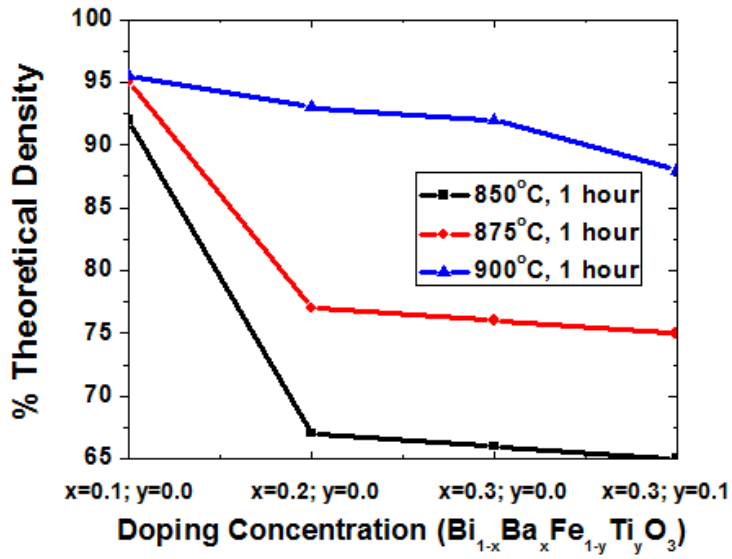

Figure 4.5: Variation of percent theoretical density with doping concentration of $Bi_{1-x}Ba_xFe_{1-y}Ti_yO_3$ (x = 0.1, y = 0.0; x = 0.2, y = 0.0; x = 0.3, y = 0.0; and x = 0.3, y = 0.1) ceramics for **1 hour holding time at the sintering temperature**.

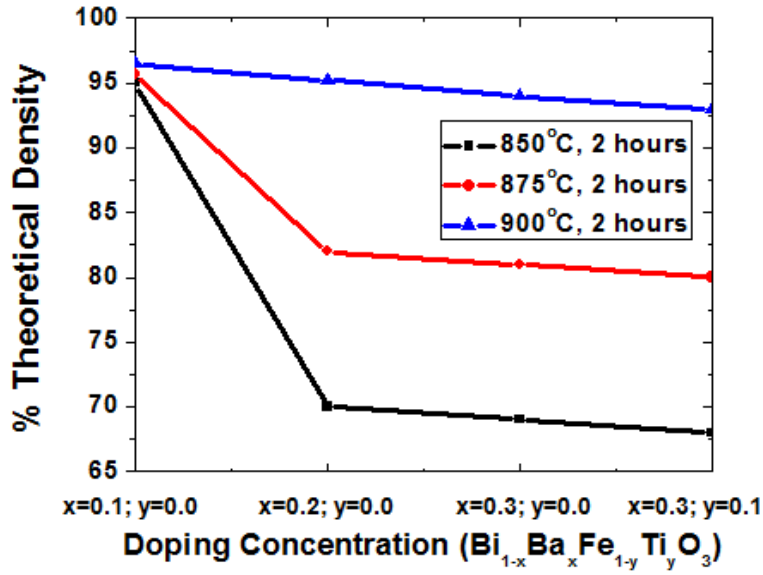

Figure 4.6: Variation of percent theoretical density with doping concentration of $Bi_{1-x}Ba_xFe_{1-y}Ti_yO_3$ (x = 0.1, y = 0.0; x = 0.2, y = 0.0; x = 0.3, y = 0.0; and x = 0.3, y = 0.1) ceramics for **2 hours holding time at the sintering temperature**.

Figure 4.7 and 4.8 show the variation of average grain size with sintering temperature for holding time of 1 and 2 hours respectively for the same samples. From both figures it is clear that with an increase in sintering temperature the average grain size increases due to the increased rate of diffusion at higher temperatures. However, as expected this effect is most prominent in the $Bi_{0.9}Ba_{0.1}FeO_3$ samples where average grain size increases from ~0.9 µm at 850°C to 10µm at 900°C for a holding time of 2 hours at both temperatures. As stated earlier this is due to the presence of less amount of Ba in $Bi_{0.9}Ba_{0.1}FeO_3$ samples. Ba suppresses grain growth as a result of its pinning effect. So, in samples containing higher concentration of Ba the average grain size increases only slightly with sintering temperature and this increase is much less prominent than in the case of $Bi_{0.9}Ba_{0.1}FeO_3$ ceramics (Figure 4.7 and 4.8). For the $Bi_{0.7}Ba_{0.9}Fe_{0.9}Ti_{0.1}O_3$ samples, Ti along with Ba acts as grain growth inhibitor and the average grain size slightly increases from ~0.2µm at 850°C to ~0.5µm at 900°C for a holding time of 2 hours at both the temperatures.

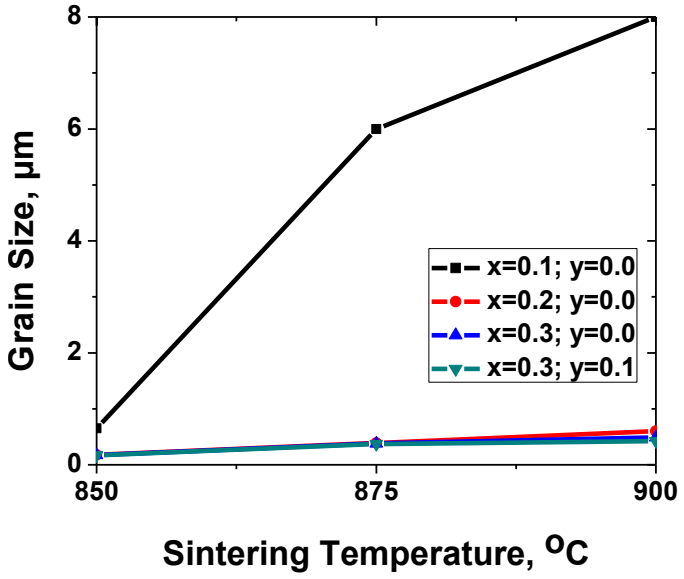

Figure 4.7: Variation of <grain size> with sintering temperature of $Bi_{1-x}Ba_xFe_{1-y}Ti_yO_3$ (x = 0.1, y = 0.0; x = 0.2, y = 0.0; x = 0.3, y = 0.0; and x = 0.3, y = 0.1) ceramics for **1 hour holding time at the sintering temperature**.

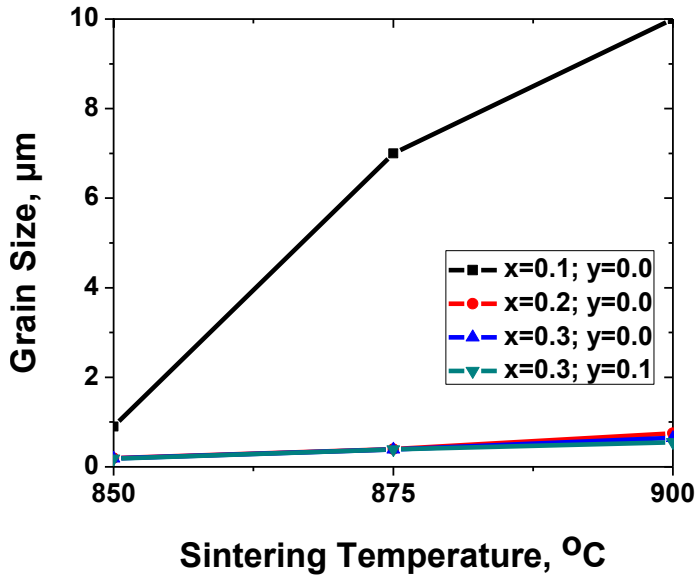

Figure 4.8: Variation of < grain size> with sintering temperature of $Bi_{1-x}Ba_xFe_{1-y}Ti_yO_3$ (x = 0.1, y = 0.0; x = 0.2, y = 0.0; x = 0.3, y = 0.0; and x = 0.3, y = 0.1) ceramics for **2 hours holding time at the sintering temperature**.

Also the variation of average grain size with doping concentration of $Bi_{1-x}Ba_xFe_{1-y}Ti_yO_3$ (x = 0.1, y = 0.0; x = 0.2, y = 0.0; x = 0.3, y = 0.0; and x = 0.3, y = 0.1) ceramics sintered using cycle-1 at holding time of 1 and 2 hours are shown in Figure 4.9 and 4.10 respectively . As expected, both figures confirm that the average grain size of the $Bi_{1-x}Ba_xFe_{1-y}Ti_yO_3$ ceramics decrease with the increase in concentration of the dopants (Ba and Ti) as a consequence of their pinning effect.

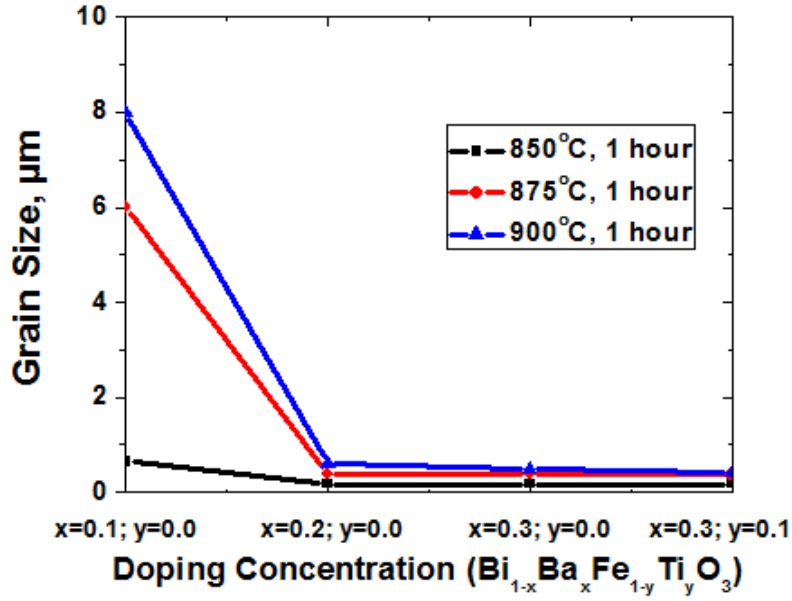

Figure 4.9: Variation of <grain size> with doping concentration of $Bi_{1-x}Ba_xFe_{1-y}Ti_yO_3$ (x = 0.1, y = 0.0; x = 0.2, y = 0.0; x = 0.3, y = 0.0; and x = 0.3, y = 0.1) ceramics for **1 hour holding time at the sintering temperature**.

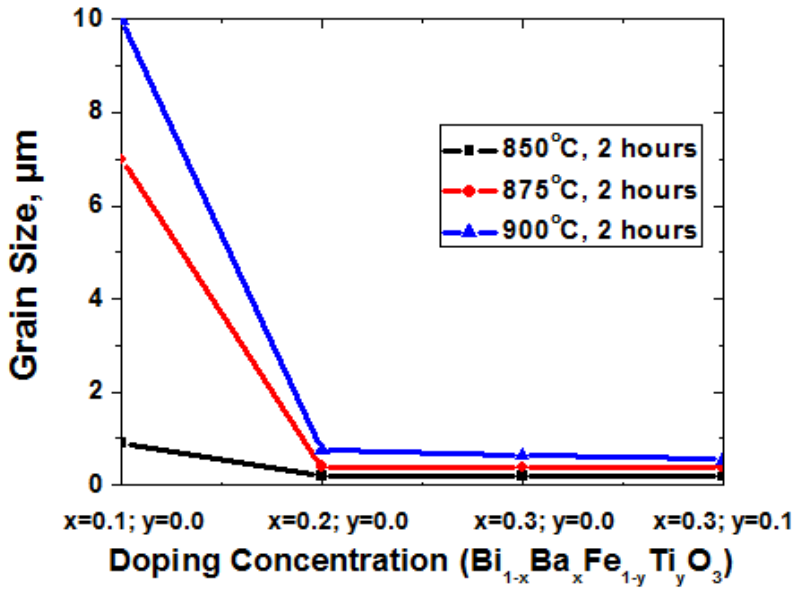

Figure 4.10: Variation of <grain size> with doping concentration of $Bi_{1-x}Ba_xFe_{1-y}Ti_yO_3$ (x = 0.1, y = 0.0; x = 0.2, y = 0.0; x = 0.3, y = 0.0; and x = 0.3, y = 0.1) ceramics for **2 hours holding time at the sintering temperature**.

Similar effects of temperature and doping concentration on the grain size and percent theoretical density were observed for $Bi_{1-x}Ba_xFe_{1-y}Ti_yO_3$ (x = 0.1, y = 0.0; x = 0.2, y = 0.0; x = 0.3, y = 0.0; and x = 0.3, y = 0.1) samples when sintered in the 850-875°C temperature range using cycle-2. The %TD and <grain size> was found to decrease with increasing doping concentration whereas the increasing sintering temperature and holding time lessened the pinning effect of the dopants causing an increase in %TD and grain size. These data have been reported in Table 4.1.

4.3 Microstructure development

As stated in section 1.3 one of the aims of this thesis was to determine optimum sintering condition for each doped compositions that will result in fine grain and dense microstructure.

Pure $BiFeO_3$ (BFO) is antiferromagnetic at room temperature due to its cycloidal spin structure and has low resistivity due to it‘s high leakage current. The excessive grain growth tendency of pure BFO at high %TD results in shorter grain boundary length, less resistance to electron flow and thus high leakage current. Both the ferromagnetic and dielectric properties of pure BFO can

be significantly improved by controlling the microstructure. Addition of dopants at A and B-sites distort the original structure of BFO, control grain growth and reduce oxygen vacancy related defects (leakage current). In this thesis, $Bi_{1-x}Ba_xFe_{1-y}Ti_yO_3$ (x = 0.1, y = 0.0; x = 0.2, y = 0.0; x = 0.3, y = 0.0; and x = 0.3, y = 0.1) samples were prepared by doping A and B-sites of pure BFO to improve it's multiferroic properties. The effect of these compositions on the microstructure was studied in this research as fine-grained (~1μm) structure and high density (>95% TD) of the doped $BiFeO_3$ are the prerequisite to obtain good dielectric and magnetic properties [75-78].

The prime challenge was to prepare single phase $Bi_{1-x}Ba_xFe_{1-y}Ti_yO_3$ ceramics with sufficiently low leakage current densities using solid state reaction method. The challenge can further be described by the reaction mechanisms shown in Eqs. 4.1– 4.5. Equations 4.1– 4.5 indicate that, if Bi_2O_3, Fe_2O_3, $BaCO_3$ and TiO_2 powders do not react with each other during the sintering process due to some specific reasons such as the volatilization of Bi_2O_3, insufficient mixing of powders, or inadequate sintering conditions, it will be difficult to form single-phase $Bi_{1-x}Ba_xFe_{1-y}Ti_yO_3$ ceramics [79, 80]. The reaction mechanisms are as follows:

$$Bi_2O_3 + Fe_2O_3 = (1 - x)\ BiFeO_3 + x/2\ (Bi_2O_3 + Fe_2O_3)\ \text{[no reaction]}, \quad (4.1)$$

$$(1 - x)Bi_2O_3 + x\ BaCO_3 + Fe_2O_3 = 2(1 - x)\ BiFeO_3 + x\ (BaCO_3 + Fe_2O_3)\ \text{[no reaction]}, \quad (4.2)$$

$$Bi_2O_3 + Fe_2O_3 = (4/25)\ Bi_{12}\ (Bi_{1/2}Fe_{1/2})\ O_{19} + (24/25)\ Fe_2O_3\ \text{[no reaction]}, \quad (4.3)$$

$$Bi_2O_3 + Fe_2O_3 = (1/18)\ Bi_{36}Fe_2O_{57} + (17/18)\ Fe_2O_3\ \text{[no reaction]}, \quad (4.4)$$

$$Bi_2O_3 + Fe_2O_3 = (1/2)\ Bi_2Fe_4O_9 + (1/2)\ Bi_2O_3\ \text{[volatilization or no reaction]}. \quad (4.5)$$

However, XRD analysis of $Bi_{1-x}Ba_xFe_{1-y}Ti_yO_3$ pellets calcined at 800°C for 2 hours followed by sintering at higher temperatures proved the formation of single phase. The XRD analysis of these pellets indicated that the initial raw materials: Bi_2O_3, Fe_2O_3, $BaCO_3$ and TiO_2 powders reacted completely with each other during the sintering process.

Our next challenge was to attain an optimum balance between percent theoretical density (% TD) and grain size to improve the multiferroic properties of the samples. From literature, it is evident that usually microstructures having ~1μm average (average) grain size and % TD above 95% provide good dielectric and magnetic properties [76-78]. According to data reported in literature,

the ceramics were first calcined at 800°C for 2 hours, Followed by calcinations, the samples were then sintered at 25°C intervals in the temperature range of 850-900°C for both 1 and 2 hours using cycle-1 (Figure 4.1) and the microstructure was studied. The optimization between % TD and grain size attained for most of the compositions was unsatisfactory after sintering in this temperature range.

Figure 4.11 shows the gradual elimination of porosity by increase in sintering temperature and a corresponding increase in grain size at higher temperatures for $Bi_{0.9}Ba_{0.1}FeO_3$ samples sintered using cycle 1.

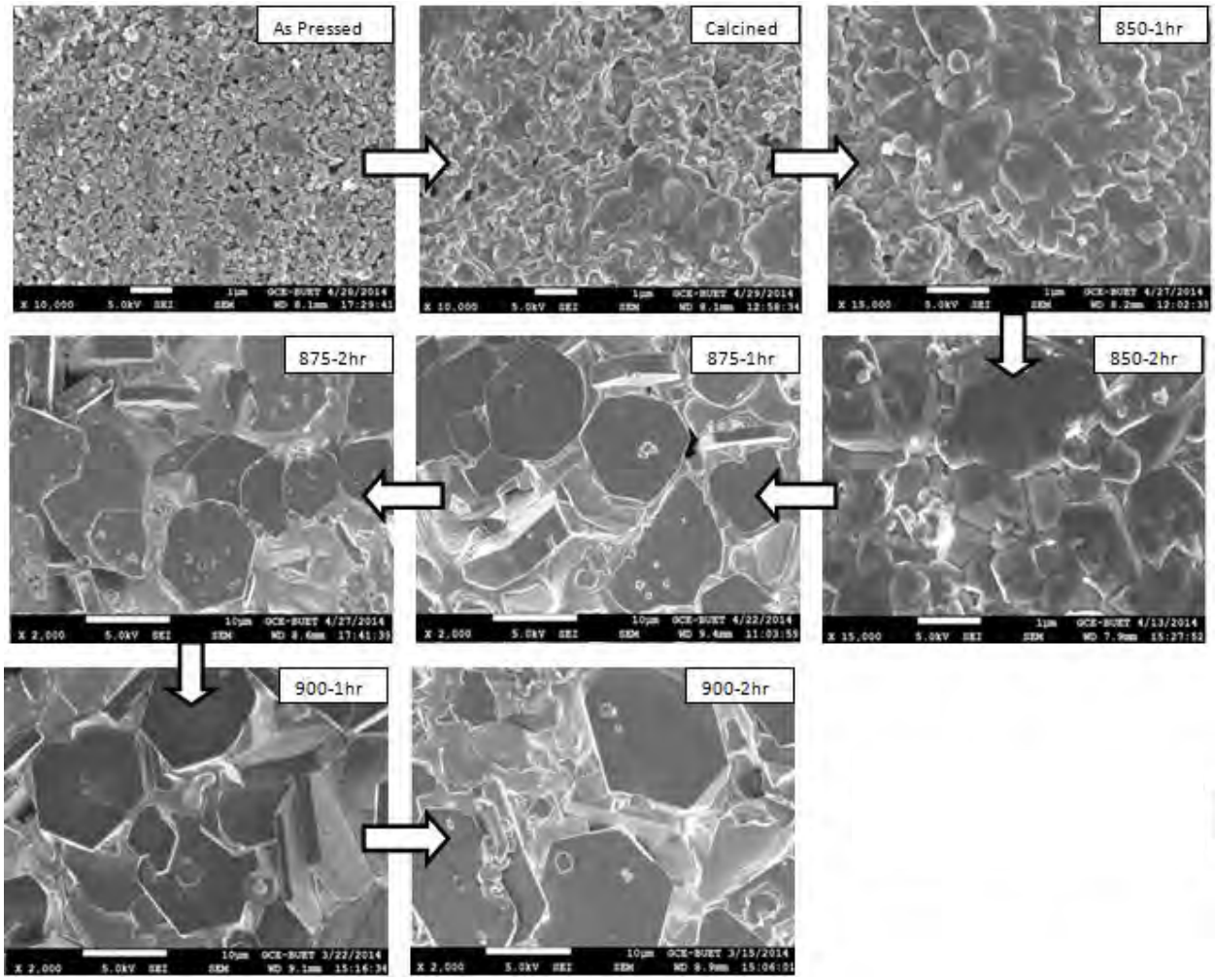

Figure 4.11: Microstructure development from as pressed to sintered condition of $Bi_{0.9}Ba_{0.1}FeO_3$ samples sintered using cycle-1.

As can be seen from Figure 4.11, the porosity of the as pressed $Bi_{0.9}Ba_{0.1}FeO_3$ sample decreased gradually with calcination and increasing sintering temperature. An optimum between % TD (> 95%) and average grain size (0.8-0.9 μm) was attained for this sample when sintered at 850°C for 2 hours. Thereafter the average grain size of $Bi_{0.9}Ba_{0.1}FeO_3$ samples increased rapidly from 0.8 μm to about 10 μm as the temperature was raised from 850°C to 900°C. However, above 850°C, a clear indication of liquification can be observed in the structure, which manifests that the sintering temperature is excessive for this composition. This liquefied structure will have a detrimental effect on the properties and so it is not preferable.

According to literature pure BFO has excessive grain growth tendency. From the microstructures shown in Figure 4.11 it is clear that, for $Bi_{0.9}Ba_{0.1}FeO_3$ sample doping of 0.1 mole fraction of Ba was not sufficient to control grain growth of BFO.

Figures 4.12 shows the gradual increase in % TD by increase in sintering temperature and effect of doping on grain size for $Bi_{0.8}Ba_{0.2}FeO_3$ samples sintered using cycle-1. At 850°C the %TD for these samples was extremely poor (below 70%) due to the presence of porosity throughout the structure as can be seen from the figure. This clearly indicated that the provided temperature and holding time was not sufficient to achieve the desired densification for these samples. At 875°C the %TD for these samples increased to about 80% for both 1 and 2 hours of holding time with clear indication of starting of grain coalescence in the microstructure (see Figure 4.12). At 900°C, although the porosity has significantly decreased (%TD > 93%) compare to the samples sintered at lower temperatures but the average grain size is still not sufficient. Maximum average grain size of 0.65-0.75μm was attained for $Bi_{0.8}Ba_{0.2}FeO_3$ samples when sintered at 900°C for 2 hours. This average grain size is still not adequate for optimization of properties.

From the microstructures shown in Figure 4.12 for $Bi_{0.8}Ba_{0.2}FeO_3$ samples, it is clear that addition of 0.2 mole fraction of Ba surely has an effect on grain growth and densification process. Ba acts as grain growth inhibitor, inhibits grain growth by pinning effect and thereby hampers the densification process. So, even 2 hours of holding at 900°C was not sufficient for proper grain growth for this composition when using cycle-1. However it should be mentioned

that, 900°C being high enough temperature causes distortion in the samples which may have a detrimental effect on properties.

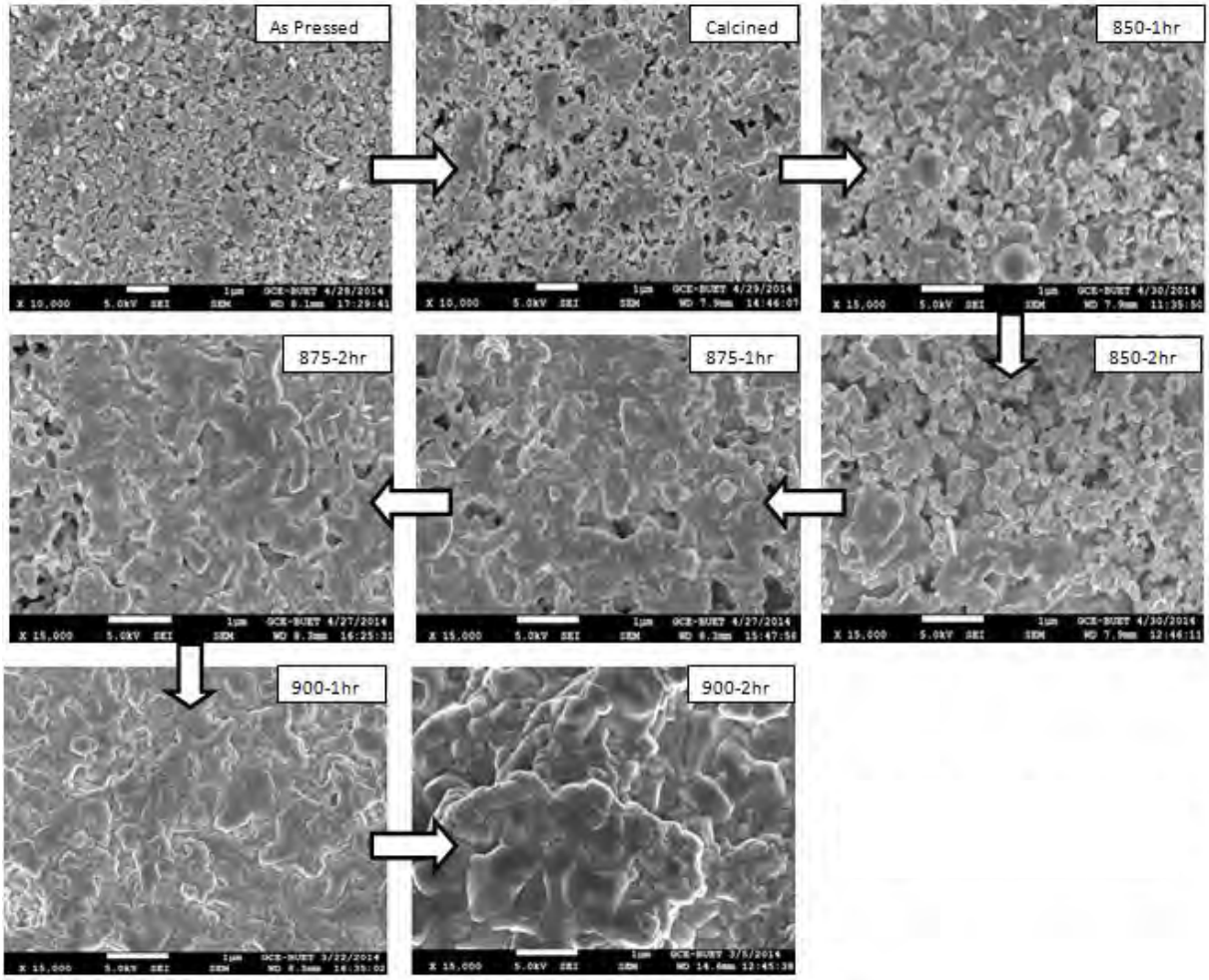

Figure 4.12: Microstructure development from as pressed to sintered condition of $Bi_{0.8}Ba_{0.2}FeO_3$ samples sintered using cycle-1.

Figure 4.13 shows the microstructural development of $Bi_{0.7}Ba_{0.3}FeO_3$ samples with increasing sintering temperature from the as pressed condition. Comparing with Figure 4.11 and 4.12, it is obvious that the porosity level has increased in the microstructures for these samples due to addition of more Ba. From Figure 4.13, it is evident that sintering temperature of 850°C is inadequate for pore removal and attainment of satisfactory %TD for this composition. The %TD is below 70% at this sintering temperature. However, the extent of densification has improved and the porosity level has decreased with increase in sintering temperature up to 900°C due to

grain coalescence. Nevertheless, the average grain size of the samples is too small with no indication of proper grain growth. The average grain size increased from 0.2 μm at 850°C to a maximum of 0.65 μm only when sintered at 900°C for 2 hours of holding time. This clearly indicates the grain growth inhibiting effect of Ba addition which has also been reported previously [30]. Ba stays at grain boundary and controls grain growth by pinning effect. The microstructure clearly indicates the requirement of a longer exposure time at high temperature for proper grain growth for these samples. Longer time at high temperature would certainly reduce the grain growth inhibiting effect of Ba.

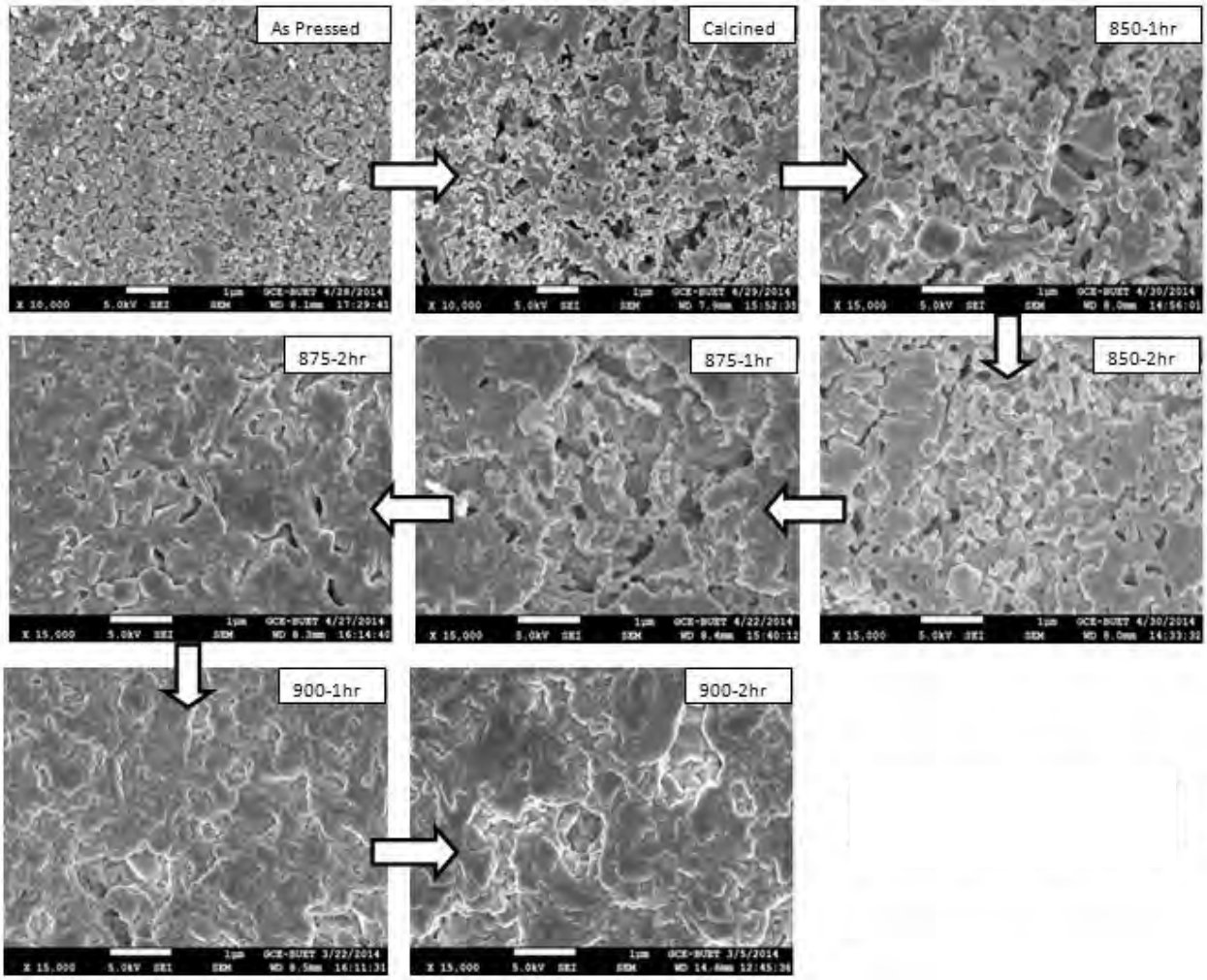

Figure 4.13: Microstructure development from as pressed to sintered condition of $Bi_{0.7}Ba_{0.3}FeO_3$ samples sintered using cycle-1.

Figure 4.14 shows the similar microstructural development for $Bi_{0.7}Ba_{0.3}Fe_{0.9}Ti_{0.1}O_3$ samples sintered using cycle-1 in the temperature range 850-900°C. The microstructures clearly indicated that the provided temperature and holding time was not sufficient to achieve the desired densification and average grain size for these samples. Ti along with Ba inhibits grain growth and densification in these samples. So, evidently, the microstructure of these samples contained lots of visible pores, as shown in the figure below. The maximum %TD (93-94%) and average grain size (0.45-0.55 µm) was attained for this sample when sintered at 900°C for 2 hours, which is not sufficient for optimization of dielectric and magnetic properties. Nevertheless, as stated previously, distortion of the samples at 900°C is also a concern for optimization of the properties.

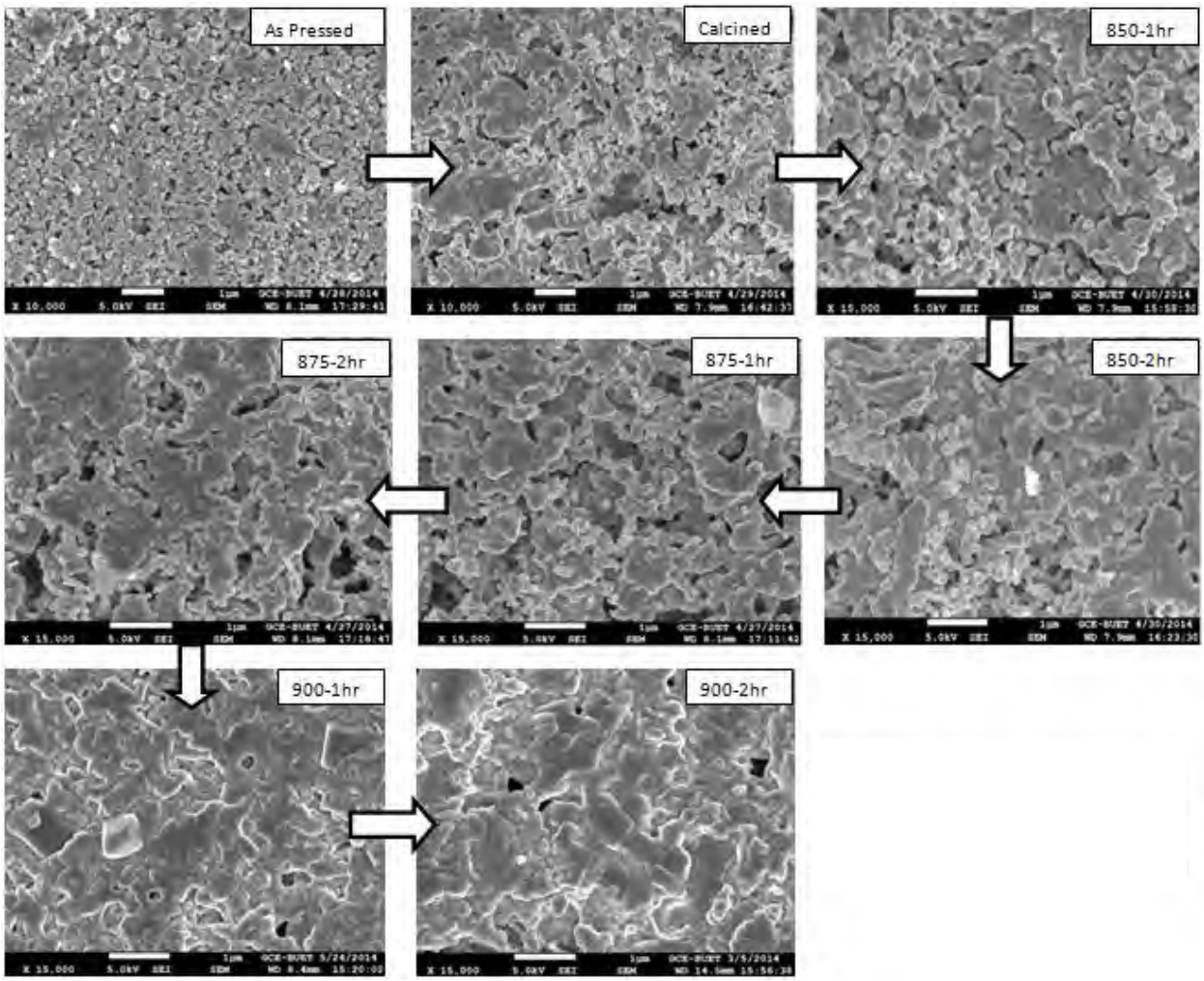

Figure 4.14: Microstructure development from as pressed to sintered condition of $Bi_{0.7}Ba_{0.3}Fe_{0.9}Ti_{0.1}O_3$ samples sintered using cycle-1.

So, the microstructures of $Bi_{1-x}Ba_xFe_{1-y}Ti_yO_3$ samples sintered in the temperature range 850-900^oC using cycle-1 for both 1 and 2 hours of holding time confirms that, increased doping concentration suppresses the grain growth during sintering thus resulting in poorer densification. This can also be explained using vacancy mechanism. Previous studies suggested that the grain growth depends upon the concentration of oxygen vacancies [30] and diffusion rate of the ions.

It is well known that in $BiFeO_3$ perovskites, the oxygen vacancies (Vo^{2+}) could be formed in the process of sintering due to the escape of oxygen from the lattice [81]. Vo^{2+} comes mainly from Bi volatility and the transition from Fe^{3+} to Fe^{2+} which can be described by equations (4.6) and (4.7): [82]

$$2Fe^{3+} + O^{2-} \rightarrow 2Fe^{2+} + Vo^{2+} + 0.5O_2 \quad (4.6)$$

$$2Bi^{3+} + 3O^{2-} \rightarrow 2V_{Bi}^{3-} + 3Vo^{2+} + Bi_2O_3 \quad (4.7)$$

In $Bi_{0.9}Ba_{0.1}FeO_3$ samples the added Ba was not sufficient to reduce these oxygen vacancies of pure $BiFeO_3$. Thus, the large number of oxygen vacancies in these samples makes it easy for the ions to diffuse, resulting in very large grains. This phenomenon was suppressed with increasing doping concentration by the occupation of certain probable evaporated Bi sites by Ba ions at certain doping level. So, the decrease in average grain size of $Bi_{0.8}Ba_{0.2}FeO_3$ samples might be interpreted in terms of the suppression of the oxygen vacancy concentration. The occupation of vacancies slows oxygen ion motion, consequently reducing the grain growth and resulting in smaller grains. Although, as stated previously in section 4.1, on further Ba doping oxygen vacancies were generated for charge neutralization in $Bi_{0.7}Ba_{0.3}FeO_3$ samples, but grain growth was limited due to substitution of Bi atoms having smaller ionic radius with larger ionic radius Ba atoms. The larger atoms confine the space for oxygen ion motion and thereby hinder grain growth and densification. However, in $Bi_{0.7}Ba_{0.}Fe_{0.9}Ti_{0.1}O_3$ samples the oxygen vacancy created by the excess Ba doping were eliminated by B-site doping with Ti^{4+} which demotivate oxygen ion motion in these samples, consequently controlling grain growth.

After sintering of $Bi_{1-x}Ba_xFe_{1-y}Ti_yO_3$ samples using cycle-1 some conclusions were drawn. The optimum sintering zone should be different for each composition due to effect of doping concentration on grain growth and densification. For $Bi_{0.9}Ba_{0.1}FeO_3$ samples, the optimum sintering temperature should not be above 850°C as liquification starts in the structure due to excessive heating. For $Bi_{0.8}Ba_{0.2}FeO_3$, $Bi_{0.7}Ba_{0.3}FeO_3$ and $Bi_{0.7}Ba_{0.3}Fe_{0.9}Ti_{0.1}O_3$ samples, optimum sintering temperature should be below 900°C as the high sintering temperature resulted in distortion in these samples. Also, more time is required at high temperatures for these compositions for proper grain growth and densification.

However, to overcome the shortcomings of cycle-1, the $Bi_{1-x}Ba_xFe_{1-y}Ti_yO_3$ samples were next sintered using cycle-2 (Figure 4.2) in the temperature range 850-875°C. In order to provide sufficient time for proper densification and grain growth at high temperature in cycle-2, the sintering rate above the calcinations temperature (800°C) was reduced from 3°C/min to 1°C/min and the cooling rate was decreased from 5°C/min to 3°C/min. Optimization of microstructure for all the compositions was achieved under this sintering cycle.

Figure 4.15 shows the microstructure of the $Bi_{1-x}Ba_xFe_{1-y}Ti_yO_3$ ceramics sintered at 850°C for 2 hours using cycle-2. For $Bi_{0.9}Ba_{0.1}FeO_3$ ceramics sintering was adequate and resulted in % TD above 95% and average grain size ~1.0-1.1 μm. **So, the optimum microstructure for $Bi_{0.9}Ba_{0.1}FeO_3$ samples was achieved when sintered at 850°C for 2 hours using cycle-2 (SAMPLE ID: T1)**. %TD was good even for $Bi_{0.8}Ba_{0.2}FeO_3$ samples but it was associated with extremely fine grain size (below 0.4 μm). In $Bi_{0.7}Ba_{0.3}FeO_3$ and $Bi_{0.7}Ba_{0.3}Fe_{0.9}Ti_{0.1}O_3$ samples, extent of densification decreased dramatically and resulted in porous structures. The average grain size of these samples was also below satisfactory (below 0.4 μm).

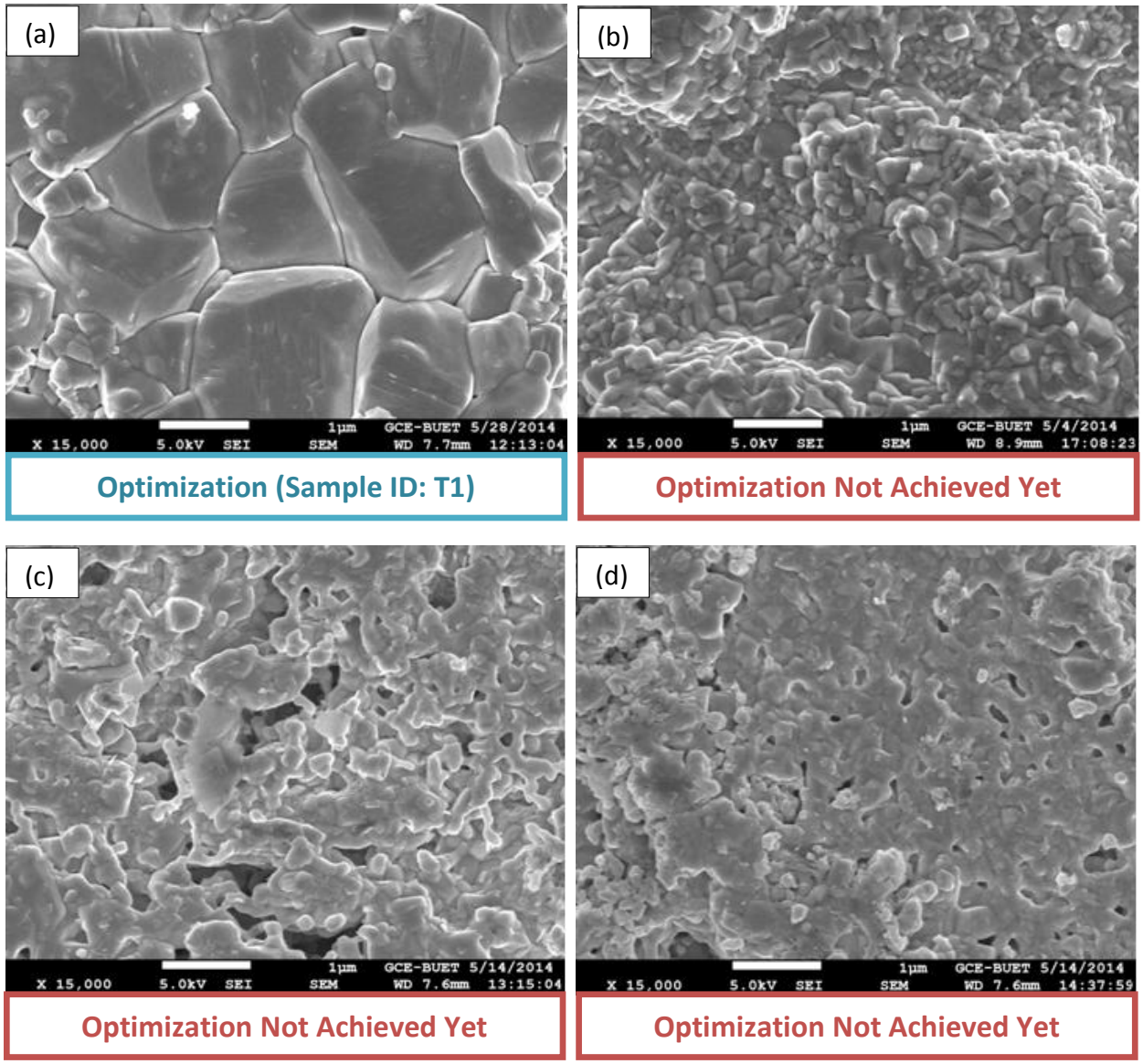

Figure 4.15: FESEM micrograph of $Bi_{1-x}Ba_xFe_{1-y}Ti_yO_3$ samples sintered at 850°C for 2 hours showing variation of <grain size> and %TD with doping concentration.

(a) x= 0.1, y= 0.0; <Grain size> = 1.0-1.1µm; % TD = >95.0 (b) x= 0.2, y= 0.0; <Grain size> = < 0.4 µm; % TD = 90-93
(c) x= 0.3, y= 0.0; <Grain size> = < 0.4 µm; % TD = 80-82 (d) x= 0.3, y= 0.1; <Grain size> = < 0.4 µm; % TD = 80-82

Keeping other parameters constant, the samples were next sintered at 850°C for a holding time of 4 hours. The %TD attained by $Bi_{0.9}Ba_{0.1}FeO_3$ ceramics was still high when the holding time was increased to 4 hours but this was accompanied with rapid increase in average grain size of the samples to 2.0-2.3 µm with increasing temperature as shown in Figure 4.16 (a). Furthermore,

increasing the holding to 4 hours resulted in better densification for the $Bi_{0.8}Ba_{0.2}FeO_3$, $Bi_{0.7}Ba_{0.3}FeO_3$ and $Bi_{0.7}Ba_{0.3}Fe_{0.9}Ti_{0.1}O_3$ samples compare to 2 hours of holding at 850°C but again the average grain size of these samples was extremely small with presence of small amount of porosity.

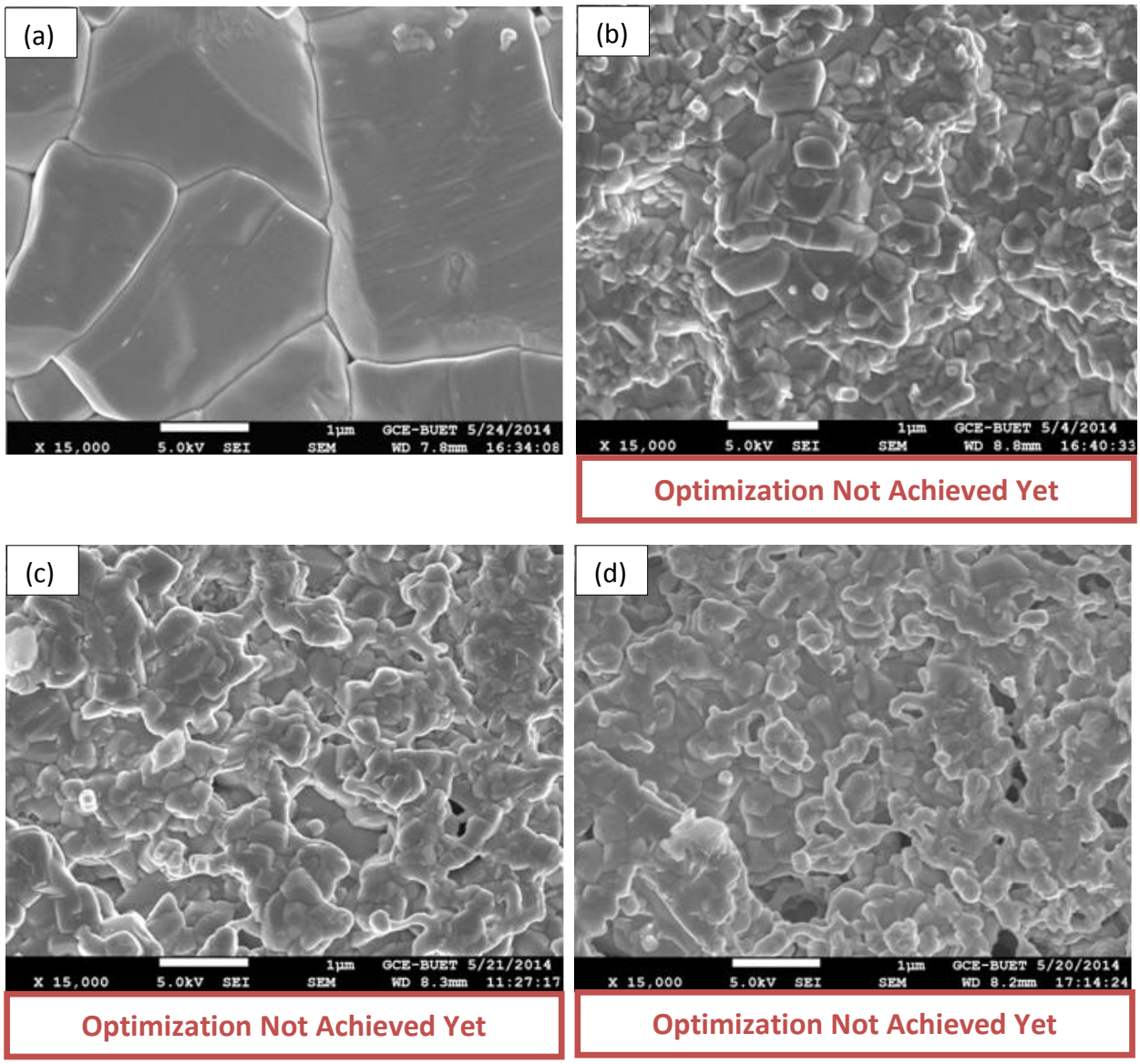

Figure 4.16: FESEM micrograph of $Bi_{1-x}Ba_xFe_{1-y}Ti_yO_3$ samples sintered at 850°C for 4 hours showing variation of <grain size> and %TD with doping concentration.

(a) x= 0.1, y= 0.0; <Grain size> = 2.0-2.3 µm; % TD = >95.0 (b) x= 0.2, y= 0.0; <Grain size> = < 0.5 µm; % TD = 90-93
(c) x= 0.3, y= 0.0; <Grain size> = < 0.5 µm; % TD = 85-90 (d) x= 0.3, y= 0.1; <Grain size> = < 0.4 µm; % TD = 85-90

From the Figure 4.16, it is clearly evident that sintering at 850°C for $Bi_{0.8}Ba_{0.2}FeO_3$, $Bi_{0.7}Ba_{0.3}FeO_3$ and $Bi_{0.7}Ba_{0.3}Fe_{0.9}Ti_{0.1}O_3$ samples were insufficient to offer sufficient energy for proper coalescence of grains hence resulted in inadequate grain growth. The effect of holding time at sintering temperature is linear but the effect of sintering temperature is exponential on grain size. So, the results shown till now clearly indicates the necessity for even higher sintering temperature in order to obtain optimization between average grain size and %TD, especially for $Bi_{0.8}Ba_{0.2}FeO_3$, $Bi_{0.7}Ba_{0.3}FeO_3$ and $Bi_{0.7}Ba_{0.3}Fe_{0.9}Ti_{0.1}O_3$ samples where the solute drag or pinning effect of Ba and Ti inhibits the grain growth process. So, this time the sintering temperature was increased to 875°C keeping other parameters constant.

Figure 4.17 reveals that after 2 hours of holding at 875°C, the average grain size of the $Bi_{0.9}Ba_{0.1}FeO_3$ samples increased excessively to 7-8 μm and this was accompanied with melting in the structure as shown in Figure 4.17 (a). This excessive grain growth together with liquefied structure is detrimental for multiferroic properties. **However, increasing the sintering temperature to 875°C resulted in optimization for $Bi_{0.8}Ba_{0.2}FeO_3$ samples (SAMPLE ID: T2).** %TD > 95% and average grain size of 0.95-1.0μm was attained by $Bi_{0.8}Ba_{0.2}FeO_3$ samples when sintered at 875°C for 2 hours. Although porosity was almost completely removed for $Bi_{0.7}Ba_{0.3}FeO_3$ and $Bi_{0.7}Ba_{0.3}Fe_{0.9}Ti_{0.1}O_3$ samples but their average grain size was still below 0.8μm. so, optimization was yet to be achieved for $Bi_{0.7}Ba_{0.3}FeO_3$ and $Bi_{0.7}Ba_{0.3}Fe_{0.9}Ti_{0.1}O_3$ samples. Further grain growth was required for these samples for optimization of microstructure and for better ferroelectric properties as average grain size of about ~ 1 μm is normally required to obtain good values of permittivity in ceramics.

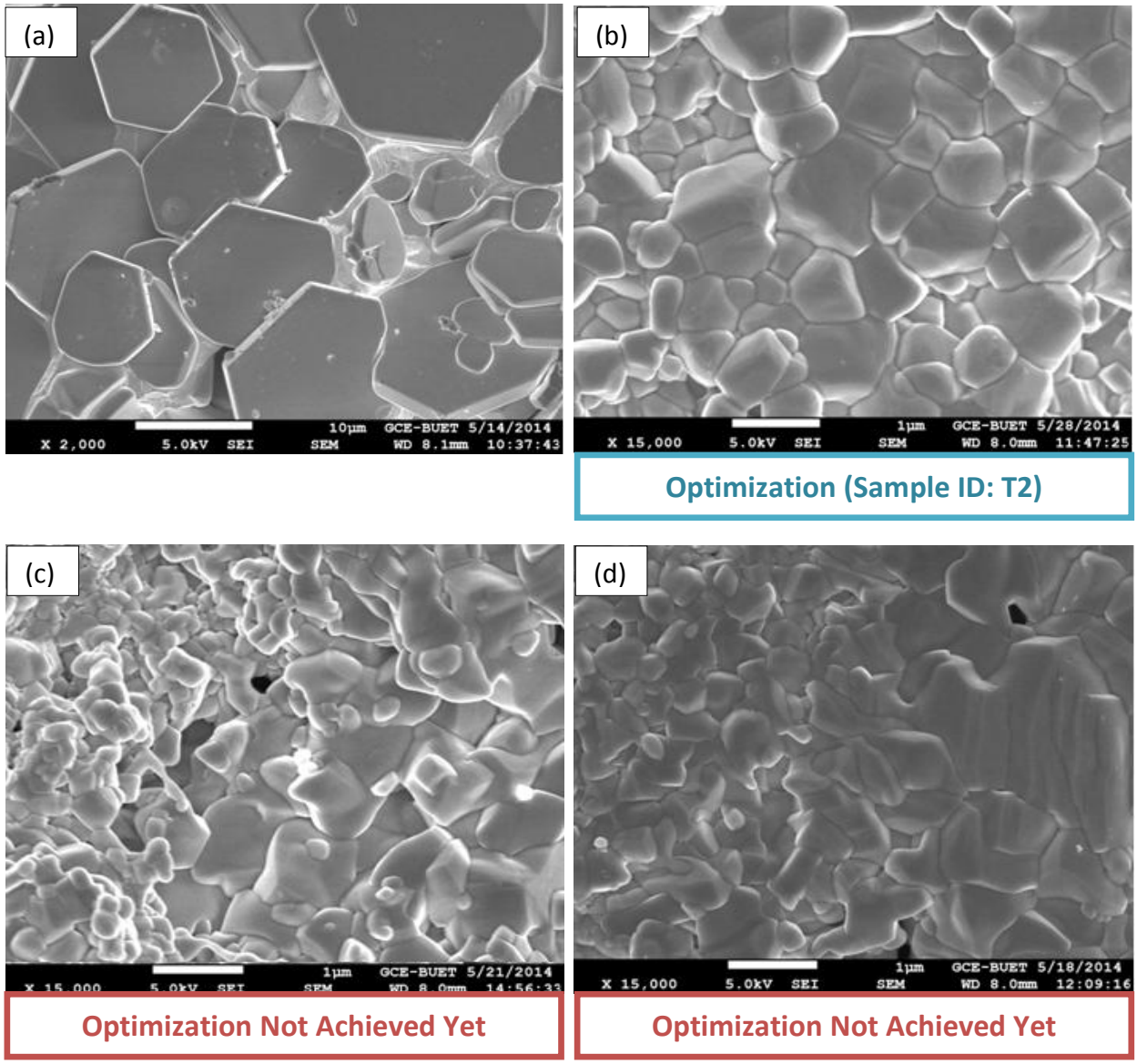

Figure 4.17: FESEM micrograph of $Bi_{1-x}Ba_xFe_{1-y}Ti_yO_3$ samples sintered at 875°C for 2 hours showing variation of <grain size> and %TD with doping concentration.

(a) x= 0.1, y= 0.0; <Grain size> = 6-7 µm; % TD = >95.0 (b) x= 0.2, y= 0.0; <Grain size> = 0.95-1.0 µm; % TD = >95.0
(c) x= 0.3, y= 0.0; <Grain size> = 0.65-0.75µm; % TD = 90-93 (d) x= 0.3, y= 0.1; <Grain size> = 0.55-0.65µm; % TD = 90-93

Next, the microstructure of the $Bi_{1-x}Ba_xFe_{1-y}Ti_yO_3$ ceramics sintered at 875°C for 4 hours are shown in Figure 4.18. As can be seen in the figure, for $Bi_{0.9}Ba_{0.1}FeO_3$ samples excessive grain growth with liquification in the structure continues at 4 hours of holding time. Excessive grain growth to 1.5-1.7µm was also attained by $Bi_{0.8}Ba_{0.2}FeO_3$ samples when sintered at 875°C for 4 hours, which is detrimental to it's properties as mentioned previously. **However, optimization**

was achieved for $Bi_{0.7}Ba_{0.3}FeO_3$ samples by sintering at 875°C for 4 hours using cycle-2 (SAMPLE ID: T3), resulting in %TD > 95% and average grain size of 0.95-1.0 µm. Nevertheless, optimization for $Bi_{0.7}Ba_{0.3}Fe_{0.9}Ti_{0.1}O_3$ was yet to be achieved, requiring for more exposure at 875°C for necessary grain growth.

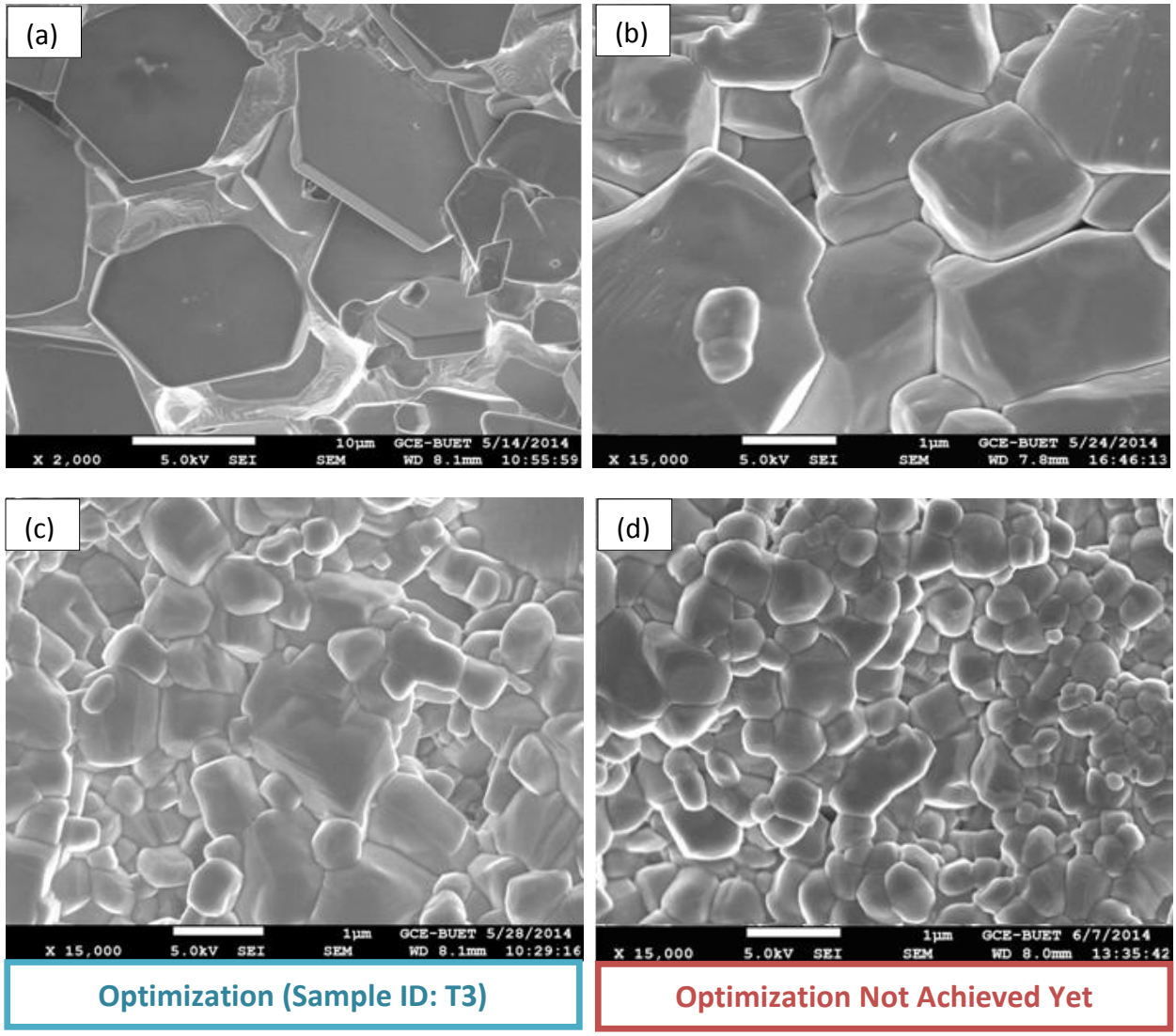

Figure 4.18: FESEM micrograph of $Bi_{1-x}Ba_xFe_{1-y}Ti_yO_3$ samples sintered at 875°C for 4 hours showing variation of <grain size> and %TD with doping concentration.

(a) x= 0.1, y= 0.0; <Grain size> = 6-7 µm; % TD = >95.0 (b) x= 0.2, y= 0.0; <Grain size> = 1.5-1.7 µm; % TD = >95.0
(c) x= 0.3, y= 0.0; <Grain size> = 0.95-1.0µm; % TD = >95.0 (d) x= 0.3, y= 0.1; <Grain size> = 0.7-0.8µm; % TD = >95.0

Figure 4.19 shows the microstructure of the $Bi_{1-x}Ba_xFe_{1-y}Ti_yO_3$ ceramics sintered at 875°C for 6 hours. **It is apparent that, optimization was attained by $Bi_{0.7}Ba_{0.3}Fe_{0.9}Ti_{0.1}O_3$ samples finally**

when the holding time at 875°C was increased to 6 hours, resulting %TD > 95% and average grain size of 1.0-1.05µm (SAMPLE ID: T4). The excellent %TD attained by $Bi_{0.8}Ba_{0.2}FeO_3$ and $Bi_{0.7}Ba_{0.3}FeO_3$ samples at sintering temperatures of 875°C for 6 hours holding time was accompanied by excessive grain growth which may have detrimental effects on the ferroelectric properties due to shortening of the grain boundary length that decreases resistance to leakage current. Moreover, similar to the previous sintering conditions at 875°C, liquification with excessive grain growth continues for $Bi_{0.9}Ba_{0.1}FeO_3$ samples at 6 hours holding time.

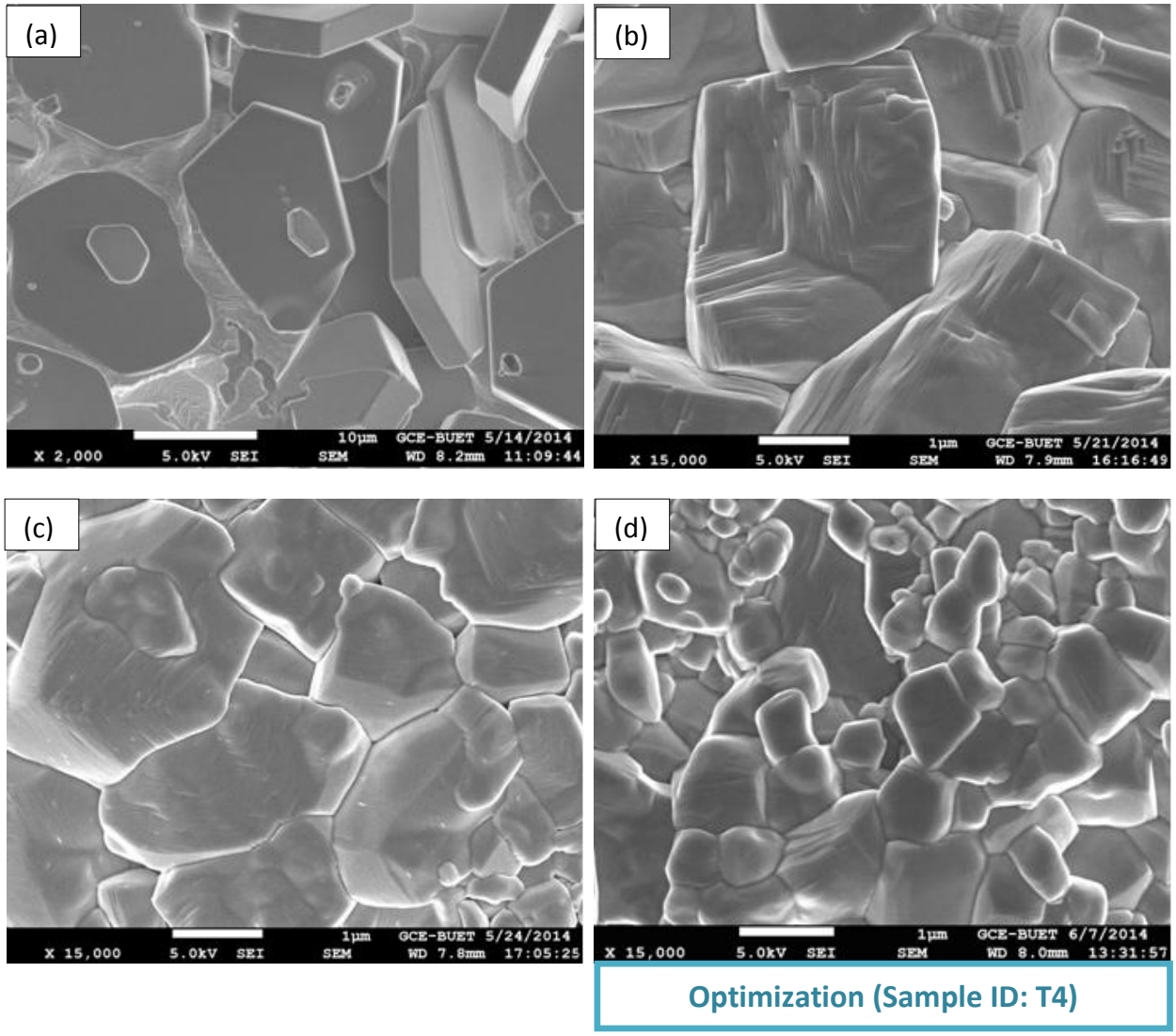

Figure 4.19: FESEM micrograph of $Bi_{1-x}Ba_xFe_{1-y}Ti_yO_3$ samples sintered at 875°C for 6 hours showing variation of <grain size> and %TD with doping concentration.

(a) x= 0.1, y= 0.0; <Grain size> = 8 µm; % TD = >95.0 (b) x= 0.2, y= 0.0; <Grain size> = 1.8-2.0 µm; % TD = >95.0
(c) x= 0.3, y= 0.0; <Grain size> = 1.5-1.7µm; % TD = >95.0 (d) x= 0.3, y= 0.1; <Grain size> = 1.0-1.05µm; % TD = >95.0

The results shown till now reveal that, optimization of microstructure for all compositions of $Bi_{1-x}Ba_xFe_{1-y}Ti_yO_3$ ceramics were achieved when sintered under cycle 2. Optimization of microstructure being achieved for all compositions by trial and error method, next the properties of the optimized compositions (T1, T2, T3 and T4) were measured to find out the effect of Ba and Ti doping on the multiferroic properties of $BiFeO_3$.

4.4 XRD analysis

Figure 4.20 shows the XRD patterns at room temperature of $Bi_{1-x}Ba_xFe_{1-y}Ti_yO_3$ (x = 0.1, y = 0.0; x = 0.2, y = 0.0; x = 0.3, y = 0.0; and x = 0.3, y = 0.1) samples having optimum microstructure (Sample ID: T1, T2, T3 and T4). All the samples show a single phase perovskite structure which implies that the doping does not lower the stabilization of $BiFeO_3$. The figure shows similarity in the intensity, number and position of the planes to that of original rhombohedral R3c structure planes (designated by green lines at the bottom) of pure $BiFeO_3$.

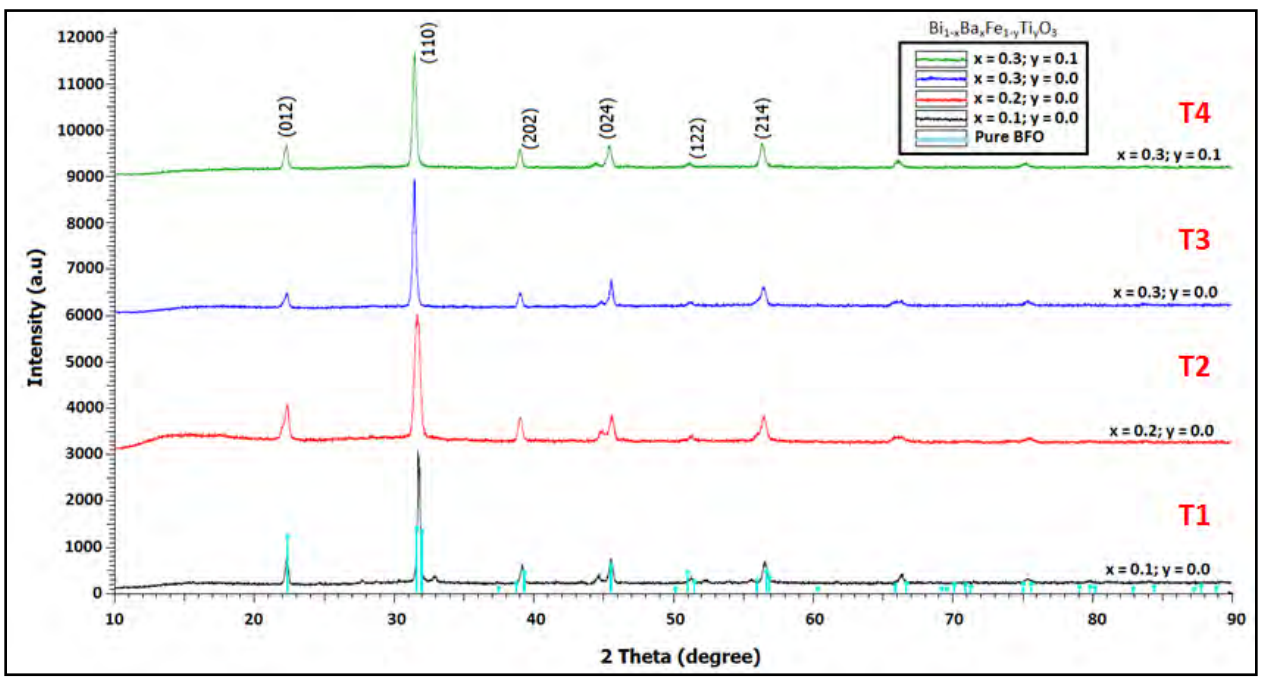

Figure 4.20: XRD patterns at room temperature of $Bi_{1-x}Ba_xFe_{1-y}Ti_yO_3$ (x = 0.1, y = 0.0; x = 0.2, y = 0.0; x = 0.3, y = 0.0; and x = 0.3, y = 0.1) samples having optimum microstructure.

It is known that the room temperature phase of pure BFO is a rhombohedrally distorted perovskite structure described by space group R3c. Rhombohedral cell is very close to the cubic one (angle α in the rhombohedral cell is about 89.4^o). In this structure, cations are displaced from their centrosymmetric position along the pseudocubic [1 1 1] c axes. The unit cell can also be described in a hexagonal frame of reference with hexagonal c-axis parallel to the diagonals of the perovskite cube. Therefore, the miller indices (hkl) of diffraction peaks in figure 4.20 are referred to as hexagonal axes rather than rhombohedral axes [23].

Figure 4.20 also reveals a shift in the peak positions towards left with the increase of doping concentration, indicating increment in the lattice parameter. Thus Ba substitution leads to an increase in the unit cell volume since the ionic radius of Ba (1.5 ˚A) is larger than that of Bi (1.17 ˚A). However, separation between diffraction peaks is observed at 2Θ ~32° and 46° for all compositions which implies that the original rhombohedral of $BiFeO_3$ structure may have distorted to a tetragonal/pseudo-tetragonal structure. This effect of peak splitting has also been reported for La or Nd doped bulk BiFeO3 in earlier studies [84].

The distortion of the original structure of BFO with increasing doping concentration as reported by the XRD analysis is particularly important to improve ferromagnetic properties of BFO.

4.5 Dielectric property measurement

Fine grained and dense samples exhibit good dielectric properties. Excessive grain growth can deteriorate dielectric properties. It is a well known fact that decrease in the grain size increases the grain boundary region and hence, increases the resistivity of the material resulting in good dielectric property [17, 30]. From literature it is evident that usually microstructures having ~1μm average grain size provide good dielectric properties [78]. However, too fine a grain size has an adverse effect on dielectric property due to the increase in pinning of domain walls. This pinning effect hinders the orientation of the domains by the applied field reducing the dielectric property. Thus, the resistivity or leakage current of $BiFeO_3$ system is significantly affected by it‘s microstructure, i.e. size of the grains and length of grain boundaries and density of the

material. So, attainment of an optimum between average grain size and %TD is the prerequisite for excellent dielectric properties. That is why developing the optimum microstructure was an important task in this thesis. As discussed previously, optimization of microstructure for all $Bi_{1-x}Ba_xFe_{1-y}Ti_yO_3$ (x = 0.1, y = 0.0; x = 0.2, y = 0.0; x = 0.3, y = 0.0; and x = 0.3, y = 0.1) samples were obtained when sintered using cycle-2 in the temperature zone 850-875^oC. All the four compositions having optimum microstructure, their dielectric constant were measured and compared to find the effect of doping concentration on dielectric properties of BFO. The optimized sintering conditions of the four compositions and their corresponding dielectric constant at room temperature have been reported in Table 4.3.

Table 4.3: Dielectric constant of $Bi_{1-x}Ba_xFe_{1-y}Ti_yO_3$ samples having optimum microstructure.

Sample ID	Composition	Sintering Temperature (^oC)	Holding Time (hours)	Percent Theoretical Density (%TD)	Grain Size µm	Dielectric Constant k (at 1 KHz)
T1	**$Bi_{0.9}Ba_{0.1}FeO_3$**	850	2	>95	1.0-1.1	**630**
T2	**$Bi_{0.8}Ba_{0.2}FeO_3$**	875	2	>95	0.95-1.0	**2860**
T3	**$Bi_{0.7}Ba_{0.3}FeO_3$**	875	4	>95	0.95-1.0	**980**
T4	**$Bi_{0.7}Ba_{0.3}Fe_{0.9}Ti_{0.1}O_3$**	875	6	>95	1.0-1.05	**2885**

These effects of doping concentration on the dielectric property of BFO have been shown graphically in Figure 4.21.

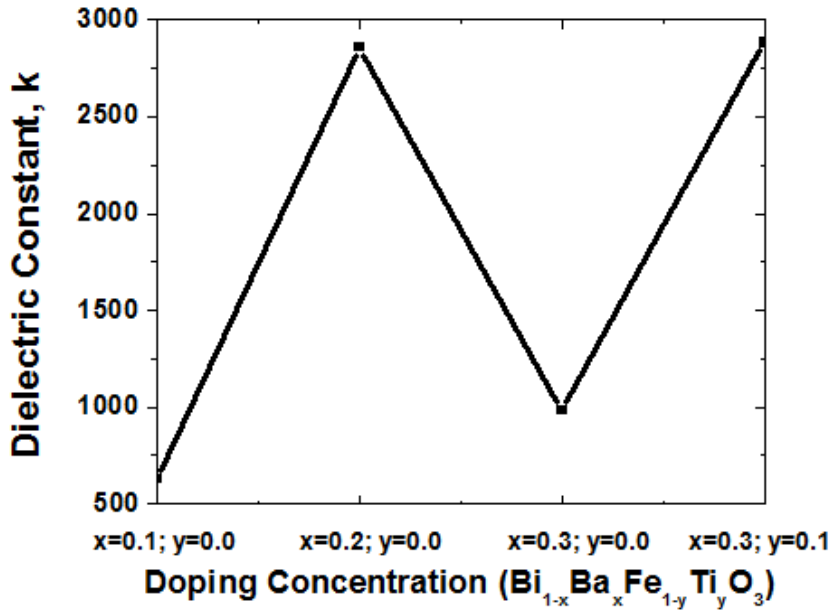

Figure 4.21: Variation of dielectric constant with doping concentration of $Bi_{1-x}Ba_xFe_{1-y}Ti_yO_3$ (x = 0.1, y = 0.0; x = 0.2, y = 0.0; x = 0.3, y = 0.0; and x = 0.3, y = 0.1) samples having optimum microstructure.

The dielectric constant value of pure BFO varies between 50-300 at the frequencies typically accessible by impedance analyzer (100 KHz to 1 MHz) depending on surface morphology, orientation and frequency range. The reduced dielectric property in pure BFO can be attributed to two possible factors: First is the concentration of oxygen vacancies [84] produced due to highly volatile nature of Bi (Pure $BiFeO_3$ should be written in the form $Bi_{1-\delta}FeO_{3-3\delta/2}$ due to this unknown number of vacant B-sites). Second is the multiple oxidation states of Fe ions (Fe^{2+} and Fe^{3+}) [84, 86]. This behavior of Fe contributes to the conduction at high electric field by the transfer of the electrons from Fe^{2+} to Fe^{3+}, that is, virtual hopping of the Fe^{2+} takes place in the vicinity of high electric field. Thus, a high concentration of Fe^{2+} ions in the material gives rise to high leakage current. Addition of Ba significantly reduces the oxygen vacancy related defects (leakage current) by occupying evaporated Bi sites and increases the electrical resistivity of BFO by controlling grain size, thus allowing high dielectric constant to be determined at room temperature. That is why the value of dielectric constant was found to increase sharply for $Bi_{1-x}Ba_xFe_{1-y}Ti_yO_3$ with increasing Ba addition from 630 for sample T1(x=0.1, y=0.0) to 2860 for sample T2 (x=0.2, y=0.0) at 1 kHz frequency (Figure 4.21). However, a sharp decrease in dielectric constant value to 980 was seen with further Ba addition for T3 sample (x=0.3, y=0.0).

This decrease in dielectric constant above 0.2 mole fraction Ba doping has been reported previously [6, 27]. All the vacant Bi-sites of pure BFO formed during processing are assumed to be filled up by 0.2 mole fraction Ba doping according to literature, resulting in minimum oxygen vacancies in $Bi_{0.8}Ba_{0.2}FeO_3$ (Sample T2). So, addition of extra 0.1 mole fraction Ba^{2+} in $Bi_{0.7}Ba_{0.3}FeO_3$ (Sample T3) by replacing 0.1 mole fraction Bi^{3+} atoms would generate 0.05 mole fraction oxygen vacancies (As, 1 mole Bi^{3+} associates with 1.5 mole O^{2-} whereas 1 mole Ba^{2+} associates with only 1 mole O^{2-}). To reduce these oxygen vacancies, 0.1 mole fraction Ti^{4+} in $Bi_{0.7}Ba_{0.3}Fe_{0.9}Ti_{0.1}O_3$ (T4) was added replacing Fe^{3+} at B-site which would reduce this 0.05 mole fraction oxygen vacancies. Because, 1 mole Ti^{4+} associates with 2 mole O^{2-} whereas 1 mole Fe associates with only 1.5 mole O^{2-}.

So, we can summarize that, the dielectric constant value decreased for T3 sample due to excessive Ba doping [27, 30]. To eliminate the oxygen vacancies created in T3 sample Fe^{3+} site of BFO was codoped with higher charge Ti^{4+} in T4 sample. That is why excellent dielectric constant (2885 at 1 KHz) was obtained for the T4 sample due to nullification of oxygen vacancies and thereby reduction of leakage current in this sample.

Figure 4.22 shows the variation of dielectric constant (k) with temperature at different frequencies of the $Bi_{1-x}Ba_xFe_{1-y}Ti_yO_3$ (x = 0.1, y = 0.0; x = 0.2, y = 0.0; x = 0.3, y = 0.0; and x = 0.3, y = 0.1) samples having optimum microstructure. The dielectric constant in these samples mainly occurs due to ionic polarization of A-site atoms. However, at higher temperatures a remarkable increase in k-value occurs in $Bi_{0.9}Ba_{0.1}FeO_3$ and $Bi_{0.7}Ba_{0.3}FeO_3$ samples due to space charge polarization, as can be seen in 4.22 [88]. The space charges are suggested to originate from V_O^{2+},V_{Bi}^{3-}, etc. As discussed previously, the oxygen deficiency is a problem with these samples. So, there is always some contribution of space charge polarization due to oxygen ion vacancies in these samples over the entire temperature range. But at higher temperature this effect becomes more prominent due to a thermally activated process, in which the k-value starts increasing after a certain temperature. So, the rise in the value of the dielectric constant beyond this temperature range may be due to the space charge polarization [87-89]. However, in $Bi_{0.8}Ba_{0.2}FeO_3$ and $Bi_{0.7}Ba_{0.3}Fe_{0.9}Ti_{0.1}O_3$ samples such behaviour is not so remarkable. Therefore, the dielectric constant of these samples remains considerably stable over the entire temperature

range. This indicates that the oxygen vacancy in these samples was controlled by doping and thereby improved their dielectric property.

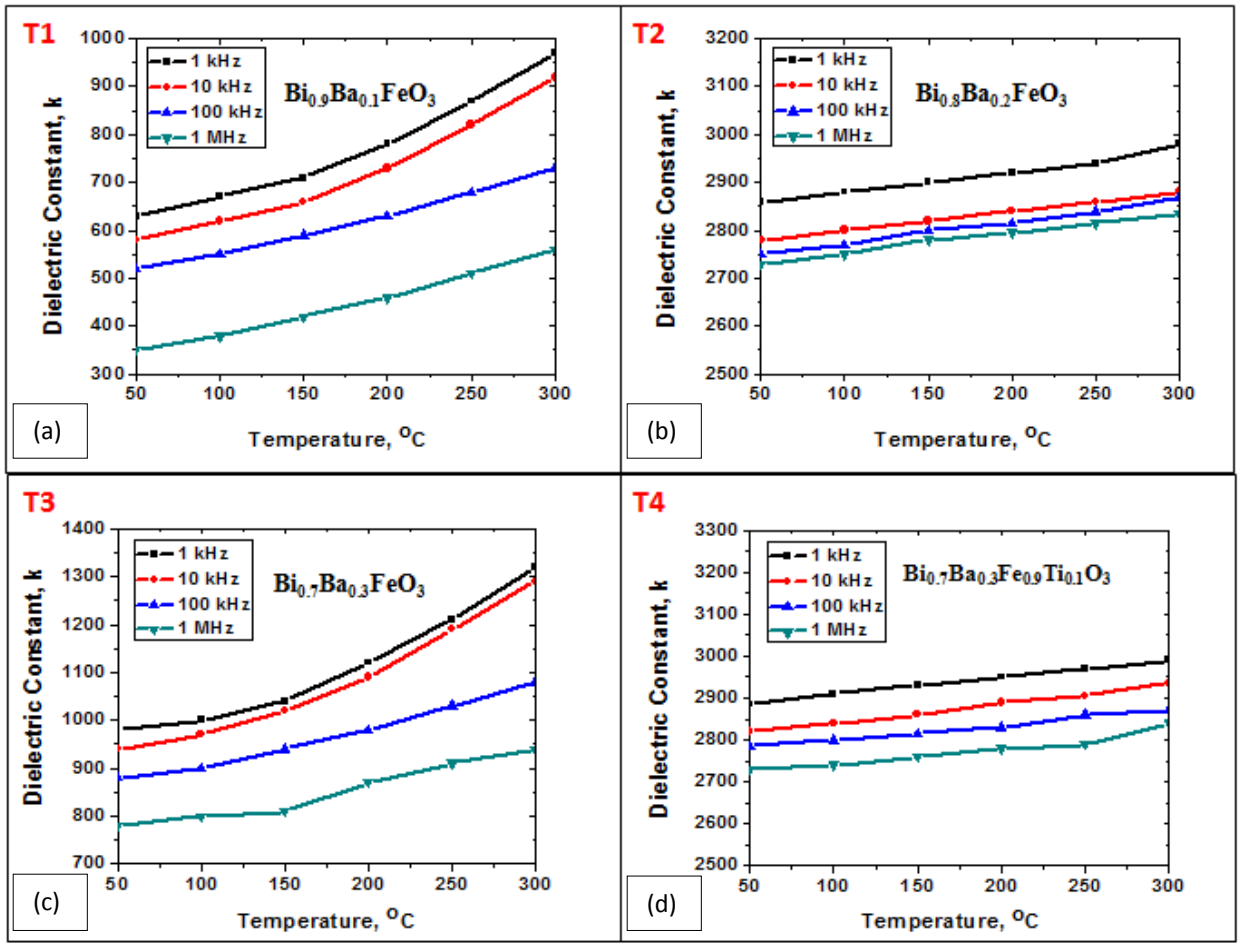

Figure 4.22: Variation of dielectric constant with temperature at different frequencies of $Bi_{1-x}Ba_xFe_{1-y}Ti_yO_3$ (x = 0.1, y = 0.0; x = 0.2, y = 0.0; x = 0.3, y = 0.0; and x = 0.3, y = 0.1) samples having optimum microstructure.

The variation of dielectric constant and loss with frequency for the same samples is shown in Figure 4.23. It is evident that the dielectric constant value decrease with increasing frequency while the loss increases with frequency for all these compositions. According to literature this variation of dielectric constant and loss with frequency is expected. At higher frequencies the polarization fails to follow the frequency of the applied field and the loss increases.

In $Bi_{0.9}Ba_{0.1}FeO_3$ and $Bi_{0.7}Ba_{0.3}FeO_3$ samples the drop in dielectric constant with frequency can also be attributed to the Maxwell–Wagner-type contribution to the dielectric constant, which is also present in the temperature dependence of dielectric constant for these samples. This phenomenon is related to the space charge relaxation at the interface. At low frequencies, the space charges formed by oxygen vacancies in these samples can follow the applied electric field and contribute to the dielectric constant. While at high frequencies, they do not have time to build up and undergo relaxation. That is why the dielectric loss for these samples increase sharply with increasing frequency from 100 Hz to 100 kHz, as can be seen from Figure 4.24. As mentioned earlier, at high frequencies space charges do not have enough time to follow the electric field, causing increase in dielectric loss. However, at frequencies above 100 kHz the change in dielectric loss with frequency for these samples become nearly constant [89].

Nevertheless, the dielectric constant and loss does not vary much for $Bi_{0.8}Ba_{0.2}FeO_3$ and $Bi_{0.7}Ba_{0.3}Fe_{0.9}Ti_{0.1}O_3$ samples due to lack of oxygen vacancies and space charges in these samples. The increase in loss with frequency for these samples is mainly due to the lagging of the motion of the domain walls with the applied alternating electric field

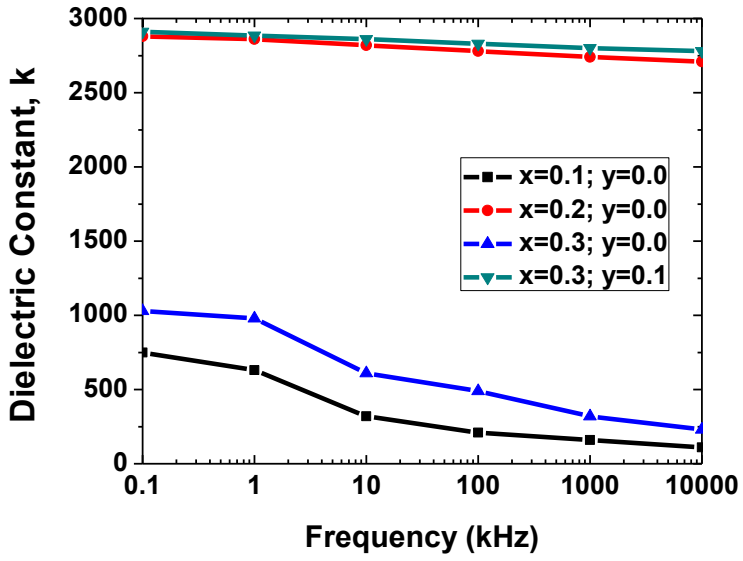

Figure 4.23: Variation of dielectric constant with frequency $Bi_{1-x}Ba_xFe_{1-y}Ti_yO_3$ (x = 0.1, y = 0.0; x = 0.2, y = 0.0; x = 0.3, y = 0.0; and x = 0.3, y = 0.1) samples having optimum microstructure.

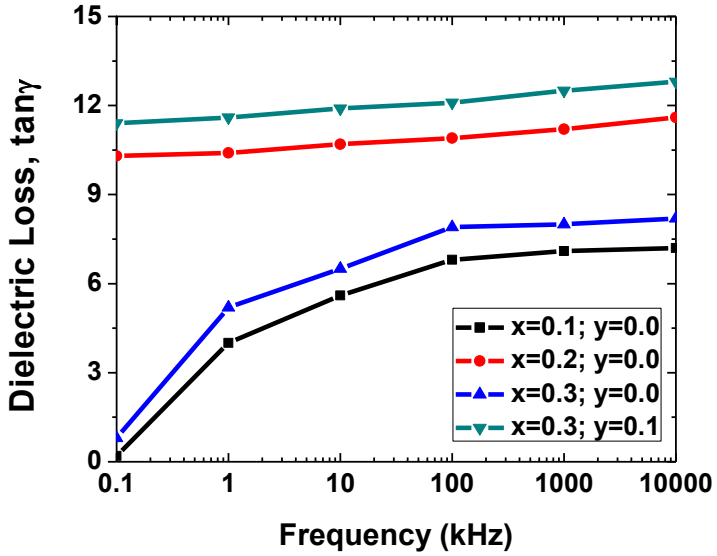

Figure 4.24: Variation of dielectric loss with frequency $Bi_{1-x}Ba_xFe_{1-y}Ti_yO_3$ (x = 0.1, y = 0.0; x = 0.2, y = 0.0; x = 0.3, y = 0.0; and x = 0.3, y = 0.1) samples having optimum microstructure.

4.6 Differential thermal analysis (DTA) for determining transition point

Compared to other multiferroics, pure BFO exhibits a higher ferroelectric Curie temperature (T_C~830°C). It has been reported that, rhombohedral–orthorhombic transition occurs at this Curie temperature. This transition is accompanied by a peak in the dielectric constant; this has been taken as an indication of a ferroelectric–paraelectric transition [153]. This is an attractive feature of dielectric property of BFO, which allows its usage in electronic devices up to very high temperature. DTA analysis of $Bi_{1-x}Ba_xFe_{1-y}Ti_yO_3$ (x = 0.1, y = 0.0; x = 0.2, y = 0.0; x = 0.3, y = 0.0; and x = 0.3, y = 0.1) samples having optimum microstructure was performed to determine their Curie Temperature and to find the effect of doping concentration on the transition temperature. The DTA result for sample T1, T2, T3 and T4 are shown in Figure 4.25.

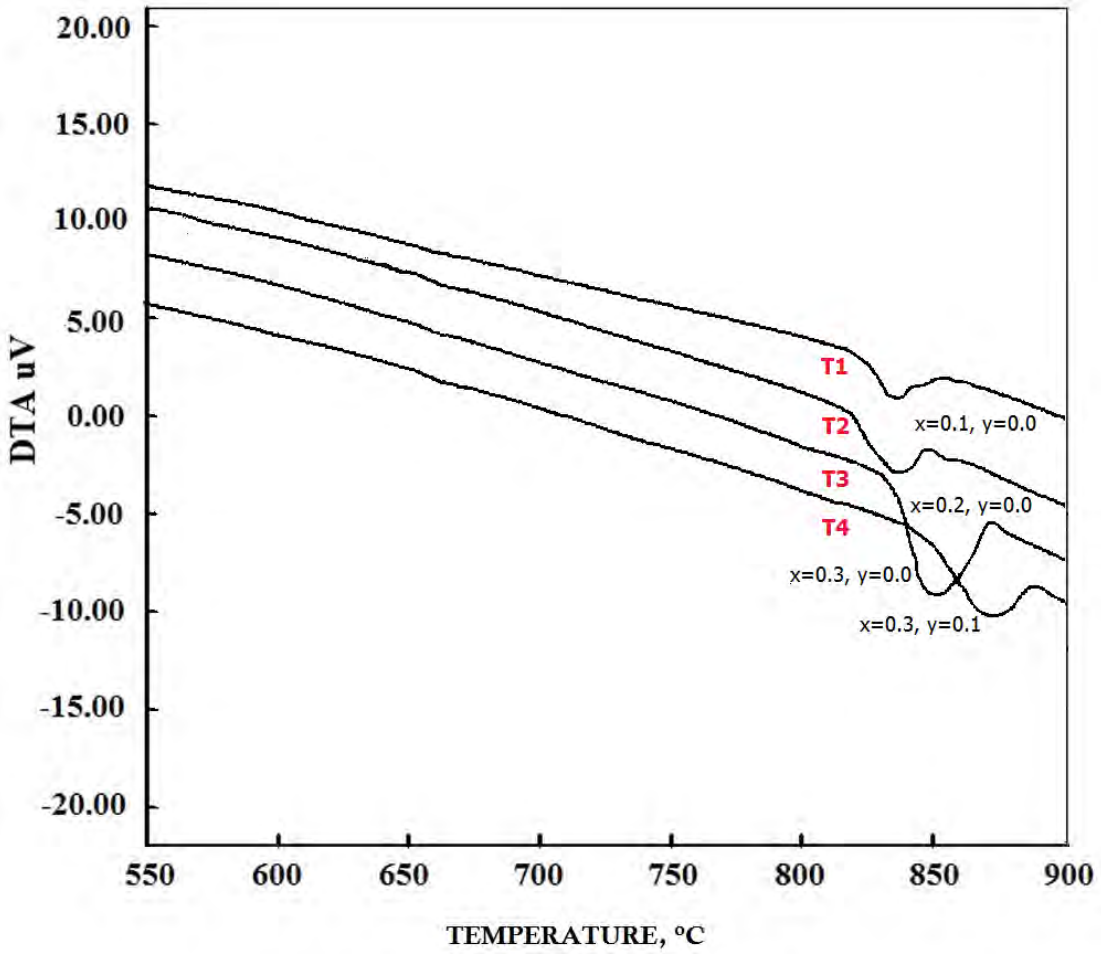

Figure 4.25: DTA analysis for $Bi_{1-x}Ba_xFe_{1-y}Ti_yO_3$ (x = 0.1, y = 0.0; x = 0.2, y = 0.0; x = 0.3, y = 0.0; and x = 0.3, y = 0.1) having optimum microstructure

For $Bi_{0.9}Ba_{0.1}FeO_3$ sample having optimum microstructure (sample T1), a peak obtained at ~835°C is attributed to the ferroelectric transition (T_C) in this compound. The peak is shifted towards higher temperature with increasing doping concentration and reaches ~866°C for $Bi_{0.7}Ba_{0.3}Fe_{0.9}Ti_{0.1}O_3$ sample having optimum microstructure (sample T4), exhibiting ferroelectric characteristics over a wide temperature range. This increase in T_C can be due to the decrease of stess with increase in the cell volume [6]. The increase in cell volume with doping concentration for $Bi_{1-x}Ba_xFe_{1-y}Ti_yO_3$ samples due to doping with larger atoms has already been reported in the XRD results (section 4.4). So, the findings of DTA analysis are in commensurate with the XRD results. Similarly, lowering of ferroelectric transition temperature is observed when doped with smaller atoms. In $BaTiO_3$ the various transition temperatures shift down on compression [90].

At Curie temperature a first-order transition to a high-temperature β phase has been reported [23]. Although there is disagreement about the exact symmetry of the β phase above Curie point, most reports agree that it is centrosymmetric, so it is probably a safe bet that the α–β transition at Curie temperature is indeed the ferroelectric–paraelectric transition. The symmetry of the β phase has been proposed to be orthorhombic by Palai et al.[64], although their data does not allow establishing the exact space group with certainty. Some authors have argued that the β phase may be tetragonal or pseudo tetragonal, but that is impossible, since the domain structure rules out a tetragonal symmetry and the perovskite a, b, c lattice constants are each quite different. It was also proposed that this phase may instead be monoclinic;[68] the measured monoclinic angle was nevertheless initially quoted as 90° within experimental error, so that the β phase was in effect __metrically orthorhombic‘‘ (i.e., the angles may be 90°, but internal ion positions in each unit cell do not satisfy orthorhombic constraints). More recently, however, R.Haumont et al. [68] have quoted a monoclinic angle of 90.018. On the other hand, the extra XRD lines used to infer monoclinic structure have not been identified. Also, the domains studied optically do not reveal the many extra wall orientations that would exist if the symmetry were monoclinic instead of orthorhombic. So, till now all the arguments are in favour of the β phase being orthorhombic.

4.7 Magnetic property measurement

The increased distortion in the original structure of BFO with increasing doping concentration reported by XRD results, distorted its cycloidal spin structure to canted spin structure and resulted in net magnetization for the doped samples. The Magnetization (M) Vs Magnetic field (H) loop of $Bi_{1-x}Ba_xFe_{1-y}Ti_yO_3$ (x = 0.1, y = 0.0; x = 0.2, y = 0.0; x = 0.3, y = 0.0; and x = 0.3, y = 0.1) samples having optimum microstructure were measured by a VSM at room temperature to find the effect of doping concentration on ferromagnetic properties of pure BFO. The M-H loop for samples T1, T2, T3 and T4 are shown in Figure 4.26.

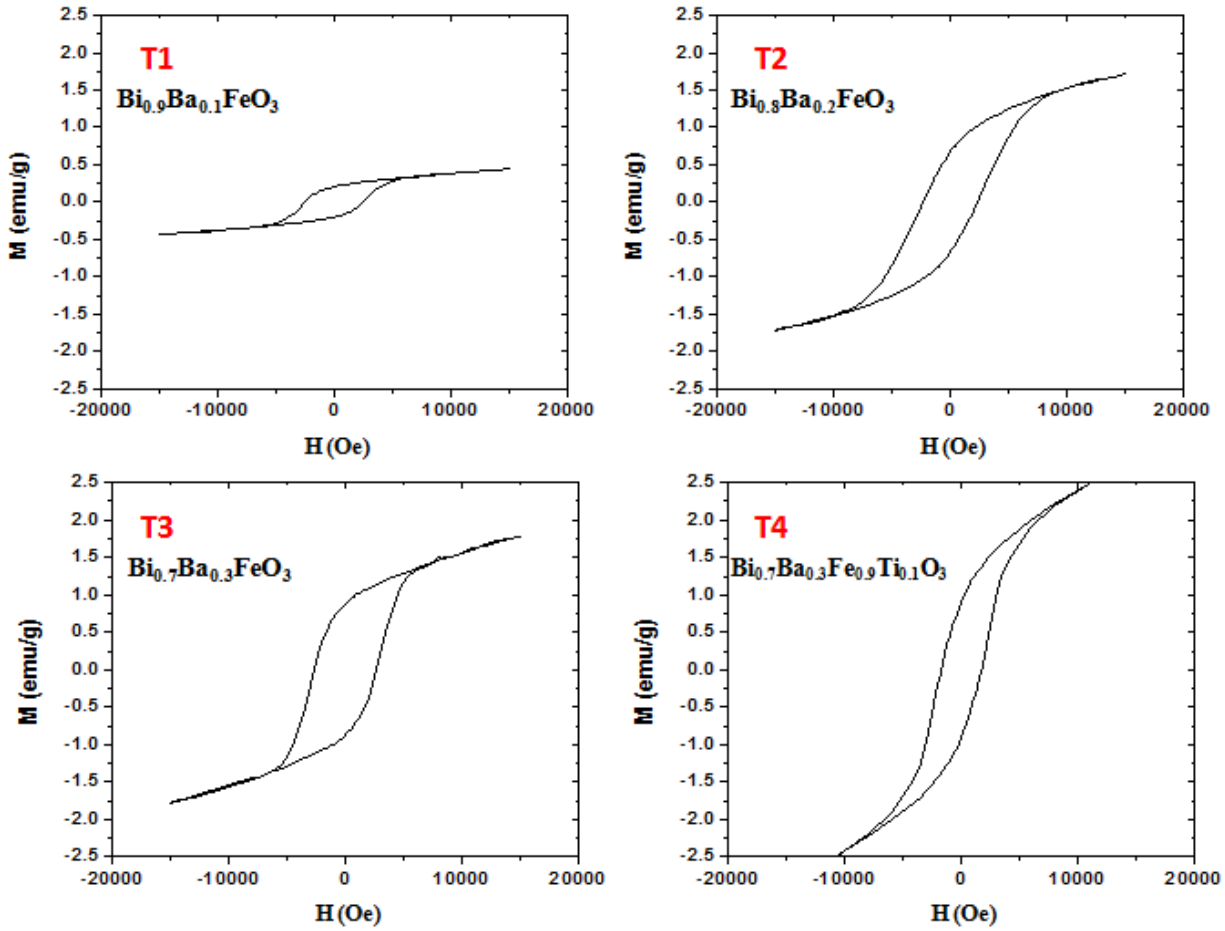

Figure 4.26: The M-H loop of $Bi_{1-x}Ba_xFe_{1-y}Ti_yO_3$ (x = 0.1, y = 0.0; x = 0.2, y = 0.0; x = 0.3, y = 0.0; and x = 0.3, y = 0.1) samples having optimum microstructure.

The hysteresis loops for T1, T2, T3 and T4 samples suggest the presence of ferromagnetic behaviour in all doped compositions. As mentioned previously, pure BFO with the rhombohedrally distorted perovskite structure allows a weak ferromagnetic ordering due to it‘s inherent cycloidal spin structure. Ba having large ionic radius compare to Bi, with Ba doping at Bi-site the structure of BFO should be distorted, then the bond angle of Fe-O-Fe may be altered changing the cycloidal spin structure of pure BFO to canted spin structure, resulting in net magnetization and ferromagnetic behaviour for Ba doped samples [12]. A comparison of these M-H loops with that of pure BFO has been shown in Figure 4.27.

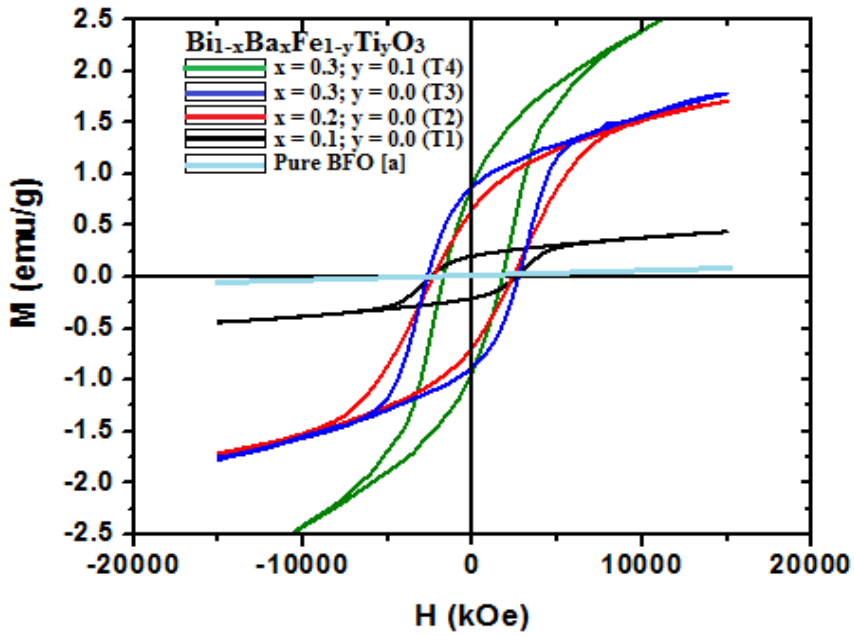

[a] Rajasree Das n, K.Mandal ,"Magnetic, ferroelectric and magnetoelectric properties of Ba-doped BiFeO3" , Journal of Magnetism and Magnetic materials, Elsevier (2012)

Figure 4.27: Comparison of the M-H loops of $Bi_{1-x}Ba_xFe_{1-y}Ti_yO_3$ (x = 0.1, y = 0.0; x = 0.2, y = 0.0; x = 0.3, y = 0.0; and x = 0.3, y = 0.1) samples with that of pure BFO.

The two important magnetic properties obtained from the M-H loops of $Bi_{1-x}Ba_xFe_{1-y}Ti_yO_3$ (x = 0.1, y = 0.0; x = 0.2, y = 0.0; x = 0.3, y = 0.0; and x = 0.3, y = 0.1) samples having optimum microstructure are remnant magnetization and coercivity. These properties have been listed in Table 4.4 for all four

Table 4.4: Remnant magnetization and coercivity of $Bi_{1-x}Ba_xFe_{1-y}Ti_yO_3$ samples having optimum microstructure.

Sample ID	Composition	Sintering Temperature (^oC)	Holding Time (hours)	(%TD)	<Grain Size> µm	Remnant Magnetization (emu/gm)	Coercivity (kOe)
T1	**$Bi_{0.9}Ba_{0.1}FeO_3$**	850	2	>95	1.0-1.1	**.23**	**2.48**
T2	**$Bi_{0.8}Ba_{0.2}FeO_3$**	875	2	>95	0.95-1.0	**.7**	**2.49**
T3	**$Bi_{0.7}Ba_{0.3}FeO_3$**	875	4	>95	0.95-1.0	**.88**	**2.5**
T4	**$Bi_{0.7}Ba_{0.3}Fe_{0.9}Ti_{0.1}O_3$**	875	6	>95	1.0-1.05	**.9**	**1.8**

Remnant magnetization indicating the magnetization left behind in a material after removing the external magnetic field is an important ferromagnetic property. As can be seen from Table 4.4, the remnant magnetization was found to increase with doping concentration from 0.23 emu/gm for $Bi_{0.9}Ba_{0.1}FeO_3$ to 0.9 emu/gm for $Bi_{0.7}Ba_{0.3}Fe_{0.9}Ti_{0.1}O_3$ sample due to increasing distortion of the structure. Although the doping concentration of Ba is similar in both samples, slight increase in remnant magnetization in $Bi_{0.7}Ba_{0.3}Fe_{0.9}Ti_{0.1}O_3$ compare to $Bi_{0.7}Ba_{0.3}FeO_3$ sample may be attributed to the breakdown of the balance between spins of Fe^{3+} due to addition of Ti^{4+} at Fe^{3+-} site [72]. However, the next important magnetic property is coercivity, which indicates the amount of magnetic field required to reduce the magnetization of a material to zero. It indicates the ease or difficulty to rotate the spins of a material by applying magnetic field or simply the ease or difficulty to magnetize or demagnetize a material. The value of coercivity was found to be almost constant for single Ba doped samples ($Bi_{1-x}Ba_xFeO_3$). The high coercivity in these samples may have resulted from the pinning effect of spins of neighbouring Fe atoms having unpaired electrons in the outer electron shell. This pinning effect hinders the movement of spins by applied magnetic field and thereby increases coercivity of the material. So, these materials are hard to demagnetize which is an important property for non-volatile memory materials. But for $Bi_{0.7}Ba_{0.3}Fe_{0.9}Ti_{0.1}O_3$ samples, although the remnant magnetization increased but it was associated with a decrease in coercivity value(~ 1.8 kOe) compare to $Bi_{1-x}Ba_xFeO_3$ samples (~ 2.5 kOe). Ti atoms have no electrons in outer d-shell, so show no spins. By replacing some Fe-sites by Ti^{4+} the pinning effect of neighbouring spins was somewhat reduced in $Bi_{0.7}Ba_{0.3}Fe_{0.9}Ti_{0.1}O_3$ samples. However, although the coercivty decreased for $Bi_{0.7}Ba_{0.3}Fe_{0.9}Ti_{0.1}O_3$, resulting in ease to magnetize or demagnetize the material, but still the coercivity value of this sample is enough for applications in memory devices.

5. CONCLUSION

The objective of this thesis project was to develop a novel multiferroic material exhibiting both ferroelectric and ferromagnetic properties by doping Ba and Ti on $BiFO_3$. This goal was successfully achieved.

Although BFO is considered a promising candidate for applications in magnetic storage devices, it's weak ferromagnetic property and leakage current due to oxygen vacancies is a major problem limiting its practical applications. It has been observed that, doping with Ba^{2+} ions at Bi-sites and Ti^{4+} at Fe-sites increased its ferromagnetic property by distorting the original structure and enhanced its dielectric property by reducing the leakage current. This research revealed the following:

- $Bi_{1-x}Ba_xFe_{1-y}Ti_yO_3$ (x = 0.1, y = 0.0; x = 0.2, y = 0.0; x = 0.3, y = 0.0; and x = 0.3, y = 0.1) ceramics were successfully prepared using solid state reaction method which was confirmed by the XRD analysis that indicated formation of single phase distorted R3c structure.
- Microstructure was developed for all compositions using trial and error method. However, the grain size was found to decrease dramatically with increasing doping concentration for $Bi_{1-x}Ba_xFe_{1-y}Ti_yO_3$ (x = 0.1, y = 0.0; x = 0.2, y = 0.0; x = 0.3, y = 0.0; and x = 0.3, y = 0.1) samples.
- Combination of good theoretical density (> 95%) and grain size (~1 μm) was obtained for all compositions when sintered using cycle-2 in the temperature range 850-875°C. Optimum multiferroic properties were obtained in this sintering zone.
- In contrast to pure BFO, $Bi_{1-x}Ba_xFe_{1-y}Ti_yO_3$ sample shows superior values of dielectric constant and remnant magnetization.
- The best value of room temperature dielectric constant (~2885) at 1 kHz frequency was attained for $Bi_{0.7}Ba_{0.3}Fe_{0.9}Ti_{0.1}O_3$ samples at grain sizes in the range of 1.0-1.05μm.
- At higher temperatures a considerable increase in the dielectric constant of $Bi_{0.9}Ba_{0.1}FeO_3$ and $Bi_{0.7}Ba_{0.3}FeO_3$ samples occurred due to space charge polarization. However, in

$Bi_{0.8}Ba_{0.2}FeO_3$ and $Bi_{0.7}Ba_{0.3}Fe_{0.9}Ti_{0.1}O_3$ the stability of dielectric constant with temperature is considerably improved due to lack of oxygen vacancy in these samples.

- DTA analysis revealed that the peak for ferroelectric transition (T_C) shifted towards higher temperatures for $Bi_{1-x}Ba_xFe_{1-y}Ti_yO_3$ samples with increasing doping concentration and reached 866°C for $Bi_{0.7}Ba_{0.3}Fe_{0.9}Ti_{0.1}O_3$.
- Remnant magnetization was also found to increase for $Bi_{1-x}Ba_xFe_{1-y}Ti_yO_3$ samples with increasing doping concentration and reached 0.9 emu/gram for $Bi_{0.7}Ba_{0.3}Fe_{0.9}Ti_{0.1}O_3$.
- The coercivity decreased in $Bi_{0.7}Ba_{0.3}Fe_{0.9}Ti_{0.1}O_3$ (~1.8 kOe) compare to single Ba doped $Bi_{1-x}Ba_xFe_{1-y}Ti_yO_3$ (x = 0.1, y = 0.0; x = 0.2, y = 0.0; x = 0.3, y = 0.0) samples due to easiness of spin flipping in this sample.

6. SUGGESTION FOR FUTURE WORK

(i) Doping B-site of $Bi_{1-x}Ba_xFeO_3$ using various dopants having higher charge than Fe^{3+} at different concentrations to find out the optimum doping concentration for improved multiferroic properties.

(ii) Fabricating multiphase multiferroic with other ABO_3 perovskite materials, such as $BaTiO_3$.

(iii) Depositing ultra-thin $BiFeO_3$ single layer or multilayer films to enhance multiferroic properties by minimizing defects of bulk material.

(iv) Synthesizing $BiFeO_3$ nano particles with grain size below 62 nm to achieve ferromagnetism by destroying spiral spin structure.

(v) Fabricating memory devices using the developed material on availability of the device fabrication lab equipments.

References

[1] N.A. Hill, ―Why Are There so Few Magnetic Ferroelectrics?", Journal of Physical Chemistry B, Vol. 104 (29) , 2000, pp 6694-6709.

[2] C.P. Bhole, ―Antiferromagnetic to Paramagnetic Phase transitions in Bismuth Ferrite (BiFeO3) Ceramics by Solid State Reaction", Ceramics – Silikáty, Vol. 56 (2), 2012, pp 127-129.

[3] W. Cheong, M. Mostovoy, ―Multiferroics: a magnetic twist for ferroelectricity, "Nature Materials, Vol. 6, 2007, pp 13-20.

[4] R. Ramesh, N.A. Spaldin, ―Multiferroics: progress and prospects in thin films", Nature Materials, Vol. 6, 2007, pp 21-29.

[5] L. Luo, W. Luo, G. Yuan, W. Wei, X. Yuan, H. Zhang, K. Shen, M. Xu, Q. Xu, ―The Origin of Enhanced Room Temperature Ferromagnetism in Ba Doped $BiFeO_3$", Journal of Superconductivity and Novel Magnetism, Vol. 26, 2013, pp 3309–3313.

[6] R. Das, K. Mandal, ―Magnetic, Ferroelectric and magnetoelectric properties of Ba-doped $BiFeO_3$", Journal of Magnetism and Magnetic Materials, Vol. 324 (11), 2012, pp 1913–1918.

[7] S.J. Kim, S.H. Han, ―Multiferroic properties of Ti-doped $BiFeO_3$ ceramics", Journal of the Korean Physical Society, Vol. 56 (1), 2012, pp 439-442.

[8] A.K. Ghosha, H. Kevin, B. Chatterjee, G.D. Dwivedi, A. Barman, H.D. Yang, S. Chatterjee, ―Effect of Sr-doping on multiferroic properties of $Bi_{0.8}La_{0.2}Fe_{0.9}Mn_{0.1}O_3$", Solid State Communications, Vol. 152, 2012, pp 557–560.

[9] A.K. Ghosh , G.D. Dwivedi, B. Chatterjee, B. Rana, A. Barmanb, S. Chatterjee, H.D. Yang, ―Role of codoping on multiferroic properties at room temperature in BiFeO3 ceramic", Solid State Communications, Vol. 166, 2013, pp 22–26.

[10] Z. Cheng, X. Wang, S. Dou, H. Kimura, K. Ozawa, ―Improved ferroelectric properties in BiFeO3 multiferroic thin film through La and Nb codoping", Physical Review B, 2008, Volume 77, 2008, pp 092101: 1-4.

[11] Y. Lin, Q. Jiang, Y. Wang, C. Nan, L. Chen, J. Yu, ―Enhancement of ferromagnetic properties in $BiFeO_3$ polycrystalline ceramic by La doping", Applied Physics Letters, Vol. 90, 2007, pp 172507: 1-3.

[12] D.H. Wang, W.C. Goh, M. Ning, C.Ong, ―Effect of Ba doping on magnetic, ferroelectric, and magnetoelectric properties in mutiferroic BiFeO3 at room temperature", Applied Physics Letters, Vol. 88, 2006, pp 212907: 1-3.

[13] Y.F. Cui, Y.G. Zhao, L.B. Luo, J.J. Yang, H. Chang, M.H. Zhu, D. Xie, T. L. Ren, ―Dielectric, magnetic, and magnetoelectric properties of La and Ti codoped $BiFeO_3$",Applied Physics Letters, Vol. 97, 2010, pp 222904: 1-3.

[14] J.F. Scott, ―Multiferroic Memories," Nature materials, Vol. 6, 2007, pp 256-257.

[15] M. Bibes and A. Barthelemy, ―Multiferroics: Towards a magnetoelectric memory," Nature materials, Vol. 7, 2008, pp 425-426.

[16] Y.K. Jun and S.H. Hong, ―Dielectric and magnetic properties in Co-and Nb-substituted $BiFeO_3$ ceramics," Solid State Communication, Vol. 144, 2007, pp. 329-333.

[17] M. Kumar and K.L. Yadav, ―Rapid liquid phase sintered Mn doped $BiFeO_3$ ceramics with enhanced polarization and weak magnetization," Applied Physics Letters, Vol. 91, 2007,pp. 242901- 242901.

[18] X. Qi, J. Dho, R. Tomov, M. G. Blamire, J. L. M. Driscoll, ―Greatly reduced leakage current and conduction mechanism in aliovalent-ion-doped $BiFeO_3$," Applied Physics Letters, Vol. 86, 2005, pp. 062903-062903.

[19] H. Zhang, W. Joo, K. Wang. K.G. Webber, ―Compositional dependence of dielectric and ferroelectric properties in $BiFeO_3$-$BaTiO_3$ solid solutions," Ceramics International, Vol. 40, 2014, pp. 4759-4765.

[20] M. Cazayous, D. Malka, D. Lebeugle, D. Colson, ―Electric field effect on BiFeO3 single crystal investigated by Raman spectroscopy," Applied Physics Letters, Vol. 91, 2007, pp. 071910-071910.

[21] Y. J. Zhang, H. G. Zhang, J. H. Yin, H. W. Zhang, J. L., Chen, W. Q. Wang and G. H. Wu, Structural and magnetic properties in $Bi_{1-x}R_xFeO_3$ (x=0–1, R=La, Nd, Sm, Eu and Tb) polycrystalline ceramics. Journal of Magnetism and Magnetic Materials, Vol. 322, 2010, pp. 2251-2255.

[22] Z. X. Cheng, X. L. Wang, H. Kimura, K. Ozawa, S. Dou, ―La and Nb codoped $BiFeO_3$ multiferroic thin films on $LaNiO_3$/Si and IrO_2/Si substrates," Applied Physics Letters, Vol. 92, 2008, pp. 092902-092902.

[23] G. Catalan and J.F. Scott, ―Physics and applications of bismuth ferrite", Advance Materials, Vol. 21, 2009, pp 2463-2485.

[24] J. Wang, J. B. Neaton, H. Zheng, V. Nagarajan, S. B. Ogale, B. Liu, D. Viehland, V. Vaithyanathan, D. G. Schlom, U. V. Waghmare, N. A. Spaldin, K. M. Rabe, M. Wuttig and R. Ramesh, ―Epitaxial BiFeO3 multiferroic thin film heterostructures," Science, Vol. 299, 2003, pp. 1719-1722.

[25] X. Qi, J. Dho, R. Tomov, M. G. Blamire and J. L. MacManus-Driscoll, ―Greatly reduced leakage current and conduction mechanism in aliovalent-ion-doped $BiFeO_3$," Applied Physics Letters, Vol. 86, 2005, pp 062903:1-3.

[26] V. A. Khomchenko, D. A. Kiselev, ―Effect of diamagnetic Ca, Sr, Pb, and Ba substitution on the crystal structure and multiferroic properties of the $BiFeO_3$ perovskite, " Journal of Applied Physics, 2008, Volume 103, pp 024105: 1-6.

[27] S. Gautam, V.S. Rangra, ―Effect of Ba ions substitution on multiferroic properties of $BiFeO_3$ perovskite," Cryst. Res. Technol., Vol. 45, 2010, pp 953 – 956.

[28] Z. Cheng, X. Wang, and S. Dou, ―Improved ferroelectric properties in multiferroic BiFeO3 thin films through La and Nb codoping," Physical Review B, Vol. 77, 2008, pp 092101: 1-4.

[29] H. Deng, M. Zheng, Z. Hu, Q. Xie, Q. Zhong, J. Wei, H. Yen, ―Enhanced dielectric and ferroelectric properties of Ba and Ti co-doped $BiFeO_3$ multiferroic ceramics," Journal of Alloys and Compounds, Vol. 582, 2014, pp 273-276.

[30] A.R. Makhdoom, M.J. Akhtar , M.A. Rafiq a, M.M. Hassan, ―Investigation of transport behavior in Ba doped BiFeO3", Ceramics International, Vol. 38, 2012, pp 3829–3834.

[31] F. Duan and J. Guojun, ―Introduction to Condensed Matter Physics," World Scientific (Vol. 1), Singapore, 2005.

[32] J. M. Yeomans, ―Statistical Mechanics of Phase Transitions," Oxford University Press, 2002.

[33] C. Kittel, ―Introduction to solid state physics," American Journal of Physics, Vol. 35, 1967, pp. 547-548.

[34] E. K. H Salje, ―Phase Transitions in Ferroelastic and Co-elastic Crystals," Cambridge University Press, 1990.

[35] V. Muller, A. Fuith, J. Fousek, H. Warhanek and H. Beige, ―Spontaneous strain in ferroelastic incommensurate [N(CH3)4]2CuCl4 crystals," Solid State Communications, Vol. 104, 1997, pp. 455-458.

[36] L. Jian and C. M. Wayman, ―Compressive behavior and domain-related shape memory effect in LaNbO4 ceramics," Materials Letters, Vol. 26, 1996, pp 1-7.

[37] R. E. Newnham, ―Molecular mechanisms in smart materials," MRS Bulletin, Vol. 22, 1997, pp. 20-34.

[38] D.I. Khomskii, ―Multiferroics: different ways to combine magnetism and ferroelectricity," Journal of Magnetism and Magnetic Materials, Vol. 306, 2006, pp 1-8.

[39] M. Fiebig, ―Revival of the magnetoelectric effect," Journal of Physics D: Applied Physics, Vol 38, 2005, pp. R123.

[40] W. Eerenstein, N. D. Mathur, and J. F. Scott, ―Multiferroic and magnetoelectric materials," Nature, Vol. 442, 2006, pp 759.

[41] J. P. Velev, S. S. Jaswal, and E. Y. Tsymbal, ―Multi-ferroic and magnetoelectric materials and interfaces," Philosophical Transactions of the Royal Society A: Mathematical, Physical and Engineering Sciences, Vol. 369, 2011, pp 3069.

[42] W. Prellier, M. Singh, P. Murugavel, ―The single-phase multiferroic oxides: from bulk to thin film," Journal of Physics: Condensed Matter, Vol. 17, 2005, pp. R803.

[43] Y. Tokura and N. Kida, ―Dynamical magnetoelectric effects in multiferroic oxides," Philosophical Transactions of the Royal Society A: Mathematical, Physical and Engineering Sciences," Vol. 369, 2011, pp. 3679-3694.

[44] G. Lawes and G. Srinivasan, ―Introduction to magnetoelectric coupling and multiferroic films," Journal of Physics D: Applied Physics, Vol. 44, 2011, pp. 243001

[45] M. Fieberg, ―Revival of the magnetoelectric effect", Journal of Physics D: Applied Physics, Vol. 38, 2005, pp. R123.

[46] W. Ehrenstein, N. Mazur, J. Scott, ―Multiferroic and magnetoelectric materials", Nature, Vol. 442, 2006, pp. 759.

[47] Special issue, Journal of Physics: Condensed Matter, Vol. 20, 2008, pp. 434201-434220.

[48] D.I.Khomskii, ―Magnetism and ferroelectricity: why do they so seldom coexist?," Bulletin of American Physical Society C, Vol. 1, 2001, pp. 21002.

[49] B. B. Van. Aken, T. T. M. Palstra, A. Filippetti, and N. A. Spaldin, ―The origin of ferroelectricity in magnetoelectric $YMnO_3$", Nature Materials, Vol. 3, 2004, pp 164-170.

[20] N. Hur, S. Park, P. A. Sharma, J. S. Ahn, S. Guha and S. W. Cheong, ―Electric polarization reversal and memory in a multiferroic material induced by magnetic fields", Nature, Vol. 429, 2004, pp 392-395.

[51] H. Kastura, N. Nagaosa and A. V. Balatsky, ―Spin current and magnetoelectric effect in noncollinear magnets," Physics Review Letters, Vol. 95, 2005, pp. 057205.

[52] T. Kimura, T. Goto, H. Shintani, K. Ishizaka, T. Arima, and Y. Tokura, ―Magnetic control of ferroelectric polarization," Nature, Vol. 426, 2003, pp. 55-58.

[53] Y. J. Choi, H. T. Yi, S. Lee, Q. Huang, V. Kiryukhin and S. W. Cheong, ―Ferroelectricity in an Ising Chain Magnet," Physics Review Letters, Vol. 100, 2008, pp. 047601.

[54] I. A. Sergienko, C. Şen, E. Dagotto, ―Ferroelectricity in the Magnetic E-Phase of Orthorhombic Perovskites," Physics Review Letters, Vol. 97, 2006, pp. 227204.

[55] T. H. O'Dell, ―The Electrodynamics of Magneto-electric Media", Publisher: North-Holland, Amsterdam, 1970.

[56] E. Ascher, H. Rieder, H. Schmid and H. Stossel, ―Some Properties of Ferromagnetoelectric Nickel-Iodine Boracite", $Ni_3B_7O_{13}I$ Journal of Applied Physics, Vol. 37, 1966, pp 1404-1405.

[57] H. Schmid, ―Multi-ferroic magnetoelectrics. Ferroelectrics", Vol. 162, 1994, pp 665.

[58] M. Fiebig, ―Revival of the magnetoelectric effect", Journal of Physics D: Applied Physics, Vol. 38, 2005, pp R123.

[59] W. Eerenstein, N.D. Mathur and J.F. Scott, ―Multiferroic and magnetoelectric materials", Nature, Vol. 442, 2006, pp 759.

[60] A. Filippetti and N.A. Hill, ―Coexistence of magnetism and ferroelectricity in perovkites," Physics Review B, Vol. 65, 2002, pp 195120.:

[61] M.F. Islam, R. Mahbub, A. Mousharraf, ―Effect of sintering parameters and Ta_2O_5 doping on the microstructure and dielectric properties of $BaTiO_3$ based ceramics", Key Engineering Materials, Vol. 608, pp 247-252, 2014.

[62] F. Kubel and H. Schmid, ―Structure of a ferroelectric and ferroelastic monodomain crystal of the perovskite $BiFeO_3$," Acta Crystallographica B, Vol. 46, 1990, pp 698.

[63] R. D. Shannon, ―Revised Effective Ionic Radii and Systematic Studies of Interatomic Distances in Halides and Chalcogenides," Acta Crystallographica A, Vol. 32, 1976, pp 751.

[64] R. Palai, R. S. Katiyar, H. Schmid, P. Tissot, S. J. Clark, J. Robertson, S. A. T. Redfern, G. Catalan and J. F. Scott, ―β phase and γ-β metal-insulator transition in multiferroic $BiFeO_3$," Physics Review B, Vol. 77, 2008, pp 014110.

[65] M. Polomska, W. Kaczmarek and Z. Pajak, "Electric and magnetic properties of $(B1-xLax)FeO_3$ solid solutions," Physica Status Solidi, Vol. 23, 1974, pp 567-574.

[66] R. Haumont, J. Kreisel, P. Bouvier and F. Hippert, ―Spin-phonon coupling in multferroics," Physics Review B, Vol. 73, 2006, 73, pp 132101.

[67] I. A. Kornev, S. Lisenkov, R. Haumont, B. Dkhil and L. Bellaiche, ―Finite- temperature properties of multiferroic $BiFeO_3$," Physics Review Letter, Vol. 99, 2007, pp 227602.

[68] R. Haumont, I. A. Kornev, S. Lisenkov, L. Bellaiche, J. Kreisel and B. Dkhil, ―Phase stability and structural temperature dependence in powdered multiferroic $BiFeO_3$," Physics Review B, Vol. 78, 2008, pp 134108.

[69] S.M. Selbach, T. Tybell, M.-A. Einarsrud and T. Grande, ―High-temperature semiconducting cubic phase of $BiFe_{0.7}Mn_{0.3}O_{3+}$,"Advanced Materials, Vol. 20, 2008, pp 3692.

[70] J.R. Teague, R. Gerson and W. J. James, Solid State Communications, Vol. 8, 1970, pp. 1073.

[71] P. Fischer, M. Polomska, I. Sosnowska, M. Szymanski, ―Temperature dependence of the crystal and magnetic structures of $BiFeO_3$", Journal of Physics C: Solid State Physics, Vol. 13, 1980, pp. 1931.

[72] M. Kumar and K.L. Yadav, ―The effect of Ti substitution on the magnetoelectric coupling at room temperature in the $BiFe_{1-x}Ti_xO_3$ system", Journal of Physics: Condensed Matter, Vol. 18, 2009, pp. 503-508.

[73] X. Qingyu, Z. Haifa, D. Wu, T. Qiu, and M.X. Xu, ―The magnetic properties of $Bi(Fe_{0.95}Co_{0.05})O_3$ ceramics", Applies Physics Letter, Vol. 95, 2009, pp. 112510.

[74] Z. Yan, K.F.Wang, J.F. Qu, Y. Wang, Z.T. Song, and S.L. Feng, ―Processing and properties of Yb-doped $BiFeO_3$ ceramics", Applied Physics Letter, Vol. 91, 2007, pp. 082906.

[75] S. Karimi, I.M. Reaney, I. Levin, I. Sterianou, ―Nd-doped $BiFeO_3$ ceramics with antipolar order", Applied Physics Letter, Vol. 94, 2009, pp. 112903.

[76] B.W. Lee, K.H Auh, ―Effect of grain sioze and mechanical processing on the dielectric properties of $BaTiO_3$", Journal of Materials reserch, Vol. 10, 1995, pp. 597-602.

[77] X.Wang, R. Chen, Z. Gui, L. Li, ―The grain size effect on the dielectric properties of $BaTiO_3$ based ceramics", Journal of Materials reserch", Materials Science and Engineering, Vol. B99, 2003, pp. 199-202.

[78] C. B. Carter, M.G. Norton, ―Ceramic Materials, Science and Engineering", Springer, 2007.

[79] Y. P. Wang, L. Zhou, M. F. Zhang, X. Y. Chen, J. M. Liu, and Z. G. Liu, ―Room-temperature saturated ferroelectric polarization in $BiFeO_3$ ceramics synthesized by rapid liquid phase sintering" Applied Physics Letters, Vol. 84, 2004, pp. 1731-1733.

[80] M. I. Morozov, N. A. Lomanova, and V. V. Gusarov, ―Specific features of $BiFeO_3$ formation in a mixture of bismuth (III) and iron (III) oxides", Russian Journal of General Chemistry, Vol. 73, 2003, pp. 1676-1680.

[81] Z. Dai, Y. Akishige, ―Electrical properties of multiferroic BiFeO3 ceramics synthesized by spark plasma sintering" Physics D: Applied Physics , Vol. 43, 2010, pp. 445403

[82] C. Chung, J. Lin, J. Wu, ―Influence of Mn and Nb dopants on electric properties of chemical-solution-deposited BiFeO3 films", Applied Physics Letter, Vol. 88, 2006, pp. 242909-242909.

[83] Y. H. Lin, Q. Jiang, Y. Wang, C. W. Nan, L. Chen and J. Yu, ―Enhancement of ferromagnetic properties in $BiFeO_3$ polycrystalline ceramic by La doping," Applied Physics Letters, Vol. 90, 2007, pp. 172507-172507.

[84] Z. Yan, K.F. Wang, J.F. Qu, Y. Wang, Z.T. Song, S.L. Feng, ―Processing andproperties of Yb-doped BiFeO3 ceramics,"Applied Physics Letter, Vol. 91, pp 082906–82908.

[85] J. Liu, M. Li, L. Pei, J. Wang, Z. Hu, X. Wang, X. Zhao, ―Effect of Ce and Zr codoping on the multiferroic properties of BiFeO3 thin films," European Physics Letter, Vol. 89, 2010, pp 57004–57010.

[86] J. Liu, M. Li, L. Pei, B. Yu, D. Guo, X. Zhao, ―Effect of Ce doping on the microstructure and electrical properties of BiFeO3 thin films prepared by chemical solution deposition," Journal of Physics D: Applied Physics, Vol. 42, 2009, pp 115409–115415.

[87] A.K. Jonscher, F. Meca and H. M. Millany, ―Charge-carrier contributions to dielectric loss", Journal of Physics C: Solid State Physics, Vol. 12, 1979, pp. L293.

[88] H. Singh and K. L. Yadav ―Dielectric, magnetic and magnetoelectric properties of La and Nb codoped bismuth ferrite," Journal of Physics: Condensed Matter, Vol. 23, 2011, pp. 385901:1-6.

[89] Reetu, A. Agarwal1, S. Sanghi, Ashima and N. Ahlawat, ―Structural transformation and improved dielectric and magnetic properties in Ti-substituted $Bi_{0.8}La_{0.2}FeO_3$ multiferroics," Journal of Physics D: Applied Physics, Vol. 45, 2012, pp 165001:1-9.

[90] T. Ishidate, S. Abe, ―Elastic anomaly and phase transition of $BaTiO_3$", Physical Review Letters, Vol.78, 1997, pp. 12.